University of London
Imperial College of Science, Technology and Medicine
Department of Physics

Quantum Simulation of Confinement Dynamics

Joseph William Vovrosh

Submitted in part fulfilment of the requirements for the degree of
Doctor of Philosophy in Physics of the University of London and
the Diploma of Imperial College, September 2022

Abstract

Quantum computers have generated much excitement over recent years due to their potential to outperform classical computers in many difficult problems. While a fully fault tolerant quantum device is yet to be built, there has been much work pushing for noisy intermediate-scale quantum (NISQ) devices to achieve quantum advantage. One of the most promising fields to accomplish this is in quantum simulation of quantum many-body systems. A classical computer is able to simulate a general quantum system but suffers from exponential memory requirements in system size. Thus, for exact results, classical computers are limited to simulating just tens of particles whereas realistic quantum systems are comprised of $\sim 10^{23}$. Quantum computers are able to reduce this memory cost to polynomial growth making them key to understand the physics of many-body systems. One area that is notably difficult to simulate is confinement physics. Confinement is the phenomenon in which the energy of two particles grows indefinitely with their separation - most prominently found between quarks in quantum chromodynamics (QCD). In this work we will consider the application of quantum devices to simulate such phenomena. In particular, we consider simple condensed matter systems, namely variations of the Ising model, that exhibit confinement physics. In the first half of this work we perform an analytical and numerical study of confinement, and develop a trotterization protocol to enable the quantum simulation of such physics on a digital quantum computer. We present results obtained directly on an IBM quantum computer showing the non-equilibrium effects of confinement in such systems. In order to achieve these results we developed state-of-the-art error mitigation methods to combat the large errors inherently faced in current NISQ devices. In the latter half, we propose physical phenomena that may act as a benchmark for quantum devices in the future. Collisions of mesons (boundstates of two particles) with impurities are considered in which a long-lived metastable state is found to form. Such collisions have potential to be simulated on digital quantum computers in the near future. We then consider collisions of mesons in systems with long-range interactions. We show how collisions of interacting mesons can lead to the formation of hadrons (boundstates of many constituent particles) in a fusion type event. While these proposals are beyond current digital quantum computer capabilities, analogue quantum simulation devices such as trapped ion setups or Rydberg atom experiments are well suited to realise this physics.

Acknowledgments

My utmost thanks go to my supervisor Prof. Johannes Knolle. Throughout the entire PhD, Johannes not only helped me to explore the field of physics freely but also supplied me with more fascinating questions than I had time to answer. Beyond this, Johannes has always showed patience and given guidance through my personal struggles during the PhD; for this I am most grateful.

I would like to give special thanks to Kiran E. Khosla, whom acted as a mentor throughout the entirety of my PhD. Kiran always had time to explore new ideas with me, both as a collaborator and as a teacher.

I am very appreciative for both Hongzheng Zhao and Sean Greenaway for their openness to discussions, whether it led to a full collaboration or just an enjoyable morning conversation. This created the perfect environment to perform research.

Finally, I benefited greatly from collaborations with Alvise Bastianello, Christopher Self, Myungshik Kim and Rick Mukherjee, each of whom I worked closely with throughout my projects. From their influence I learnt the process of research, from the initial idea all the way through to publication.

To Holly Richards,

Declaration of Authorship

I, Joseph Vovrosh, declare that this thesis titled, "Quantum Simulation of Confinement Dynamics" and the work presented in it are my own. I confirm that:

- This work was done wholly or mainly while in candidature for a research degree at this University.
- Where I have quoted from the work of others, the source is always given. With the exception of such quotations, this thesis is entirely my own work.
- I have acknowledged all main sources of help.
- Where the thesis is based on work done by myself jointly with others, I have made clear exactly what was done by others and what I have contributed myself.

The core part of the thesis is based on the research appearing in:

[1] J. Vovrosh and J. Knolle, "Confinement and entanglement dynamics on a digital quantum computer," *Scientific Reports*, vol. 11, p. 11577, Jun 2021

[2] J. Vovrosh, H. Zhao, J. Knolle, and A. Bastianello, "Confinement-induced impurity states in spin chains," *Phys. Rev. B*, vol. 105, p. L100301, Mar 2022

[3] J. Vovrosh, K. E. Khosla, S. Greenaway, C. Self, M. S. Kim, and J. Knolle, "Simple mitigation of global depolarizing errors in quantum simulations," *Phys. Rev. E*, vol. 104, p. 035309, Sep 2021

[4] J. Vovrosh, R. Mukherjee, A. Bastianello, and J. Knolle, "Dynamical hadron formation in long-range interacting quantum spin chains," *arXiv preprint 2204.05641*, Apr 2022

Other works published during my doctoral research not included in this thesis:

[5] H. Zhao, J. Vovrosh, F. Mintert, and J. Knolle, "Quantum many-body scars in optical lattices," *Phys. Rev. Lett.*, vol. 124, p. 160604, Apr 2020

Contents

Abstract i

Acknowledgements iii

1 Motivation 1

1.1 Outline . . . 3

2 Quantum Simulation 4

2.1 Qubits and Quantum Gates . . . 6

2.1.1 Quantum Circuits . . . 9

2.2 Variational Quantum Eigensolvers . . . 10

2.3 Quantum Simulation of Non-Equilibrium Dynamics . . . 11

2.3.1 Suzuki-Trotter decomposition . . . 12

2.3.2 Gate Decomposition . . . 13

2.4 Randomised Measurement Methods . . . 14

2.5 Experimental Realisation of Quantum Computers . . . 16

2.5.1 Generating a Bell State on an IBM Device . . . 18

2.6 Errors in NISQ devices . . . 18

2.6.1 Choosing the Layout of Qubits . . . 22

2.6.2 Measurement Error Mitigation . . . 23

3 Confinement Dynamics **25**

3.1 Two Particle Model . . . 26

3.2 Confinement in Spin Chains . . . 27

3.2.1 The Transverse Field Ising model . . . 28

3.2.2 The Transverse Ising Model with a Longitudinal Field . . . 29

3.2.3 The long-range Ising Model . . . 32

3.3 Signatures of Confinement . . . 33

3.3.1 Meson Masses . . . 34

3.3.2 Meson Velocities . . . 35

3.3.3 Entanglement Spread . . . 36

4 Digital Quantum Simulation of Confinement Dynamics **38**

4.1 Quantum Circuit and Initialisation . . . 39

4.2 Error Mitigation . . . 40

4.3 Results . . . 42

4.3.1 Meson Velocities . . . 42

4.3.2 Suppression of Entropy Spread . . . 44

4.3.3 Probability Maps . . . 46

5 Simple Mitigation of Global Depolarising Errors in Quantum Simulations 50

5.1 A Global Depolarising Error Model 51

5.2 Mitigation Protocol 53

5.2.1 Simplified Method 55

5.3 Simulated Results 55

5.3.1 Calibration 57

5.4 Results form the IBM Devices 58

5.4.1 Meson Masses 58

5.4.2 Suppression of Entanglement Spread 60

6 Confinement Induced Impurity States in Spin Chains 62

6.1 The Model 64

6.2 Confinement and Metastable Trapping 65

6.2.1 Semi Classical Approximation 65

6.2.2 Two Domain-Wall Subspace 67

6.3 Time-Evolving Block Decimation Results 70

7 Dynamical Hadron Formation in Long-Range Interacting Quantum Spin Chains 72

7.1 Hadrons in the Long-Range Ising Model 73

7.2 The 1-Meson Subspace 75

7.3 Inelastic Collisions of Large Mesons 79

7.4 Inducing Fusion Events 80

7.4.1 An Abrupt Change to the Transverse Field . . . 81
7.4.2 Modifying the Long-Range Interactions . . . 82
7.4.3 Inducing Fusion Events for Larger Mesons . . . 87
7.5 Experimental Feasibility . . . 88

8 Conclusion **92**
8.1 Summary of Thesis Achievements . . . 92
8.2 Future Work . . . 93
8.2.1 Dynamical Hadron Formation in the Lattice Schwinger Model . . . 94
8.2.2 Scalable Error Mitigation . . . 94

Bibliography **95**

A **118**
A.1 The Jordan-Wigner Transformation . . . 118
A.2 Semiclassical Two Fermion Subspace Hamiltonian . . . 120
A.3 Eigensystem of the Two domain-wall Subspace . . . 121

B **123**
B.1 Effectiveness of Error Mitigation Methods . . . 123

C **125**
C.1 Impurities in the Two Domain-Wall Subspace . . . 125
C.2 The Semiclassical Limit . . . 131
C.3 The Tensor Network Simulations . . . 138

D **145**

D.1 Meson Wavepackets 145

D.2 Truncation of Meson Width 146

Chapter 1

Motivation

Physics attempts to accurately describe the world around us. However, the problem of describing any part of nature at the fundamental quantum level is that its building blocks are so small. Anything that exists at the human scale is made up of an unimaginable number of elementary particles. Thus, even when considering the behaviour of some seemingly simple materials, the sheer number of degrees of freedom faced make the mathematical task of fully describing it by hand insurmountable. Luckily, for systems close to equilibrium, physicists can take advantage of the high level of universality in nature. This allows a statistical approach to accurately describe many phenomena. However, when trying to understand emergent behaviours of strongly correlated quantum many-body systems such as high temperature superconductivity, the underpinnings of molecular properties in quantum chemistry, or the very nature of interactions between particles in QCD, this approach fails. It is in these areas in which a computer becomes a useful tool to solve the large mathematical systems that are inherently faced in physics research.

One area of physics that computers are vital for is the study of quantum many-body systems. However, despite modern high performance computers having access to many thousands of CPUs/GPUs and terabytes of available data for storage, when considering a simple one-dimensional system of fermions, only tens of particles can be considered - a far cry from the Avogadro's constant number of particles in a true physical system. This is due to the exponential growth of memory cost and computation time with respect to system size. Typically, physicists resort to approximations in their calculations, two examples of which are Monte Carlo methods [6], which suffer from the "minus-sign

problem" [7], and the Density Matrix Renormalization Group method [8], which does not cope well with multidimensional systems and highly entangled states.

The work outlined in this thesis is motivated by the promise of quantum computers to solve the issue of exploding memory costs when simulating quantum systems. Due to the one-to-one mapping between qubits (the fundamental building blocks of a quantum computer) and fermions, the memory cost of simulating the same one-dimensional system of fermions becomes linear. Thus, given a quantum device that has as many qubits as a traditional classical computer has bits, we would be able to simulate exponentially larger systems. This could lead to a better understanding of molecular properties in quantum chemistry, improve our ability to simulate Hamiltonian evolution as well as accurately describing the fundamental interactions between elementary particles.

In this work we consider the ability of current quantum computers - both digital and analogue - to simulate confinement dynamics between particles. Confinement is typically found in the context of interactions between quarks due to the strong nuclear force. Understanding confinement physics is notoriously difficult, exemplified by the Clay Mathematics Institute offering a prize of $\$1{,}000{,}000$ to the person who is able to complete the mathematical description of this phenomenon [9]. Confinement has recently seen an influx of interest from the condensed matter physics community due to it appearing in many simple one-dimensional spin chain systems that are already well studied [10, 11, 12, 13]. As previously mentioned, not only are these spin systems much simpler to analyse they also map easily onto a quantum computer – making them a prime target for near term quantum simulation efforts. It was the aim of this work to do just this, as well as propose the first steps in pushing closer to a full simulation of the SU(3) gauge theory of QCD on a quantum computer.

1.1 Outline

This thesis is structured as follows. In Chapter 2, the main concepts that will be considered throughout this thesis are introduced. Firstly, the building blocks of a quantum computer, the *qubit* and *quantum gates* are presented. After this, some of the different methods of how a quantum computer is used to probe physical systems are described, from obtaining the ground state energy to simulating time evolution dynamics. In particular, a recent protocol utilising repeated randomised measurements for calculating Rényi entropies is outlined; this protocol is heavily used throughout this body of work. Finally, the errors inherent in current NISQ devices and current methods to deal with these are discussed. In Chapter 3, confinement physics in the setting of quantum spin chains is introduced and explanations are given as to why it is an ideal testing ground for current quantum computers. Two mechanisms to induce confinement in the Ising model are the focus. Finally, signatures of confinement present in the non-equilibrium dynamics of these systems that can act as a smoking gun of confinement are outlined.

Chapter 4 will present results from a real IBM quantum device that directly observe confinement physics, including the first ever measurements of the second order Rényi entropy on a digital quantum computer. In Chapter 5, an error mitigation protocol is presented that is not only effective, allowing us to observe signatures of confinement that were previously out of reach on from a NISQ device, but also is generally applicable and simple to implement. In Chapter 6 and 7, collisions with mesons are considered, in which exotic many-particle states are excited with long lifetimes. Such collisions are considered with experimental feasibility in mind, with the aim of outlining a future direction for NISQ quantum simulation efforts.

Chapter 2

Quantum Simulation

In order to appreciate the complexity of simulating quantum many-body systems consider a one-dimensional quantum spin chain of length N. Each spin can be in a superposition of both up and down spin states with some probability p_i of being measured in an up state and $1 - p_i$ of being measured in a down state, here i labels the spin in consideration. Thus, one might naively think that only N parameters are required to fully describe the quantum spin chain. However, this is only true for product states, for a general quantum state entanglement breaks this intuition. The Hilbert space of such a spin chain is spanned by the 2^N basis states $|j\rangle$, with $0 < j \leq 2^N$. Thus, the general quantum state $|\psi\rangle$ of this spin chain is written out as the linear combination of all these 2^N basis states,

$$|\psi\rangle = \sum_{j=1}^{2^N} \alpha_j |j\rangle , \tag{2.1}$$

where α_j are complex numbers with $\sum_j |\alpha_j|^2 = 1$. When storing such a quantum state on a classical device, each individual complex coefficient is comprised of two floating point numbers, one for the real part and one for the imaginary part. If 4 bytes are used to store each of these floating-point numbers individually, then the memory required to store the general quantum state of a spin chain grows as 8^N bytes. In order to store the Hamiltonian of such a system, a matrix of size $2^N \times 2^N$ is required - costing a further 2^{2N+3} bytes. These memory requirements quickly supersede the current available memories of classical devices. The time evolution of one of the largest spin chains ever calculated was $N = 36$, requiring a Terabyte of memory and multiple CPUs [14].

The first notions of using quantum mechanics to better technological power was in the, now famous, lecture given by Feynman in Caltech titled '*There's Plenty of Room at the Bottom: An Invitation to Enter a New Field of Physics*' on 29^{th} December 1959. Here, he proposed that in the future physicists would develop nanoscale machines that "*arrange the atoms the way we want*". Feynman further reiterated this in his famous talk '*Simulating physics with computers*' at MIT in 1981 [15];

> "*Nature isn't classical, dammit, and if you want to make a simulation of nature, you'd better make it quantum mechanical, and by golly it's a wonderful problem, because it doesn't look so easy.*"

The first successes in quantum simulation came through analogue methods. The idea behind analogue quantum simulation is to map a complicated quantum system, H_{sys}, one that we cannot directly describe, to a quantum system that we have good control over, H_{sim}. In this way, we can make use of our abilities to experimentally control a system described by H_{sim} to reproduce the details of the desired physics of H_{sys}. The most advanced, and perhaps most successful experimental setup that has allowed for the simulation of many phenomena is ultracold atoms trapped in an optical lattice [16]. These optical lattice setups have promise to probe different many-body physics problems out of reach for classical supercomputer [17]. Namely, these systems have been used to probe properties of the doped Fermi-Hubbard model, the ground state of which is expected to give insight into the nature of high-temperature super conductors [18]. Furthermore, they have been used to simulate the non-equilibrium time dynamics of two dimensional many-body systems [19, 20]. Optical lattices have even been used to realise quantum spin chains [21].

While analogue quantum simulation has promise to supersede the power of classical supercomputers, their capabilities are limited by the inherent physics that governs them; if a mapping from $H_{sys} \leftrightarrow H_{sim}$ does not exist, analogue quantum simulation fails. A more ambitious goal is currently at the height of popularity in academia, as well as industrial physics research - the development of a *universal quantum computer*, a device that can simulate any quantum phenomena to arbitrary accuracy. In the following we introduce the basic building blocks of quantum computing, namely, *qubits* and *quantum gates*.

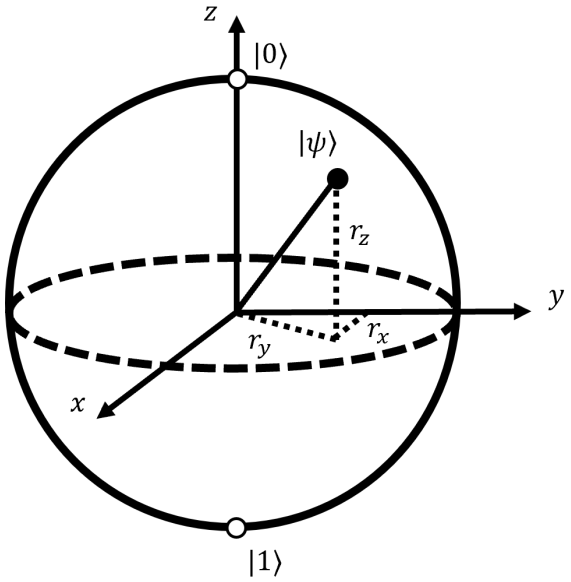

Figure 2.1: A graphical depiction of the Bloch sphere for a qubit described by the density matrix $\rho = \frac{1}{2}(\mathcal{I} + r_x\sigma_x + r_y\sigma_y + r_z\sigma_z)$

2.1 Qubits and Quantum Gates

The building blocks of classical computers are bits, each of which is a binary digit that can either be in the state '0' or '1'. These are realised in modern computers though electromechanical transistors which can map electrical signals into one of two states. By encoding information into binary, we are able to store information on a set of bits. The quantum equivalent of bits are quantum bits or *qubits*. Qubits are quantum objects that can be described by a two-level quantum mechanical Hilbert space in which the general state is given by

$$|\psi\rangle = \alpha_0 |0\rangle + \alpha_1 |1\rangle . \tag{2.2}$$

This qubit has a probability $|\alpha_0|^2$ of being measured as 0 and a probability $|\alpha_1|^2$ of being measured as 1. Note, α_0 and α_1 must follow the condition that $|\alpha_0|^2 + |\alpha_1|^2 = 1$, or that the sum of the probabilities is unity. Thus qubits can also exist in the states '0' and '1' but also any superposition of the two.

A common description of the qubit state is the density matrix formulation. Consider a general quantum state that has probabilities p_i of being measured in the states ψ_i. The density matrix of this state

NOT	
Input	Output
0	1
1	0

NAND	
Input	Output
(0,0)	1
(0,1)	1
(1,0)	1
(1,1)	0

NOR	
Input	Output
(0,0)	1
(0,1)	0
(1,0)	0
(1,1)	0

Table 2.1: Truth tables for the NOT, NAND and NOR classical logic gate.

is given by

$$\rho = \sum_i p_i \left|\psi_i\right\rangle \left\langle\psi_i\right| . \tag{2.3}$$

The density matrix formulation of a quantum system allows us to fully describe the state. If $p_i = 0$ for all $i \neq j$ and $p_j = 1$, the quantum system is said to be in a *pure* state and the purity of the state, $\mathrm{Tr}(\rho^2) = 1$. If more than one of the probabilities are non-zero the quantum state is in a *mixed* state. In this case, the purity satisfies $\frac{1}{d} \leq \mathrm{tr}(\rho^2) \leq 1$ in which d is the dimension of the Hilbert space. Furthermore, given any observable $\hat{O}$, in the form of a Hermitian matrix, its expectation value is given by $\mathrm{Tr}\left[\hat{O}\rho\right]$. The density matrix of a general qubit is

$$\rho = \frac{1}{2}(\mathcal{I} + r_x\sigma_x + r_y\sigma_y + r_z\sigma_z), \tag{2.4}$$

where $\mathcal{I}$ is the 2×2 identity matrix, σ_x, σ_y and σ_z are the Pauli matrices and (r_x, r_y, r_z) is a vector with $||\mathbf{r}|| = 1$. Given this representation, the state of a qubit can be visualised pictorially on the Bloch sphere, see Fig. 2.1.

In order to do classical computation with bits, computers implement gates. These are functions that take binary inputs and output a binary sequence. For example, the NOT gate given the input '0' outputs '1', and given the input '1' outputs '0'. The truth table is shown in Table. 2.1. Similarly, quantum computers are able to do calculations with qubits via *quantum gates*. A quantum gate is a unitary operator that, given a quantum state as an input, outputs a quantum state, i.e. $\mathcal{U}$ such that

$$\left|\psi_{out}\right\rangle = \mathcal{U}\left|\psi_{in}\right\rangle . \tag{2.5}$$

Note that for any quantum gate $\mathcal{U}$ there does not exist two quantum states, $|\psi_1\rangle$ and $|\psi_2\rangle$ such that $\mathcal{U}|\psi_1\rangle = \mathcal{U}|\psi_2\rangle$, i.e. quantum computation is reversible [22]. In order for a classical computer

to be *universal* it must be able to implement the functions of all logic gates to arbitrary accuracy. Henry M. Sheffer proved that this can be achieved via just two gates, the NAND and NOR gates; see Table. 2.1 for their truth tables [23]. Similarly, for a quantum computer to be universal it must be able to implement the functions of all quantum gates to arbitrary accuracy. A commonly used set of quantum gates that achieve this are the single qubit rotation gates, $\mathcal{R}_x(\theta)$, $\mathcal{R}_y(\theta)$ and $\mathcal{R}_z(\theta)$, the single qubit phase shift gate, $P(\phi)$, and the two-qubit controlled-NOT (CNOT) gate. Given the vector representation of a single qubit state

$$|\psi\rangle = \alpha_0 |0\rangle + \alpha_1 |1\rangle \rightarrow \begin{pmatrix} \alpha_0 \\ \alpha_1 \end{pmatrix}, \tag{2.6}$$

and the vector representation of the two-qubit state

$$|\psi\rangle = \alpha_{00} |00\rangle + \alpha_{01} |01\rangle + \alpha_{10} |10\rangle + \alpha_{11} |11\rangle \rightarrow \begin{pmatrix} \alpha_{00} \\ \alpha_{01} \\ \alpha_{10} \\ \alpha_{11} \end{pmatrix}, \tag{2.7}$$

the definitions of these gates are below:

$$\mathcal{R}_x(\theta) = \begin{pmatrix} \cos\frac{\theta}{2} & -i\sin\frac{\theta}{2} \\ -i\sin\frac{\theta}{2} & \cos\frac{\theta}{2} \end{pmatrix}, \quad \mathcal{R}_y(\theta) = \begin{pmatrix} \cos\frac{\theta}{2} & -\sin\frac{\theta}{2} \\ \sin\frac{\theta}{2} & \cos\frac{\theta}{2} \end{pmatrix}, \quad \mathcal{R}_z(\theta) = \begin{pmatrix} e^{-i\frac{\theta}{2}} & 0 \\ 0 & e^{i\frac{\theta}{2}} \end{pmatrix}, \tag{2.8}$$

$$CNOT = \begin{pmatrix} 1 & 0 & 0 & 0 \\ 0 & 1 & 0 & 0 \\ 0 & 0 & 0 & 1 \\ 0 & 0 & 1 & 0 \end{pmatrix}, \qquad P(\phi) = \begin{pmatrix} 1 & 0 \\ 0 & e^{i\theta} \end{pmatrix}. \tag{2.9}$$

The Solovay–Kitaev theorem proves that with a set of universal quantum gates, we are able to efficiently approximate a general quantum gate [24]. While it is possible to decompose deep quantum circuits using these matrices by hand, the task quickly becomes overwhelming. A concise notation for quantum circuits is commonly used in the relevant literature that will be briefly introduced here.

2.1.1 Quantum Circuits

Consider a N qubit circuit. Pictorially we represent this as N lines stacked vertically with the horizontal axis representing time:

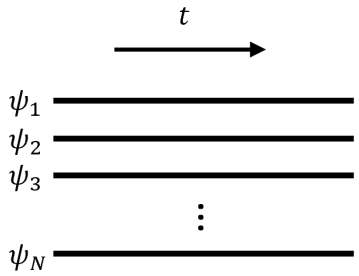

Figure 2.2: A blank quantum circuit of N qubits.

A unitary operation acting on a subset of these qubits is represented as a rectangle that overlaps the qubit registers that it effects. Note that the horizontal length of this rectangle typically is a rough intuition of the relative gate depth required to realise this unitary:

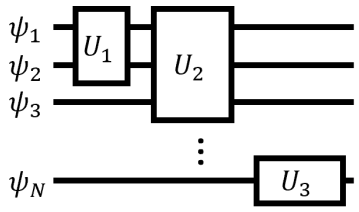

Figure 2.3: A generic quantum circuit of N qubits.

At the gate level, each commonly used gate has a pictorial representation used in quantum circuit notation. Below we give the notation for the rotation gates, $\mathcal{R}_\alpha(\theta)$, phase shift gate, $P(\phi)$, CNOT gate and a measurement. Note that the below representation of the CNOT gate acts on the lower qubit with respect to the upper qubits state.

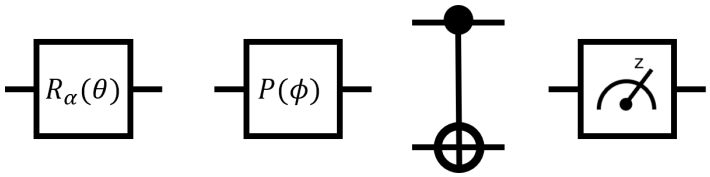

Figure 2.4: The pictorial representations of the rotation gates, phase shift gate, a CNOT gate and a qubit measurement.

Given the framework of qubits and quantum gates, there are many theoretically possible calculations that a quantum computer would be able to perform far quicker than a classical super computer [25]. The most well known is the exponential speed up of the quantum Fourier transformation utilised in the quantum phase estimation algorithm, an algorithm that determines the eigenvalue of an eigenvector [26, 27, 28]. This algorithm is a subroutine in the notorious Shor's algorithm which solves both the discrete logarithm problem and integer factorization in polynomial time [29]. This algorithm is proposed to break the widely used RSA algorithm for encryption that relies on the NP-hard problem of decomposing a large integer into its constitute prime factors [30]. However, in this work it is the promise of quantum computers to simulate physical systems that will take main stage. In the following, three popular directions for quantum simulation, namely variational quantum eigensolvers, Hamiltonian evolution and randomised measurement methods are introduced.

2.2 Variational Quantum Eigensolvers

A popular area of active research in quantum simulation using digital quantum computers is variational quantum eigensolvers (VQE). VQE methods are examples of quantum/classical algorithms that aim to utilise quantum state preparation and measurement in combination with classical optimisation. The aim of these algorithms are to find the ground state of a given Hamiltonian [31, 32, 33]. While it is tangential to the work presented in this thesis, for completeness it is briefly introduced here.

The setup for VQE requires a general unitary operator, U, that has many tunable parameters, θ, which can be used to initialise a vast number of quantum states on the quantum computer, $|\psi(\theta)\rangle = U(\theta)\,|\mathbf{0}\rangle$. The exact form of this ansatz will vary depending on what is efficient given the hardware in use. To begin, we initialise this ansatz with random inputs and measure the energy with respect to the Hamiltonian in consideration; this will define the cost function of the protocol. Furthermore, the gradients of the energy with respect to the tunable parameters are also measured on the quantum device; this can be done via the parameter shift rule for example [34]. From this we can use classical optimisation methods to tune the parameters of the ansatz to minimise the cost. Given many optimisation steps and that the ansatz is general enough, an upper bound on the ground state of the Hamiltonian can be found.

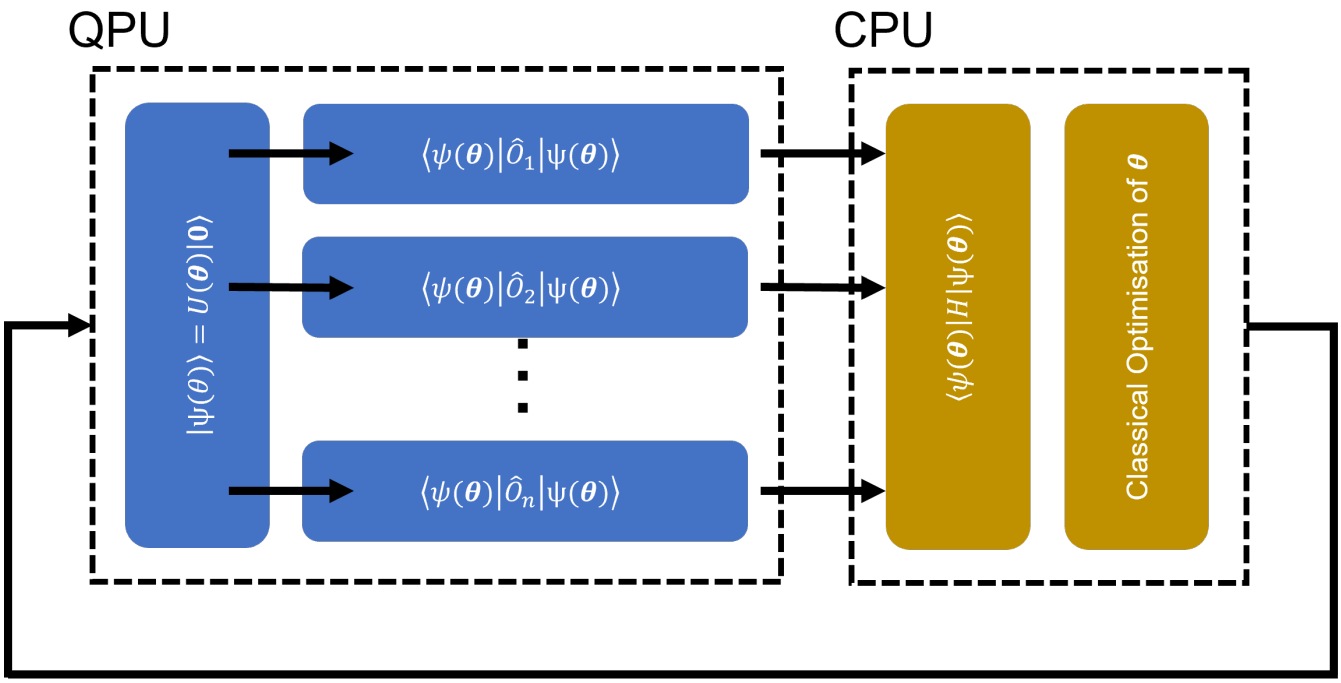

Figure 2.5: A schematic of the VQE algorithm. We first initialise the ansatz with the parameters $\boldsymbol{\theta}$ on the quantum computer via acting the unitary $\boldsymbol{U}(\boldsymbol{\theta})$ on the fiducal state $|0\rangle$. Then we measure the local observables $\hat{\boldsymbol{O}}_i$ which allow us to classically obtain the energy of the quantum state. Finally, we use classical optimisation to update $\boldsymbol{\theta}$ to minimise the energy.

To perform this process on a classical computer would require an exponential number of bits with respect to system size to fully parameterise a general quantum state. On a quantum computer only a linear number of qubits are required. However, there are powerful classical algorithms that can perform this task efficiently given the quantum state in consideration is low-dimensional, such as the density matrix renormalisation group approximation [8]. Thus, while there is scope to achieve quantum advantage using a VQE algorithm, perhaps a more exciting prospect is that of the simulation of the non-equilibrium dynamics of a quantum many-body system.

2.3 Quantum Simulation of Non-Equilibrium Dynamics

In order to exactly simulate the time dynamics of a quantum system classically you must first store the Hamiltonian. As previously mentioned, the large memory cost limits the size of the system you can simulate. Secondly, you must calculate the time evolution operator, $U(t) = e^{-iHt}$, a computationally costly task. Finally, you must perform the calculation $U(t)\,|\psi(0)\rangle$, which is again computationally

costly. In the following we outline how the time dynamics of a quantum system can be simulated on a digital quantum computer.

2.3.1 Suzuki-Trotter decomposition

To simulate time evolution of a system on a quantum computer we must be able to decompose the time evolution operator, $U(t) = e^{-iHt}$ as a product of the elementary gates available on the quantum hardware in use. Note, here we have restricted our focus to time independent and local Hamiltonians. In general, a Hamiltonian is the sum of many non commuting terms, that is

$$H = \sum_j H_j, \tag{2.10}$$

where $[H_i, H_j] \neq 0$. This poses a problem to experiments as, in practise, each term cannot be implemented simultaneously. Thus, it is common to turn to the Suzuki-Trotter decomposition [35, 36]. We first recall the Baker–Campbell–Hausdorff formula [37]. Consider the operator $U(t) = e^{i(\hat{A}+\hat{B})t}$ in which $\hat{A}$ and $\hat{B}$ do not commute in general, then

$$U(t) = e^{i\hat{A}t}e^{i\hat{B}t}e^{\frac{t^2}{2}[\hat{A},\hat{B}]}e^{-i\frac{t^3}{6}(2[\hat{B},[\hat{A},\hat{B}]]+[\hat{A},[\hat{A},\hat{B}]])} + \cdots . \tag{2.11}$$

Next we note that $U(t) = U(t/n)^n$ and consider large n such that $\frac{t^2}{n^2} \to 0$. Mathematically, this limit leads to the result

$$U(t) = \left(e^{i(\hat{A}+\hat{B})\frac{t}{n}}\right)^n = \lim_{n\to\infty}\left(e^{i\hat{A}\frac{t}{n}}e^{i\hat{B}\frac{t}{n}}\right)^n. \tag{2.12}$$

This is the Suzuki-Trotter decomposition [38]. For large but not infinite n, the error of the Suzuki-Trotter decomposition is $O(\frac{t^2}{n^2})$. However by using a symmetric decomposition we can reduce this error further such that [39]

$$U(t) \approx \left(e^{i\hat{A}\frac{t}{2n}}e^{i\hat{B}\frac{t}{n}}e^{i\hat{A}\frac{t}{2n}}\right)^n + O(\frac{t^3}{n^3}). \tag{2.13}$$

Thus, given an initial quantum state, $|\psi(0)\rangle$, and a Hamiltonian, $H = \sum_j H_j$, and that $\Delta t = \frac{t}{n} \ll 1$, the quantum state $|\psi(t)\rangle = U(t)|\psi(0)\rangle \approx (\prod_j e^{iH_j\Delta t})^{\frac{t}{\Delta t}}|\psi(0)\rangle$. Note, for simplicity we have not

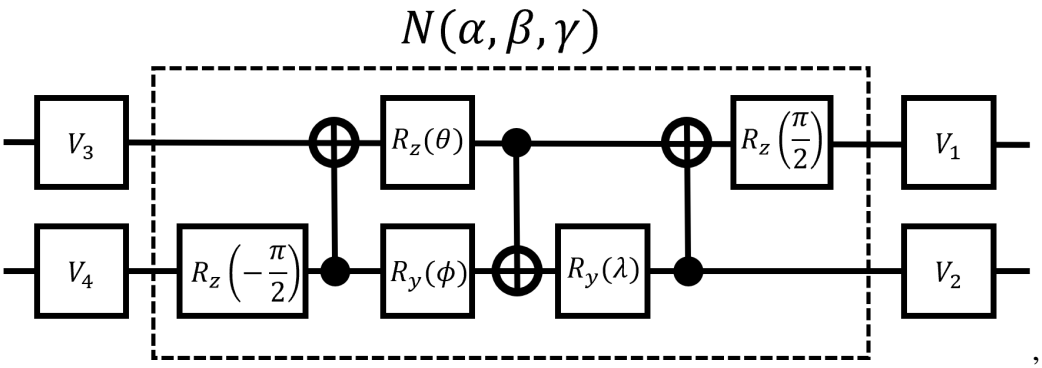

Figure 2.6: The quantum gate for $\mathcal{N}(\alpha,\beta,\gamma)$, here $\theta = \frac{\pi}{2} - 2\gamma$, $\phi = 2\alpha - \frac{\pi}{2}$ and $\lambda = \frac{\pi}{2} - 2\beta$.

considered the symmetric decomposition here.

2.3.2 Gate Decomposition

A digital quantum computer makes use of a universal set of quantum gates. Hence, it is important to be able to decompose a generic n-qubit unitary into the native gates in use. In this section, we will assume the native gates are CNOT, phase shift and rotation gates as these are the most popular choice in realised systems. It is clear by visualising the Bloch sphere depicted in Fig. 2.1 that any single qubit unitary can be achieved through the three rotation gates in combination with the phase shift gate. In particular, for the special case that $H = \sigma^\alpha$, in which α is x, y, or z, the gate corresponding to e^{-iHdt} is identically the native rotation gate $\mathcal{R}_\alpha(2dt)$.

However, a general multi-qubit unitary is non-trivial. Work done by Loïc Herviou *et. al.* [40] calculated the optimal circuit decomposition for the two qubit case. A general two qubit unitary can be decomposed as $U = (V_1 \otimes V_2)\cdot\mathcal{N}(\alpha,\beta,\gamma)\cdot(V_3 \otimes V_4)$, where V_i are single qubit unitaries and

$$\mathcal{N}(\alpha,\beta,\gamma) = \exp[i(\alpha\sigma^x \otimes \sigma^x + \beta\sigma^y \otimes \sigma^y + \gamma\sigma^z \otimes \sigma^z)]. \tag{2.14}$$

The quantum circuit of $\mathcal{N}(\alpha,\beta,\gamma)$ is shown in Fig. 2.6. It turns out that for quantum spin chain simulations, $\mathcal{N}(\alpha,\beta,\gamma)$ itself is highly useful as it allows us to simulate most commonly used Hamiltonians for condensed matter systems. For the case that $\alpha = 0$ and $\beta = 0$, i.e. $U = e^{i\gamma\sigma^z\otimes\sigma^z}$, which will be highly relevant in this thesis, the circuit diagram for $\mathcal{N}(\alpha,\beta,\gamma)$, simplifies to

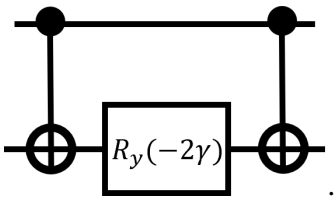

Figure 2.7: The quantum circuit for $U = e^{i\gamma\sigma^z\otimes\sigma^z}$.

While circuit decompositions of three qubit unitaries and beyond are known [41, 42], they require many composite gates to realise and thus are beyond the scope of this work.

While the qubit requirements of the quantum simulations methods introduced here have been linear, extracting the information encoded in the qubits after the implementation is non-trivial. It turns out that, while a system of N qubits can encode 2^N bits of information, only N bits of the data are accessible with each measurement - this is known as the Holevo bound [43]. Thus, in order to fully characterise a quantum state prepared on a quantum computer, an exponential number of measurements are required; this process is called *full state tomography* and is hugely inefficient. Thankfully, for many purposes the full quantum state is not required. A new technique for quantum simulation using NISQ devices has recently shown much promise, namely, randomised measurement methods [44].

2.4 Randomised Measurement Methods

In the family of randomised measurement protocols the fundamental idea is that, by repeating a simulation many times and performing measurements randomly sampled from a fixed ensemble, post-processing can be used to obtain details of the quantum state in consideration. This post-processing can be tailored for the characterization of topological order [45], for quantum chaos diagnostics [46] and more generally for machine learning problems for quantum many-body systems [47]. In this thesis we are interested in the use of randomised measurements to calculate the Rényi entropy of a system.

Entanglement is not only an important diagnostic for non-ergodic quantum dynamics such as thermalisation [48] and many-body localisation [49, 50] but also systems that generate high levels of

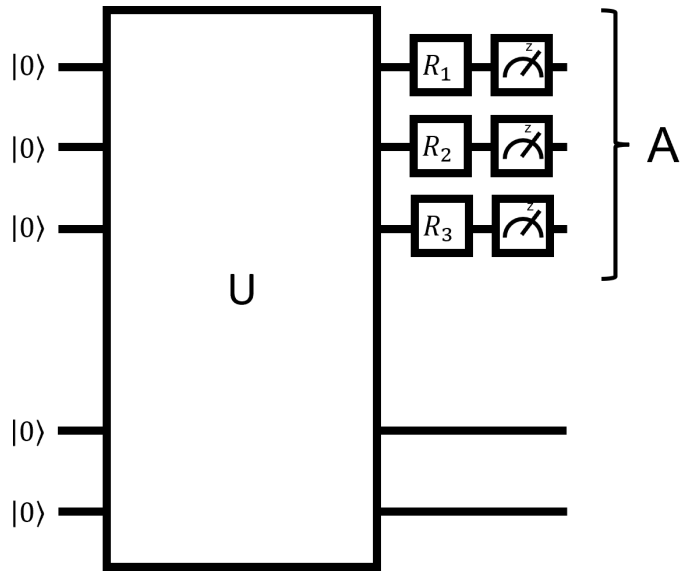

Figure 2.8: The circuit required to measure $\mathrm{Tr}(\rho_A^2) = \bar{X}$ of the subsystem A on a NISQ device. Here, U is the unitary that initialises the state of interest and R_i are random single qubit unitaries.

entanglement are required to achieve quantum advantage [51]. The level of entanglement in a system is typically probed via entanglement entropies. The n^{th}-order Rényi entropy is defined as

$$S^n(\rho_A) = \frac{1}{1-n} \log_2 \mathrm{Tr}(\rho_A^n), \tag{2.15}$$

where ρ_A is the reduced density matrix of the subsystem A. Note the special case of $n = 1$ which corresponds to the von Neumann entropy. The general process of measuring these Rényi entropies on a quantum device is outline in Ref. [52]. However, for the case of $n = 2$ there is a simplified protocol that is introduced in the following [53].

Consider a quantum circuit that initialises a quantum state via a unitary U. Given this quantum state, to measure the second-order Rényi entropy of the subsystem A we apply random single qubit gates on each of the qubit registers within the subsystem A, see Fig. 2.8. Here, each of these unitaries is taken from the circular unitary ensemble. These qubits are then measured in a fixed basis. Through repetition of this process, with a new set of unitaries drawn for each measurement, statistics can be obtained and $S^{(2)}(\rho_A)$ can be approximated by

$$S^{(2)}(\rho_A) = -\log_2 \bar{X}, \text{with } X = 2^{N_A} \sum_{s_A, s'_A} (-2)^{D[s_A, s'_A]} P(s_A) P(s'_A), \tag{2.16}$$

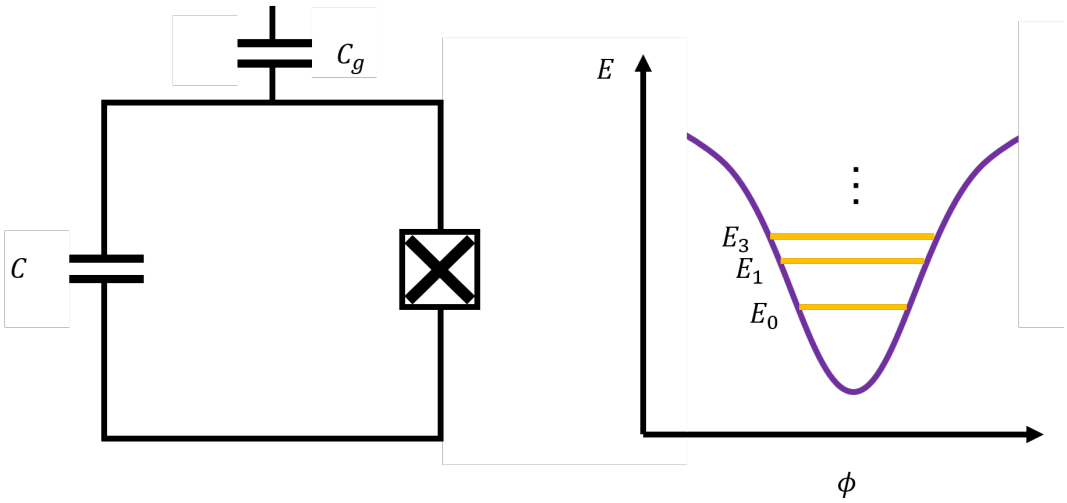

Figure 2.9: The simplest superconducting circuit that can be used as a qubit. Here, there is a capacitor in series with a Josephson junction (depicted by a cross). To interact this qubit with others, a gate capacitor is attached in parallel that will extend to other circuits. A schematic of the anharmonic energy levels of this circuit is also shown.

where s_A denotes a measurement outcome, $P(s_A)$ is the probability of measuring s_A, $D[s_A, s'_A]$ is the Hamming distance between s_A and s'_A (the number of positions at which the measured qubit states are different), N_A is the dimension of A and $\bar{X}$ denotes the ensemble average of X over the set of different random single qubit gates used. In Chapter 4 we present the first ever measurements of the second-order Rényi entropy on a digital quantum device.

2.5 Experimental Realisation of Quantum Computers

In this section we briefly summarise a number of commonly used platforms for building a digital quantum computer. The first experimental proposal to realise a CNOT gate was developed by Ignacio Cirac and Peter Zoller in 1994 for a trapped ion setup [54]. This was later achieved in 1995 by Christopher Monroe and David Wineland [55]. However, while this is a huge milestone in the experimental realisation of a quantum computer, a device able to perform an algorithm such as Shor's requires many logical qubits and the ability to perform deep, high fidelity circuits of many consecutive gates.

Many different physical systems have been used to build real devices. A popular experimental setup that has seen much financial backing by companies such as IonQ [56], Honeywell [57] and ORCA

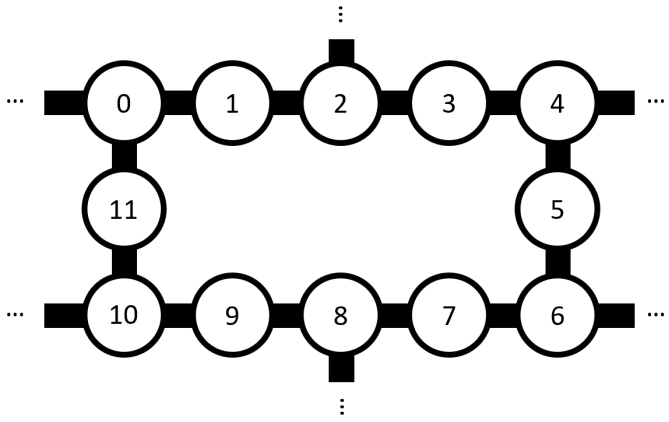

Figure 2.10: The unit cell of qubits used to build the IBM devices. Here, qubits are shown as numbered circles, and the connections between qubits is represented via solid black lines.

Computing [58] is a trapped ion setup. There has also been some work with neutral atoms by PASQAL [59] and planqc [60]. However, the most popular technology to build a quantum device is the superconducting qubit. These setups are built by companies such as Google [61], IBM [62], Rigetti [63] and Intel [64]. Throughout this body of work results were taken from the IBM digital quantum computers, thus these will be the focus of much of this thesis.

To realise a qubit it is required to isolate a two level quantum system from the environment. While both trapped ion and neutral atom qubits make use of the inherent properties of individual atoms, superconducting qubits use quantum effects on macroscopic degrees of freedom on superconducting circuits first proposed by Leggett [65]. A superconducting $LC-$circuit - consisting of an inductor, with inductance L, and capacitor, with capacitance C - is well described by a harmonic oscillator approximation. Here, the energy levels are equally spaced, thus, we are not able to isolate a two level system and these circuits do not make usable qubits. However, when the indicator is replaced by a Josephson junction the energy levels become anharmonic due to the non-linear inductance, see Fig. 2.9. The result is a unique energy gap between the two lowest energy levels which are therefore easily isolated. This idea is the foundation of the superconducting qubit which is the building block of the IBM quantum devices [66]. IBM has many NISQ devices that range from one qubit to 127 qubits [67]. The typical topology of these devices is built from rectangular unit cells of 12 qubits shown in Fig. 2.10. These devices typically have single qubit errors of $\mathcal{O}(10^{-3})$, two qubit gate errors of $\mathcal{O}(10^{-2})$ and measurement errors of $\mathcal{O}(10^{-2})$. Here, errors are defined by one minus the fidelity.

The thermal relaxation time, T_1 - defined as the time for a qubit to move from the excited state to the ground state - and coherence time, T_2 - defined as the time before a qubit's resonance frequency becomes unidentifiable - are $\sim 100\mu s$ with gate times $\sim 500ns$. To explicitly show the abilities of a NISQ device, in the next section a simple example of a shallow quantum circuit run directly on an IBM quantum computer is given.

2.5.1 Generating a Bell State on an IBM Device

As a simple example of the capabilities of an IBM quantum computer the results from a trivial quantum circuit that realises the Bell state $|\psi\rangle = \frac{|00\rangle+|11\rangle}{\sqrt{2}}$ is presented. The circuit to prepare such a state is simply two Hadamard gates, one applied to each qubit. Note, a Hadamard gate is defined as

$$\frac{1}{\sqrt{2}}\begin{pmatrix} 1 & 1 \\ 1 & -1 \end{pmatrix}. \tag{2.17}$$

These are then followed by a CNOT gate, see Fig. 2.11. When measuring this state with $10,000$ shots we would expect to see roughly half the measurement outcomes as 11 and half as 00. However, from Fig. 2.11 we see that while most the shots are in the expected states, there are some measurements of 10 and 01 indicating errors. Furthermore, there is a slight bias to the 00 state. As circuits get deeper this error accumulates and the physical signals become hard to interpret. There are two directions for dealing with such errors, namely the long term goal of implementing error correction codes as well as the short term fix of error mitigation; these two fields are introduced in the next section.

2.6 Errors in NISQ devices

Naturally in any experiment there are errors due to imperfect equipment and influence from the environment. In order to limit the effect of these errors in classical computers, we implement error correcting codes (ECC). The fundamental idea is to encode data with redundant information in such a way that the error can be detected and corrected. The original ECC was developed by Richard

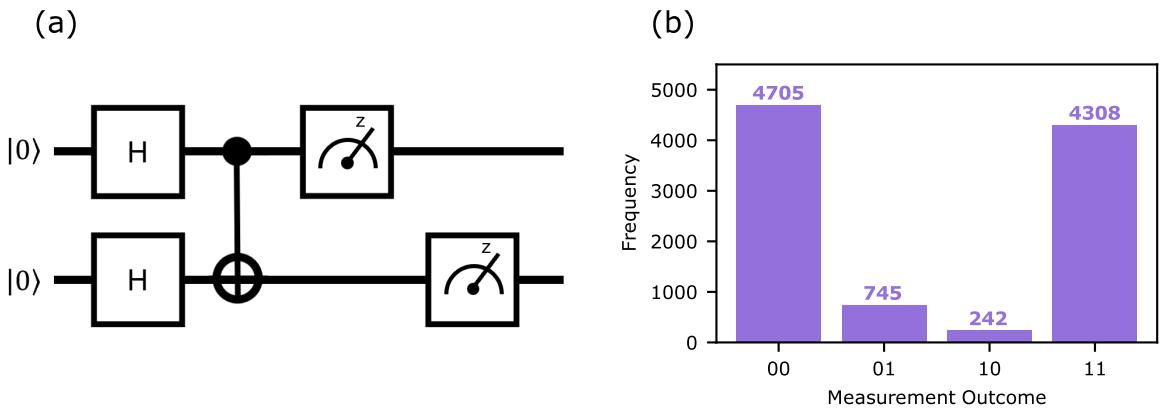

Figure 2.11: (a) The quantum circuit required to create the Bell state $|\psi\rangle = \frac{|00\rangle+|11\rangle}{\sqrt{2}}$. Here, a Hadamard gate is performed on each qubit, followed by a CNOT gate and finally each qubit is measured. (b) The results from running this circuit on the *ibmq_nairobi* [68].

Hamming in 1950 for classical computers, which is now called the Hamming Code [69]. The most simple form of this code is the $(n, 1)-$Hamming code, or the n-repetition code.

Given information in the form of a bit string, the idea behind n-repetition code is that instead of directly sending this message down a noisy information channel you send a bit string in which each element is repeated n times. For example, for $n = 3$ and the message '0', the transmitted message becomes '000'. This extended message is transmitted down the noisy communication channel and is received with some errors. For each n digits that correspond to a single bit in the original message, the message is read as the value that occurs most often. In our example, assume that the second bit in this message experiences a bitflip error, such that the received message after the noisy communication channel is '010'. This protocol will still read as the correct message '0', as there are two '0's and one '1', hence our error correction code has worked. Given the probability of bit error down the noisy communication channel is p, the probability of incorrectly reading the original message bit is $O(p^{\frac{n-1}{2}+1})$; with $p \ll 1$ the probability of error can be all but eradicated with n set as just a small integer.

This idea cannot be directly mapped onto qubits in a quantum computer due to the no-cloning theorem [70, 71], a general wavefunction cannot be replicated multiple times. Instead, the repetition code inspired the three-qubit bitflip code designed by Asher Peres in 1985 [72]. In this protocol the quantum state $\alpha|0\rangle + \beta|1\rangle$ is extended to the state $\alpha|0_L\rangle + \beta|1_L\rangle$ in which $|0_L\rangle = |000\rangle$ and $|1_L\rangle = |111\rangle$. This can be achieved through two CNOT gates and two ancillary qubits [27], see Fig. 2.12. This ex-

(a)

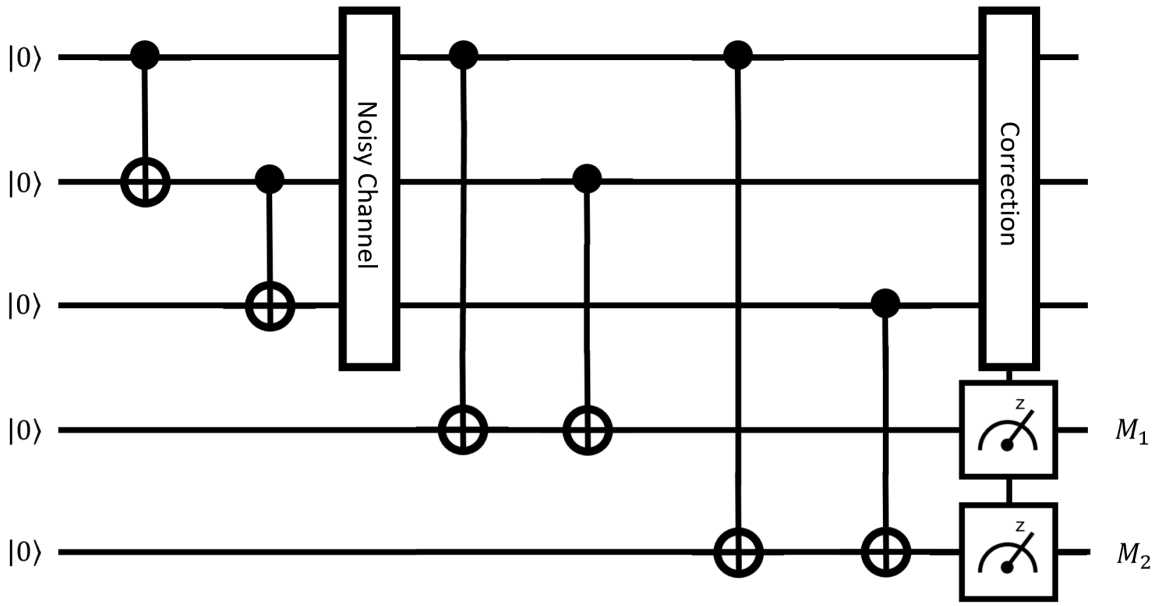

(b)

Message Received	M_1	M_2	**Correction**
$\alpha\|000\rangle + \beta\|111\rangle$	0	0	$I \otimes I \otimes I$
$\alpha\|100\rangle + \beta\|011\rangle$	1	0	$X \otimes I \otimes I$
$\alpha\|010\rangle + \beta\|101\rangle$	1	1	$I \otimes X \otimes I$
$\alpha\|001\rangle + \beta\|110\rangle$	0	1	$I \otimes I \otimes X$

Figure 2.12: (a) The quantum circuit to perform the three-qubit bitflip code. (b) A table highlighting the quantum gates required to correct bitflip error given measurements M_1 and M_2.

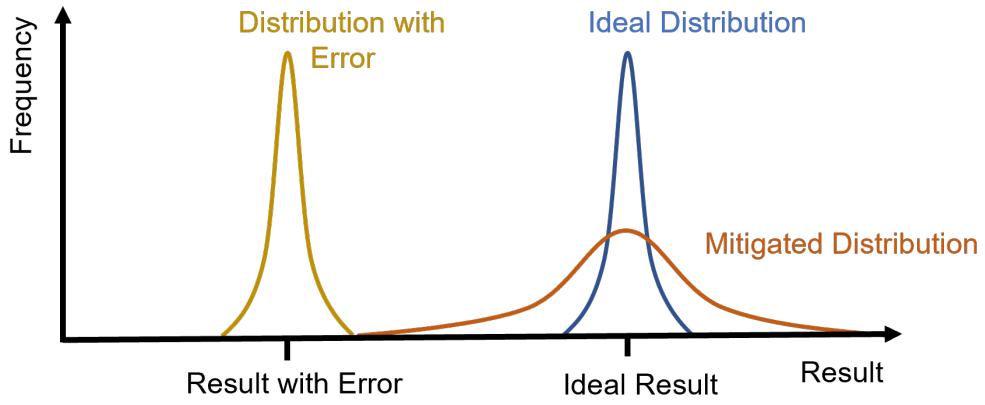

Figure 2.13: A schematic that shows the general effect of error mitigation schemes. The mean of the result obtain with error mitigation is closer the ideal result but the uncertainty in the results has increased from the unmitigated case [74]

tended message is then passed through the noisy quantum channel. Finally, assuming that at most one bitflip error has occurred, we are able to encode information about the state of the message into two more auxiliary qubits, such that, once these extra two qubits are measured we can locate the bitflip error. By simply acting a Pauli$-X$ gate on the corresponding qubit we can fix the error without collapsing the wavefunction of the original message. Further optimisations both in the required physical qubits to logical qubit ratio as well as in the level of error protection have been made in recent years; Ref. [73] gives a thorough review of current quantum ECCs. In practise, ECCs are beyond reach of NISQ devices. The reason for this can be understood from the example of the three-qubit bitflip code; to perform this ECC algorithm there were two requirements. Firstly, the probability of error was low, and secondly, we were able to add auxiliary qubits into the circuit. In NISQ devices, the inherent errors are large and we have limited numbers of qubits.

While NISQ devices are not able to use ECC algorithms, error mitigation techniques can be used. Error mitigation methods aim to estimate the effect of noise in a quantum simulation and infer what the error-free results would be. Typically these methods improve the mean result of a simulation but increase the variance. Error mitigation is a large area of research with many subfields. In particular, mitigation methods either aim to address measurement errors [75, 76, 77, 78, 79, 80, 81, 82, 83] or consider optimisation of an algorithm and/or deal with gate errors [84, 85, 86, 87, 88, 89, 90, 91]. There has been strong progress in this field but an effective general error mitigation method is yet to be discovered. Typically, mitigation protocols rely on high levels of control of the quantum device in

use, or, are designed for a specific algorithm i.e. exploiting specific symmetries [92]. One promising direction is to employ machine learning algorithms for error mitigation [93, 94, 95, 96]. In general these methods use the abilities of machine learning to learn the effect of error in noisy simulations and thus infer the error-free result. However, the implementation of such methods requires a large increase in classical computational overhead. These methods can also be somewhat uncontrolled. For example, many protocols are based on systematically increasing error in the device and then extrapolating back to the zero error case [89, 97, 98, 99, 100, 101, 102, 103]. Tuning the error rates is typically device dependant and the fitting process requires expert knowledge of the specific hardware. Throughout our work two standardised mitigation protocols are used that are introduced in the following.

2.6.1 Choosing the Layout of Qubits

In IBM devices measurement and gate errors vary from qubit to qubit - the error rates for each qubit in every device are available on the IBM website and are routinely updated [62]. Thus, it is important to choose the set of qubits within the machine that not only have the topology that you require but also that minimise the inherent errors. The method chosen in this work is as follows. We define the total error of a set of qubits as

$$E_{tot} = \sum_i \alpha e_i^{CNOT} + \sum_j \beta e_j^{U3} + \gamma e_j^M , \tag{2.18}$$

where, e^{CNOT} is the CNOT gate error, e^{U3} is the single qubit gate error, e^M is the measurement error, α, β and γ are weightings that allow for the prioritisation of different errors, i labels the connections between qubits and j labels the qubits. By calculating E_{tot} for each set of qubits with the desired topology, we are able to select the set of qubits that have the lowest error rates. In this work we choose $\alpha = 1$, $\beta = 1$ and $\gamma = 0$ as deep circuits have many gates but are only measured once, hence gate error is more important to minimise. Note, this protocol method only works in small system sizes but in the NISQ era it is sufficient.

2.6.2 Measurement Error Mitigation

Qiskit is an open-source interface for working with quantum computers remotely [75]. Within the Qiskit package there are many available protocols for different quantum computer applications. In particular, a measurement mitigation package is utilised throughout this body of work.

Consider a system of N qubits in which a subset of N_m are to be measured. These N_m qubits span a 2^{N_m} dimensional Hilbert space that can be spanned by a basis of the z-polarised product states. The measurement mitigation employed by Qiskit works as follows. The subset of N_m qubits are initialised into each of the individual z-polarised basis states and measured. From this a mapping matrix from the ideal results to the measured results can be made

$$R_{noisy} = M R_{ideal}, \tag{2.19}$$

where R_{noisy} are the measured results, M is the mapping matrix, and R_{ideal} are the expected results on a fully fault tolerant device. Once M is known, we are able to invert the equation to obtain a mapping from the noisy measurements to the ideal results

$$R_{ideal} = M^{-1} R_{noisy}. \tag{2.20}$$

For example, assume we are measuring a system of two qubits, i.e. $N_m = 2$. These qubits are initialised in each of the states 00, 01, 10 and 11 separately and are measured. From this we obtain the probability of measuring the state j given we initialised in state i, $P_{(i,j)}$. From this we build the matrix M as:

$$M = \begin{pmatrix} P_{(00,00)} & P_{(00,01)} & P_{(00,10)} & P_{(00,11)} \\ P_{(01,00)} & P_{(01,01)} & P_{(01,10)} & P_{(01,11)} \\ P_{(10,00)} & P_{(10,01)} & P_{(10,10)} & P_{(10,11)} \\ P_{(11,00)} & P_{(11,01)} & P_{(11,10)} & P_{(11,11)} \end{pmatrix}. \tag{2.21}$$

Note, for the zero error case this matrix will be the identity. This matrix is simple to invert and thus we can obtain the desired M^{-1}. While this measurement mitigation method works well for small systems, the number of basis states grows exponentially with system size. Scalable methods of measurement

error mitigation is a current area of research [104, 105].

Despite using both of these error mitigation techniques, namely, carefully choosing the correct layout of qubits as well as measurement error mitigation, we have found that for observing nontrivial confinement dynamics the noise on the device is still too large to obtain physical results. Thus, we developed a novel error mitigation protocol that is not only is generally applicable, but also highly effective. This method is presented in Chapter 5.

Chapter 3

Confinement Dynamics

In this chapter the physical phenomenon that we have chosen for our quantum simulation efforts, namely confinement, is introduced. In doing so, we will also justify why it was chosen. The elementary particles, quarks, are never found in isolation in nature. The reason for this is that the interaction strength between two quarks grows as a function of their separation. As a consequence the energy required to split a meson, a two-quark particle, is sufficient to excite a new quark anti-quark pair, the result of which is the creation of two mesons – a phenomenon known as string breaking [106]. The description of this physics is given by quantum chromodynamics (QCD). The mathematical underpinning of QCD is the Yang-Mills theory, which is still an active area of research. In fact, the unsolved Yang–Mills existence and mass gap problem is famous in mathematical physics, the solution of which would prove there is a lower bound on the mass of glueballs – a particle made up of many gluons. The Yang–Mills existence and mass gap problem is one of the seven Millennium Prize Problems defined by the Clay Mathematics Institute, eaching having a prize of US $\$1,000,000$ for any individual able to solve them [9]. This exemplifies the importance put on a full understanding of confinement physics. Furthermore, confinement is an example of a non-perturbative quantum many-body effect, which makes it extremely difficult to simulate on a classical computer.

3.1 Two Particle Model

Many experiments have shown that the confinement potential between quarks is proportional to their spatial separation at large distances [107]. The simplest model of two confined quarks is the one dimensional Schrödinger equation for a two particle system moving in a potential proportional to the difference in their real space coordinates. Given the position of two particles of mass $m/2$ and positions x_1 and x_2, this system is described by

$$\frac{-2\hbar}{m}\left[\frac{\partial^2}{\partial x_1^2}+\frac{\partial^2}{\partial x_2^2}\right]\psi(x_1,x_2)+C|x_1-x_2|\psi(x_1,x_2)=E\psi(x_1,x_2), \tag{3.1}$$

where $\hbar$ is the Planck's constant, C is the gradient of the potential, and E is the system's energy. By defining $x=x_1-x_2$, we obtain the centre of mass Schrödinger equation

$$\frac{-\hbar}{m}\frac{d^2}{dx^2}\psi(x)+C|x|\psi(x)=E\psi(x). \tag{3.2}$$

Due to the symmetry of the potential around $x=0$ we have to consider both a symmetric solution - the particles are bosons - and skew-symmetric solution - the particles are fermions. Assuming a skew-symmetric wave function, $\psi(x)=-\psi(-x)$, we obtain the boundary condition $\psi(0)=0$ for continuity. Similarly, for a symmetric wavefunction $\psi(x)=\psi(-x)$ the boundary condition is such that $\frac{d}{dx}\psi(0)=0$. If we consider the dimensionless variables ϵ and y such that

$$E=\epsilon\left(\frac{C^2}{m\hbar^2}\right)^{\frac{1}{3}}, \qquad y=x\left(\frac{\hbar^2}{mC}\right)^{\frac{1}{3}}, \tag{3.3}$$

and consider the transformation $z=y-\epsilon$, we are left with the differential equation

$$\frac{d^2}{dz^2}\psi(z)-z\psi(z)=0. \tag{3.4}$$

This differential equation has linearly independent solutions that correspond to the Airy functions, $\psi(z)=\alpha\mathrm{Ai}(z)+\beta\mathrm{Bi}(z)$. For normalisation of the wavefunction we require that $\beta=0$, and as a consequence $\alpha=1$. Due to the boundary condition at $x=0$, the energies are given by $Ai(-\epsilon)=0$ and $Ai'(-\epsilon)=0$ for the skew-symmetric and symmetric cases respectively. In Fig. 3.1 we plot the

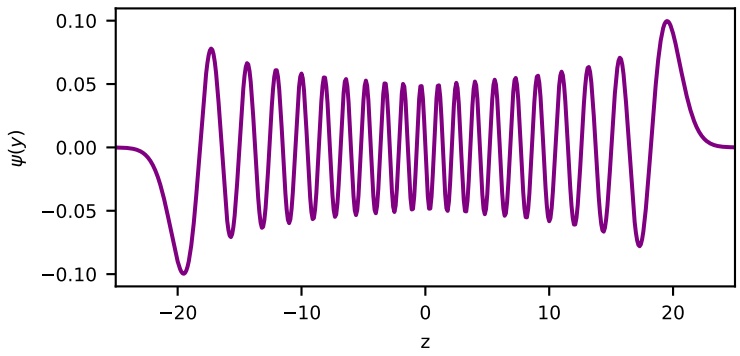

Figure 3.1: The wavefunction for the 20^{th} energy level. We see the turning points at $|y| \sim 20$, these correspond to the limits in the particle separation due to the confining potential.

wavefunction for the 20^{th} energy level. We clearly see that, while the two particles have a nonzero probability to be found at a varying number of distances, there are turning points for $z \sim 20$ which correspond to $|y| = \epsilon$. Physically these are interpreted as the maximal separation between two particles, i.e. the particles are confined together to form a meson.

3.2 Confinement in Spin Chains

It turns out that many simple condensed matter systems also exhibit confinement physics, for example domain-wall confinement in quantum spin chains. Examples include the transverse field Ising model (TFIM) with an additional longitudinal field [108, 1, 3], the TFIM with long-range interactions [12, 4], the lattice Schwinger model [13, 109] and the Potts Model [110, 111, 112, 113]. Not only are these spin systems much simpler to analyse than full QCD, they also map easily map onto a quantum computer – making them a prime target for near term quantum simulation efforts. In our work we consider additions to the TFIM that induce confinement dynamics between the native excitations, namely, a longitudinal field and long-range interactions. In the follow section, we first introduce the pure one dimensional TFIM, its properties and exact solutions.

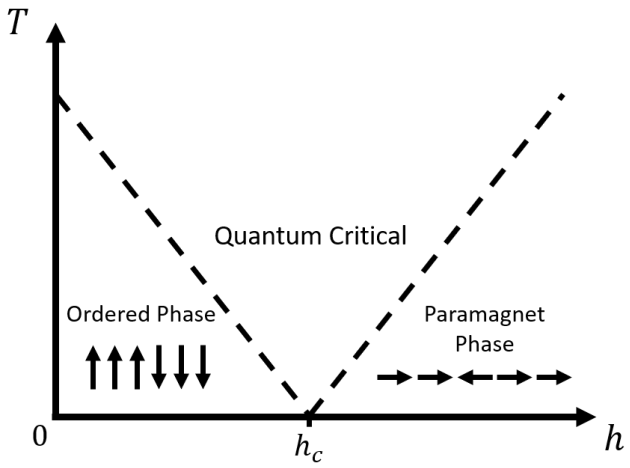

Figure 3.2: The phase diagram for the one dimensional transverse field Ising model.

3.2.1 The Transverse Field Ising model

The one dimensional TFIM is given by the following Hamiltonian

$$H = -J\left[\sum_i \sigma_i^z \sigma_{i+1}^z + h\sum_i \sigma_i^x\right], \tag{3.5}$$

where the basis considered is the z-polarised product states, i.e. a basis state is given by $|\psi\rangle = \bigotimes_{i=0}^{N} |a_i\rangle$ where, i labels the site, N is the length of the spin chain and a_i is either $\uparrow$ or $\downarrow$. Here, J is the Ising exchange of nearest neighbour spin-$1/2$ and h is the relative strength of the transverse field. The TFIM can be exactly diagonalised via a Jordan-Wigner and subsequent Bogoliubov transformations and describes free fermions, see the Appendix A.1 for details. The resulting form of the Hamiltonian is

$$H = \sum_q \omega(q)\eta_q^\dagger \eta_q, \tag{3.6}$$

$$\omega(q) = 2J\sqrt{1 - 2h\cos k + h^2}, \tag{3.7}$$

where, $\eta_q^\dagger$ are fermionic operators. For a transverse field strength below its critical value, $h_c = J$, ($J > 0$) the fermions are well approximated by domain-wall excitations $|... \uparrow\uparrow\downarrow\downarrow ...\rangle$ [108]. These domain-walls are topological excitations interpolating between the two degenerate ground states. This is the ordered phase. For a transverse field strength above the critical value, the paramagnetic phase, the fermions are spin-flip quasiparticles $|... \rightarrow\rightarrow\leftarrow\rightarrow\rightarrow ...\rangle$, see Fig. 3.2.

While a non-zero transverse field in principle breaks the conservation of domain-walls, providing the transverse field strength is small, resonances between different particle number states are greatly suppressed and can be safely neglected [114]. This can be understood simply by noting that the energy cost to create new domain-wall excitations is of the order J and, given that the transverse field is the source of dynamics of spins, if $J \gg h$ there are large energy gaps between subspaces of varying numbers of domain-walls. Thus, we can accurately understand non-equilibrium dynamics by projecting the full Hilbert space into subspaces with a conserved number of domain-walls as long as we remain in the limit $h \ll J$.

3.2.2 The Transverse Ising Model with a Longitudinal Field

Perhaps the simplest model that exhibits confinement effects is the one-dimensional TFIM with an additional longitudinal field [10, 11]. In the limit of negligible longitudinal field strength, we recover the freely propagating domain-wall excitations. However, with the introduction of a non-negligible longitudinal field strength the $\mathcal{Z}_2$ spin-flip symmetry is broken. The Hamiltonian of the TFIM with an additional longitudinal field is given by

$$H = -J\left[\sum_i \sigma_i^z \sigma_{i+1}^z + h_x \sum_i \sigma_i^x + h_z \sum_i \sigma_i^z\right], \tag{3.8}$$

where $h_{x/z}$ are the relative strengths of the transverse and longitudinal fields. In this work we restrict our focus to transverse field strengths below the critical value, $h_c = J$, in the ordered phase, where fermions are approximately described by domain-walls excitations $|... \uparrow\uparrow\downarrow\downarrow ...\rangle$. The addition of a longitudinal field lifts the degeneracy of the ground state and gives rise to a confining potential between domain-walls strongly affecting the non-equilibrium dynamics of the system. An established way to elucidate the confinement physics is to study the dynamics in a restricted two domain-wall subspace. We project Eq. 3.8 into the two domain-wall subspace written in the basis $|j, n\rangle = |\uparrow\uparrow ... \uparrow\downarrow_j ... \downarrow_{j+n-1}\uparrow .. \uparrow\uparrow\rangle$. Note, for periodic boundary conditions $0 \leq j < N$ and

$0 \leq n < N$. This gives $\mathcal{H} = P^{-1}HP$, in which P is the projection operator and

$$\begin{aligned}\mathcal{H} = &- h_x \sum_{j,n} \left[|j, n+1\rangle + |j, n-1\rangle + |j+1, n-1\rangle + |j-1, n+1\rangle \right] \langle j, n| \\ &+ \sum_{j,n} V(n) \, |j, n\rangle \, \langle j, n| \, ,\end{aligned} \tag{3.9}$$

where we have set $J = 1$, removed constant terms and $V(n) = 2h_z n$. The first term of this subspace Hamiltonian is a kinetic term that allows the domain-walls to 'hop', and the second term is the effective potential, $V(n)$, linearly increasing with domain-wall separation n. As a result, domain-walls are bound together and form mesons. This spin chain model has been an exciting area of research in recent years due to its experimental relevance [115, 116, 117, 1].

Recovering the Airy Function Wavefunctions

By analysing this system in the semiclassical limit - where we now ignore lattice effects - we are able to recover the Airy wavefunction solutions as in the continuous two particle model from Eq. 3.2. Consider the weakly confined region, i.e. h_z small but not zero. In this limit we can obtain a semiclassical system in which the phase space of the two fermions belonging to a meson is labeled by the momentum and position of each fermion, (k_1, x_1) and (k_2, x_2). The dynamics are governed by the effective Hamiltonian

$$H_{cl} = \omega(k_1) + \omega(k_2) + 2\bar{\sigma} h_z |x_1 - x_2| \tag{3.10}$$

where $\omega(k)$ is given by Eq. 3.7 and $\bar{\sigma} = (1 - h_x^2)^{\frac{1}{8}}$ is the expectation value of $\langle \sigma^z \rangle$ for $h_z = 0$ [118]. Note, that in the classical case the coordinates x_1, x_2 are continuous and we consider an infinite system. The derivation of this Hamiltonian is given in full in Appendix A.2. By considering the coordinates of the center of mass $X = (x_1 + x_2)/2$, $P = (k_1 + k_2)/2$ and relative coordinates $x = x_1 - x_2$, $p = k_1 - k_2$, this Hamiltonian becomes

$$H_{cl} = \epsilon(p; P) + 2\bar{\sigma} h_z |x| \tag{3.11}$$

where $\epsilon(p; P) = \omega(p + P/2) + \omega(p - P/2)$. Physically, $\epsilon(p; P)$ can be interpreted as the kinetic energy of the meson and $2\bar{\sigma} h_z |x|$ as the confining potential. Conservation of energy and momentum

give us the following conditions

$$\epsilon(p(t);P) + 2\bar{\sigma}h_z|x(t)| = E = \text{const}, \qquad P(t) = \text{const}. \tag{3.12}$$

From here we consider the limit of small momentum, $p \ll 1$, in which

$$\epsilon(p;P) \approx \epsilon(P) + \partial_P^2\epsilon(p;P)|_{p=0}\, p^2/2. \tag{3.13}$$

Given that this Hamiltonian is quadratic in the momentum, the problem is reduced to a Schrödinger equation in the exact form of Eq. 3.2 and we recover Airy function solutions:

$$\frac{1}{2}\partial_p^2\epsilon(p;P)|_{p=0}\,\frac{d^2}{dx^2}\psi(x) + 2\bar{\sigma}h_z|x|. = (\epsilon(P)+E)\psi(x). \tag{3.14}$$

Eigenvectors and Energies of the Two domain-wall Subspace

Away from the semiclassical limit it is possible to fully diagonalise the two domain-wall subspace Hamiltonian and obtain the fully quantum mechanical energy levels retaining the lattice effects. We note that Eq. 3.9 has translational symmetry in j, allowing us to take the Fourier transform, $|k,n\rangle = \frac{1}{\sqrt{L}}\sum_j \exp\big(-ik\frac{n}{2} - ikj\big)\,|j,n\rangle$, obtaining

$$\mathcal{H} = \sum_{k,n}\Big[V(n)\,|k,n\rangle\langle k,n| - 2h_x\cos\frac{k}{2}\big(\,|k,n\rangle\langle k,n-1| + |k,n\rangle\langle k,n+1|\,\big)\Big] \tag{3.15}$$

which, for an infinite chain can be diagonalised using the transformation

$$|k,\alpha\rangle = \sum_n C_\alpha \mathcal{J}_{n-\nu_{k,\alpha}}(x_k)\,|k,n\rangle\,, \tag{3.16}$$

where $\nu_{k,\alpha} = \frac{E_{k,\alpha}}{2h_z}$, $x_k = \frac{2h_x\cos\frac{k}{2}}{h_z}$, $\mathcal{J}$ is the Bessel function of the first kind and the coefficient C_α is used for normalisation [114]. See Appendix A.3 for details. The energy levels $E_{k,\alpha}$ can be computed via the boundary condition that $\mathcal{J}_{-\nu_{k,\alpha}}(x_k) = 0$. In fact, using the correct asymptotic approximations of the Bessel functions, it is possible to recover the semiclassical Airy function solutions from this result as well [118].

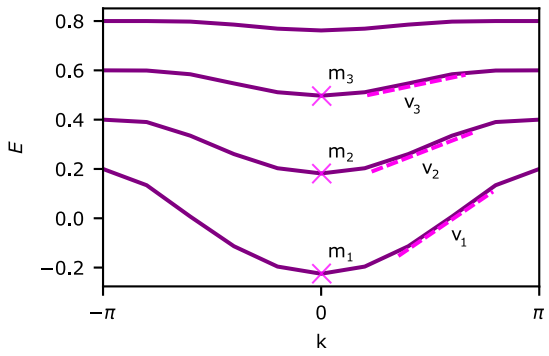

Figure 3.3: The energy levels of the two domain-wall subspace for $N = 10$, $J = 1$, $h_x = 0.2$ and $h_z = 0.1$. Given that the energy of the polaraised state has been shifted to zero, the minima of each energy level corresponds to a meson mass. The lowest three meson masses have been marked. Furthermore, the meson velocity is given by the group velocity, or $\frac{\partial E}{\partial k}$. The first three maximal meson velocities, the maximal gradients of the energy levels, have been marked.

3.2.3 The long-range Ising Model

Confinement can also be induced between the fermionic excitations in the TFIM through the addition of long-range interactions. The one dimensional Ising spin chain with long-range interactions is given by

$$H = -\sum_{i,r} \frac{J}{r^\alpha} \sigma_i^z \sigma_{i+r}^z - h \sum_i \sigma_i^x \tag{3.17}$$

where r denotes the distance between two sites. Again, we are interested in the regime where the transverse field is weak $h \ll J$. In the limit of large α, the short-ranged TFIM is recovered and the fermion excitations freely propagate. As α is reduced, longer ranged domain-wall interactions are induced. We can again project the full Hilbert space into the two domain-wall subspace using the basis $|j, n\rangle$ resulting in a Hamiltonian of the same form as Eq. 3.9, however, this time inducing a confining potential (for an infinite chain) of the form

$$V(n) = 4n\zeta(\alpha)J - 4J \sum_{1 \le l < n} \sum_{1 \le r \le l} \frac{1}{r^\alpha}, \tag{3.18}$$

where $\zeta(\alpha)$ is the Riemann zeta function [12]. For $\alpha < 1$ the potential $V(n)$ diverges, signaling a transition to an infinitely-long-ranged model without well-defined local excitations. Therefore we will always consider the regime $\alpha > 1$. For $\alpha > 2$, this potential is a monotonically increasing function of n with a finite maximum $\lim_{n\to\infty} V(n) = V_{\text{max}} < +\infty$. In contrast, in the regime $1 < \alpha < 2$, $V(n)$ is

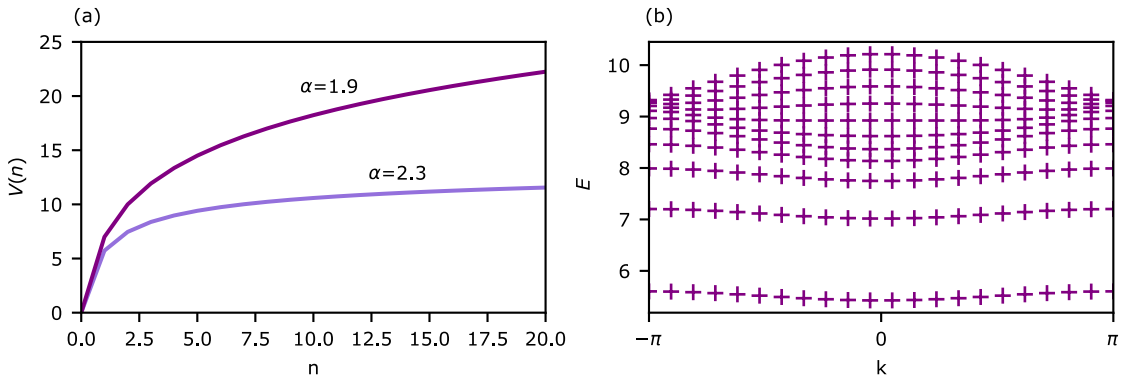

Figure 3.4: (a) The potential between two domain-walls as a function of their separation in the long-range Ising model for an infinite chain. Here, $J = 1$ and $h = 0.27$. For $\alpha = 2.3$ we see that the potential is bounded above and is not a truly confining potential. However, for $\alpha = 1.9$ this potential grows indefinitely and thus induces confinement dynamics. (b) The energy levels of the two domain-wall subspace with $J = 1$, $h = 0.27$, $\alpha = 2.3$ and $N = 22$. We clearly see boundstates for low energies but a continuum at high energies. This is due to the bounded nature of the domain-wall potential for $\alpha > 2$.

unbounded and domain-walls cannot be pulled infinitely far apart without paying infinite energy, thus exhibiting strict confinement. While there is no known transformation to diagonalise this Hamiltonian analytically, in Fig. 3.4 the energy levels calculated numerically are presented.

3.3 Signatures of Confinement

It was Marton Kormos *et. al.* [108] that first showed the effects of confinement on the non-equilibrium dynamics of a spin chain model. In their work, they consider the dynamics after a quantum quench in the TFIM with an additional longitudinal field of varying strengths. They define the 'masses' of mesons as the gap between the ground state and a meson energy level and show how spectroscopy can be performed to measure these from the measurements of magnetisation. Secondly, they show the slowing of correlation spread due to meson formation. In fact, this slower correlation results in a subtle light cone in which the gradient can be related to the maximal velocities of the mesons. Finally, they show that entanglement is suppressed due to confinement, and that the amount of suppression is directly linked to the longitudinal field strength. Later, Fangli Liu *et. al.* [12] showed similar signatures of confinement in the non-equilibrium dynamics of the long-range TFIM. Again, they showed how spectroscopy can be used to measure the meson masses and how the correlation spread

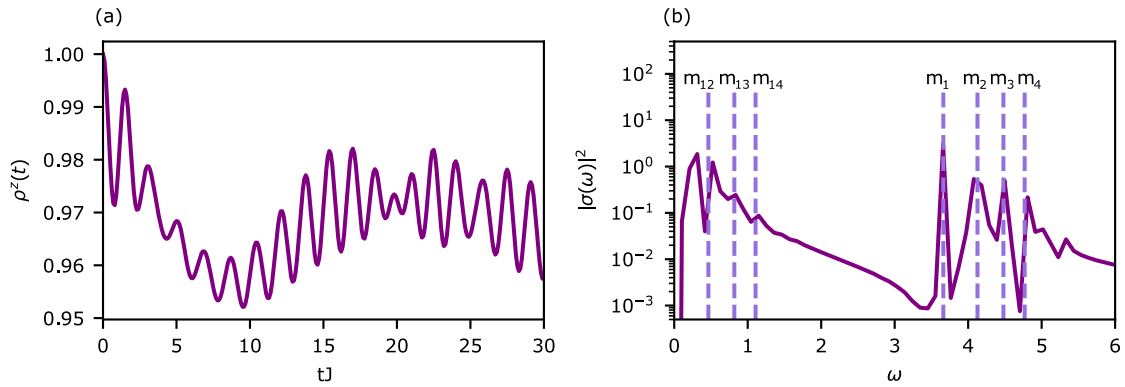

Figure 3.5: (a) Real-time dynamics of the local magnetisation. The initial state is fully polarised and the Hamiltonian parameters are $h_x = 0.1$, $h_z = 0.25$ and $N = 11$. (b) The power spectrum of these dynamics, clear peaks are seen that match with the theoretical predictions of meson masses from the two domain-wall approximation.

is suppressed due to confinement. In their work they go on further to show how confinement prolongs the time for the system to thermalise. These effects can be considered signatures which we use as evidence that the physics being observed in this thesis is the result of quasi-particle confinement. In the next section we directly show these signatures of confinement as well as discuss their viability in the context of a NISQ device.

3.3.1 Meson Masses

In the pure TFIM, the real time dynamics of the local magnetisation after a quantum quench, namely,

$$\rho_i^z(t) = \langle \psi(t) | \, \sigma_i^z \, | \psi(t) \rangle \, , \tag{3.19}$$

exponentially decays to zero [119]. However, the introduction of a confining potential halts this decay and leads to persistent oscillations. This can be seen in Fig. 3.5 (a). The 'masses' of the mesons formed by the domain-wall pairs are defined by the difference between energy levels and the ground state; these masses are marked on Fig. 3.3. Note, in the two domain-wall subspace calculations the ground state energy has been shifted to zero. As a first clear signature of confinement, these masses can be extracted from the most prominent frequencies in the measurements of local magnetisation in the real time dynamics from a low energy initial state via spectroscopy, see Fig. 3.5.

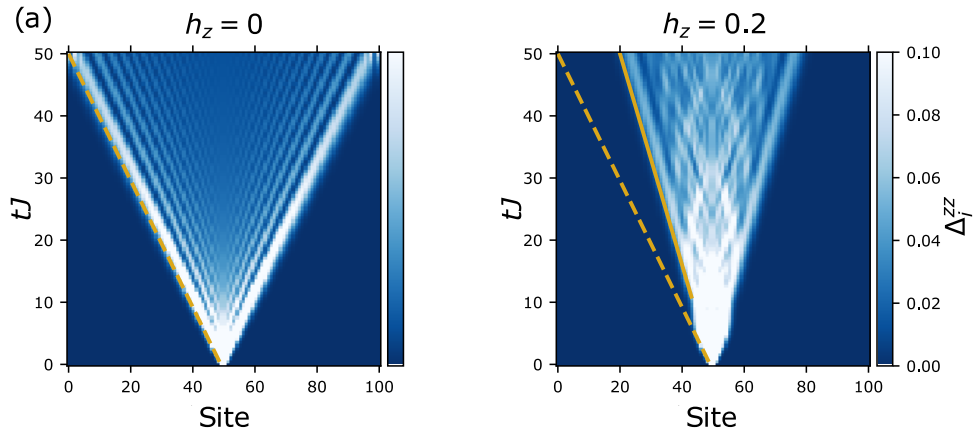

Figure 3.6: Real time dynamics of domain-wall positions within the two domain-wall subspace following a quantum quench to the TFIM without and with additional longitudinal field h_z. These results are calculated via exact diagonalisation of the two domain-wall subspace. Here, $L = 101$, $h_x = 0.5$ and the initial state is ferromagnetic with a single flipped spin in the centre. (a) $h_z = 0$, the light cone structure of free particles is visible. (b) $h_z \neq 0$, two velocities are observable, an initial velocity (dashed) equal to the free case and the meson velocity (solid) at longer times [1].

While classically this signature of confinement is easy to perform, when considering this method of meson mass extraction in the context of a NISQ device, we see that the precision requirements are large to perform; the amplitude of the oscillations is small and there are many contributing frequencies to capture. Hence, long times are needed. In work done by W. L. Tan *et. al.* [120] it is shown how one can vary the dominant frequency observed by choosing a particular initial state that has a large overlap with the energy level corresponding to the desired meson mass. This in turn allows the masses of mesons in the long-range TFIM to be measured in a trapped ion set up and makes the meson mass measurements viable for a NISQ device.

3.3.2 Meson Velocities

As quasi-particles move through the spin chain they spread quantum correlations. Due to the Lieb-Robinson bound [121] there is a maximal velocity, v_{max}, in which these quasi-particles can propagate and all connected correlations at distance l vanish for times $t < l/2v_{max}$. This can be seen through the measurement of the light cones produced by the two point correlation function, namely

$$\rho_{i,j}^{zz}(t) = \langle\psi(t)|\, \sigma_i^z \sigma_j^z \,|\psi(t)\rangle - \rho_i^z(t)\rho_j^z(t). \tag{3.20}$$

Marton Kormos *et. al.* [108] compared the correlation spread in the free fermion case with the confined region. In the free case, a simple linear light cone was observed with a velocity given by the maximal gradient of the TFIM dispersion relation, $v = \frac{\partial E}{\partial k} = 2J\text{min}(1, h_x)$. However, in the meson dynamics, two velocities are seen, an initial velocity, as well as a second slower velocity, see Fig. 3.6. This initial velocity agrees with the free domain-wall motion described by the pure TFIM and the second velocity is interpreted as the maximal *meson* velocity; as this meson velocity is slower than the free fermion velocity, confinement suppresses correlation spread. This second velocity can be directly calculated via the maximal gradient of the energy levels shown in Fig. 3.3. This provides another smoking gun signiture of confinement in the spin chain.

In order to observe this meson velocity, Marton Kormos *et. al.* [108] presented results saturated at $\rho^{zz}_{i,j}(t) < 10^{-5}$. With classical computers able to reach a precision far beyond this level, this is a clear signature of confinement. On a NISQ device, the errors are orders of magnitude larger than 10^{-5} and thus, in the context of observing this signature of confinement on a NISQ device the required precision is far beyond reach. However, by using an altered correlation function, in particular

$$\Delta^{zz}_i = \langle\psi(t)| \frac{1}{2}(1 - \sigma^z_i \sigma^z_{i+1}) |\psi(t)\rangle \,, \tag{3.21}$$

that explicitly measures the position of domain-walls, these two velocities are visible at $O(10^{-1})$, and the meson velocity becomes a viable signature of confinement for a NISQ device, see Fig. 3.6.

3.3.3 Entanglement Spread

Another key signature of confinement is the suppression of entanglement entropy spread [108]. Similarly to correlation spread, entanglement is carried throughout the spin chain via quasi-particle dynamics; given that there is a maximal velocity in which these quasi-particles can move, we expect to see a linear growth. However, with the introduction of a confining potential this growth is suppressed in a characteristic fashion; the stronger the confining potential, the slower entanglement spreads, see Fig. 3.7.

While this signature of confinement requires less precision than both the meson masses and velocities,

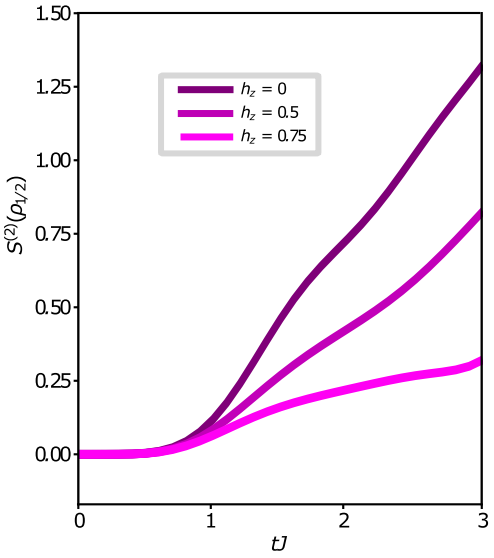

Figure 3.7: The half chain second order Réyni entropy for the transverse field Ising model with varying longitudinal field strengths. Here, $J = 1$, $h_x = 0.5$ and $N = 6$. With no longitudinal field, clear linear entropy growth is observed. As a longitudinal field is introduced the entropy spread is suppressed. This suppression is greater for larger h_z.

in general, entanglement entropy is not easy to calculate on a real quantum computer as it requires some form of state tomography. However, as presented in Chapter 2.4, a method to measure the second order Rényi entropy was developed by Tiff Brydges *et. al.* [53] via the use of randomised measurement. This makes the suppression of entanglement spread a viable signature to observe confinement on a NISQ device.

Given these signatures of confinement observable in the real time dynamics of spin chains, in the next chapter we present the first realisation of a non-perturbative quantum phenomenon on a digital quantum computer.

Chapter 4

Digital Quantum Simulation of Confinement Dynamics

In order to use current NISQ devices as new tools for quantum simulation, it is necessary to carefully design the measurement setup to obtain unambiguous signatures. There are many factors to take into account. The first step is understanding the capabilities of the device at your disposal; in this work we had access to the IBM digital quantum computers, thus, these will be the focus of the following discussion. In particular, the IBM devices have few qubits arranged with a topology that has limited connectivity. As a result, to simulate two dimensional systems or long-range interactions would require many SWAP gates, each of which is comprised of three CNOTS. With the CNOT error on the scale of $\mathcal{O}(10^{-2})$, such systems are beyond reach. Hence, we are limited to short, one dimensional nearest neighbour models. In Section 2.3, the gate decomposition of the time evolution operator for a given Hamiltonian was introduced. When simulating time dynamics on a quantum device, there are two types of errors to be aware of: error from the Suzuki-Trotter approximation - in practise we are incapable of using the limit of infinite Trotter steps - as well as the gate errors introduced with each Trotter step. This consideration strongly restricts the times that can be accurately simulated on a NISQ device. For long times we require many Trotter steps for accurate results but many Trotter steps lead to a deep quantum circuit that in turn results in large gate errors. Thus, any quantum phenomenon to be simulated is required to be observable in short times.

With these considerations, confinement dynamics in the TFIM with a longitudinal field is an ideal choice for simulation efforts. The Hamiltonian is simple, comprised of just one and two qubit interactions and the effects of confinement are observable in short times and in small systems. We begin by introducing the quantum circuit that is required to simulate this physics on an IBM quantum computer. This chapter closely follows the work published in Ref. [1].

4.1 Quantum Circuit and Initialisation

In order to observe confinement dynamics on a quantum computer, we need the ability to prepare the desired initial quantum state as well as realise the time evolution operator. The initial states that are considered in this chapter are all product states aligned in the z-direction. Given that the IBM devices naturally initialise qubits in the up z-polarised state, all initial states can be prepared simply by using Pauli-X gates to flip the desired spins.

In order to implement time dynamics onto a quantum computer we decompose the time evolution operator, $U(t) = e^{-iHt}$, using the standard Suzki-Trotter decomposition introduced in Section 2.3. In particular, in the following we use the second order symmetric decomposition given by:

$$U(t) = e^{-iHt} = e^{-ia\frac{t}{2}}e^{-ibt}e^{-ict}e^{-ia\frac{t}{2}} + O(t^3), \tag{4.1}$$

with $a = -Jh_x \sum_{i=1}^{L} \sigma_i^x$, $b = -Jh_z \sum_{i=1}^{L} \sigma_i^z$ and $c = -J \sum_i^L \sigma_i^z \sigma_{i+1}^z$. Note that e^{-ibt} is not symmetrised in this expression as $[b, c] = 0$. A schematic of the gate sequence required to implement this is given in Fig. 4.1. Given a small t and multiple consecutive implementations of this quantum circuit we would be able to reach simulations up to arbitrary times, if it were not for gate errors. However, each Trotter step induces large errors and thus we are restricted with the number of Trotter steps we can reasonably use. In the following results we found that by keeping the number of Trotter steps fixed and varying t, i.e. keeping the exact gate sequence fixed but varying the circuit parameters, we were able to keep the error rate approximately constant. This constant error rate was valuable with regards to performing error mitigation. We introduce the protocols utilised in this work that reduced the effect of error in the following section.

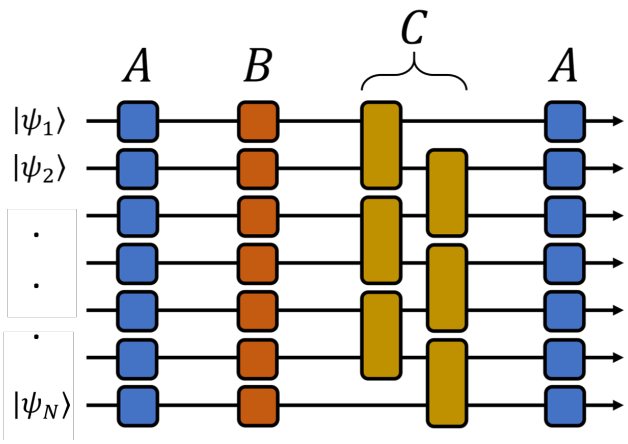

Figure 4.1: The gate sequence in each Trotter step performed on the quantum computer. Here, $A = e^{\frac{itJh_x}{2}\sum_{i=1}^{L}\sigma_i^x}$, $B = e^{itJh_z\sum_{i=1}^{L}\sigma_i^z}$ and $C = e^{itJ\sum_i^L \sigma_i^z\sigma_{i+1}^z}$.

4.2 Error Mitigation

Throughout the results presented in this chapter, we employed both the qubit selection protocol introduced in Section 2.6.1, and the measurement error mitigation introduced in Section 2.6.2. Beyond this, we consider two other mitigation methods that are specifically tailored the TFIM model with a longitudinal field.

Firstly, the initial states considered here have an inherent inversion symmetry around the centre site such that the data should reflect this symmetry. However, because of inhomogeneous errors in the IBM device, this symmetry is lost. We found that by enforcing this symmetry - averaging the data with its mirror image - that qualitative structure of the physics can be recovered. Secondly, we projected the data into the two domain-wall subspace. For our initial states and quench setups, the error-free time evolution mainly takes place within this subspace, and crucially, it contains the desired confinement physics. Hence, this post selection to the two domain-wall subspace is a viable tool for eliminating errors. To quantify the extent to which the two domain-wall subspace dictates the motion of domain-walls, one can look at $\phi(t)$ defined as

$$\phi(t) = \sum_i |\langle i|\psi(t)\rangle|^2, \tag{4.2}$$

where, $|\psi(t)\rangle$ is the full many-body wave function of the spin chain at the time t after the global quantum quench and $\{|i\rangle\}$ are the basis states of the two domain-wall subspace. $\phi(t)$ can be seen

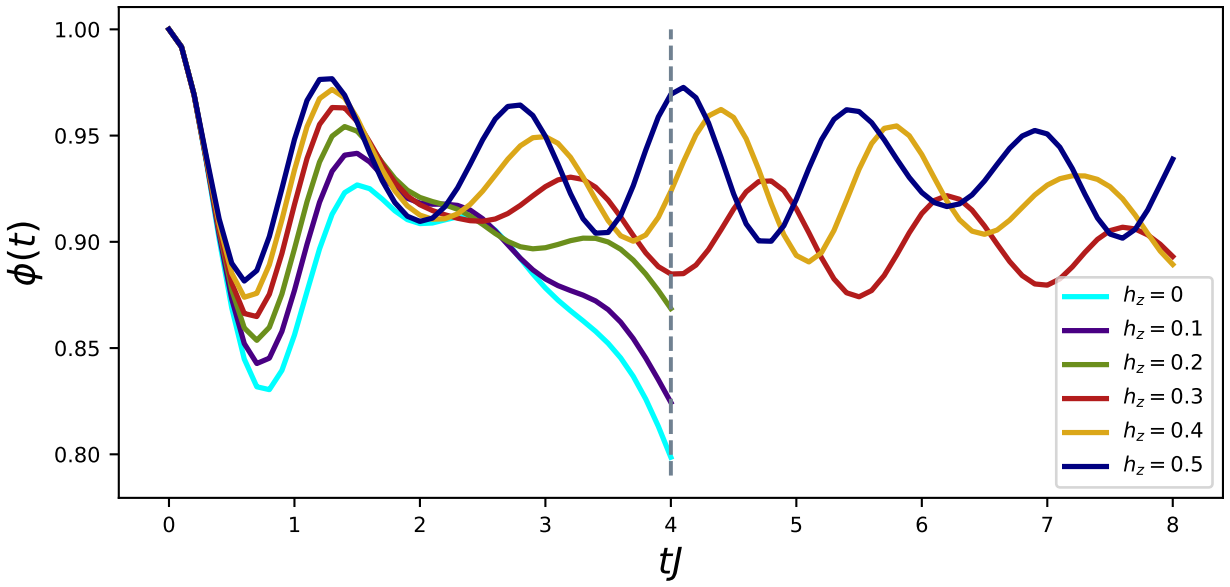

Figure 4.2: A measure of the contribution of the two domain-wall subspace, $\phi(t)$, after a global quantum quench to the TFIM with a longitudinal field on the state $\left|\frac{L-1}{2}, 1\right\rangle$. Here $h_x = 0.5$ and $L = 9$.

as the percentage of the full wave function, $|\psi(t)\rangle$, that remains in the two domain-wall subspace. In Fig. 4.2 it is clear that the two domain-wall subspace is responsible for the majority of the dynamics of the full Hilbert space. Hence, by post selecting states measured in the two domain-wall subspace the correct states will be selected up to reasonable error.

A simple intuition behind the effectiveness of this mitigation technique is as follows. Let δ be the probability of bit flip error for a qubit. For a two domain-wall state there are just four possible erroneous spin flips that do not result in the measurement to be outside the subspace. Therefore to first order approximation the error that will not be mitigated is just 4δ, which does not scale with system size. In turn, the probability of error in simulations that can be mitigated via a projection into the two domain-wall subspace is $(N-4)\delta$. At second order, the probability of two consecutive errors occurring that take the result out of and then back into the subspace is of order δ^2. With a small δ this second order process is much less likely. For an example of the effectiveness of the error mitigation methods outlined in this section see Appendix B.1. Given these protocols, in the following chapter we present results from the IBM digital quantum computers that show qualitative and quantitative signatures of confinement dynamics.

4.3 Results

4.3.1 Meson Velocities

To obtain results of the meson velocities we employed a global quench protocol to the TFIM with and without a longitudinal field. The initial state considered was a product state with a single spin flipped at the centre, i.e. the state $\left|\frac{L-1}{2}, 1\right\rangle$. The observable measured Δ_i^{zz} given in Eq. 3.21. In Fig. 4.3 we show results (with $h_z = 0, 0.5$ and $h_x = 0.5$) from the IBM machine, obtained via Trotterised time evolution, compared with both continuous time exact diagonalization (ED) and Trotterised ED, both projected to the two domain-wall subspace. The short time dynamics is governed by the free motion of domain-walls (dashed) before the boundstates form and propagate at the slower meson velocity (solid). From these results, initial velocities and subsequent slower velocities were extracted. In Fig. 4.4 we compare the obtained velocities with the theoretical values for both the free and meson cases. Here, we see that the extracted velocities are in quantitative agreement with the ideal values.

In order to extract the initial free domain-wall and later meson velocities from the mitigated data obtained by the IBM device, the gradient of the light cone formed in Δ_i^{zz} data is computed. Due to the inherent error in the NISQ device, there is a level of uncertainty in the saturation levels that should be used. Thus, a range of velocities are computed and the averages and standard deviations are obtained.

To obtain the initial velocities quench dynamics up to $tJ = 4$ are considered, the time before boundary effects are noticeable. Here, four Trotter steps were used. In these results there are initialisation errors that would cover up the free domain-wall velocity unless they are removed. Fig. 4.5 shows Δ_i^{zz} data collected for sites $i \in \{0, 1, 2\}$ after forcing the minimum of each to be zero, removing the effect of the initialisation error. To calculate a velocity one can choose a saturation level, S, and find the times at which Δ_i^{zz} surpasses this number for each site $i \in \{0, 1, 2\}$. This gives three (x, t) coordinates for which the gradient of a line of best fit gives the velocity. When computing the light cone gradients for initial velocities the same range of saturation levels were used for each value of h_z for consistency.

It turns out that the meson velocities are much more simple to obtain because the meson velocities

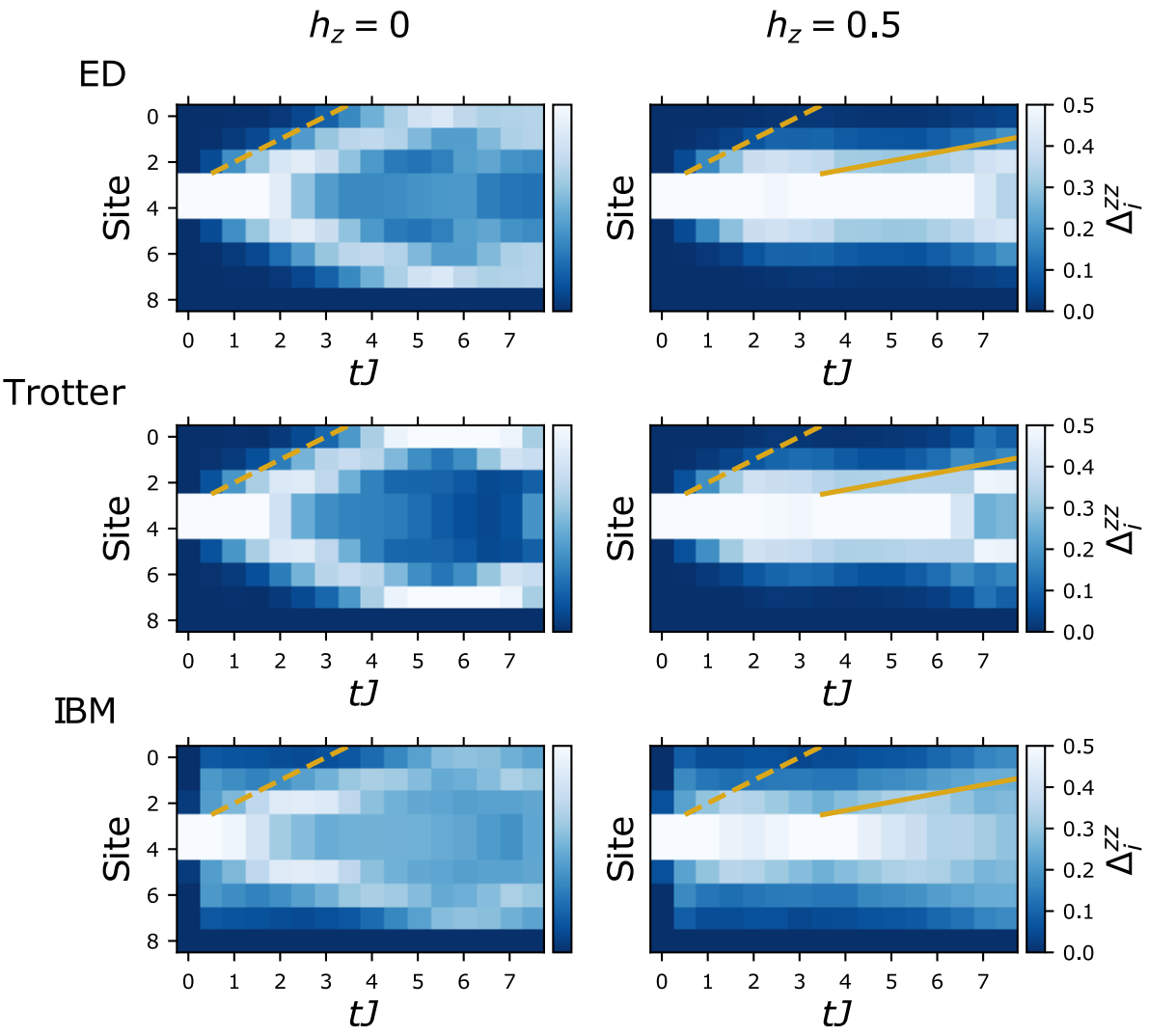

Figure 4.3: Data for Δ_i^{zz} after a global quantum quench to the TFIM with and without a longitudinal field starting from the state $\left|\frac{L-1}{2}, 1\right\rangle$. In all presented data $h_x = 0.5$ and $L = 9$. The graphs on the left show the free domain-wall case, $h_z = 0$ and the graphs on the right the confined one $h_z = 0.5$. Clear suppression of the domain-wall separation can be seen in the latter as well as the emergence of a second slower velocity – both signatures of confinement.

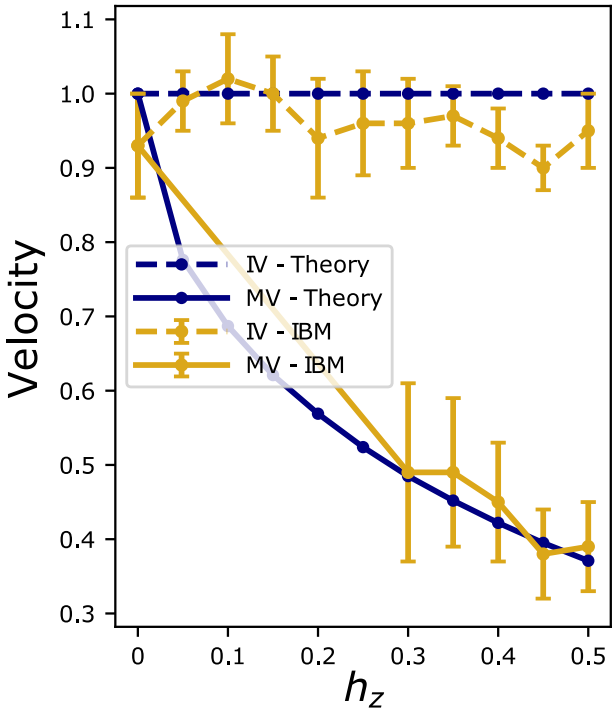

Figure 4.4: Comparisons of the two velocities, the initial velocity (IV) and meson velocity (MV), as measured on the IBM quantum computer ($h_x = 0.5$ and $L = 9$) after error mitigation and as theoretically predicted. Error bars displayed are the standard deviation of a range of velocities obtained.

themselves are observed at the scale $O(10^{-1})$. Data was collected up to $tJ = 8$, a time such that boundary effects are not present, using seven Trotter steps. An initial time of $tJ = 4$, roughly the time at which mesons form, was used as the starting point of the light cone to measure the meson velocities. The light cones produced for a given saturation level, $S = 0.21$, and the corresponding velocities are shown in Fig. 4.6. Again, the same range of saturation levels was used for each value of h_z to obtain an average velocity.

4.3.2 Suppression of Entropy Spread

The second order Rényi entanglement entropy results are presented in Fig. 4.7. Here, we compare the exact results calculated via ED and Trotterisation with the data from the IBM device. Note, due to the randomised measurement protocol required to obtain data for the entanglement entropy, the error mitigation protocols of symmetrisation and projected into the two domain-wall subspace could not be implemented. Hence, errors can still be seen in the results. Nevertheless, the IBM device reproduces the suppression of entanglement spreading that depends on the strength of the confining

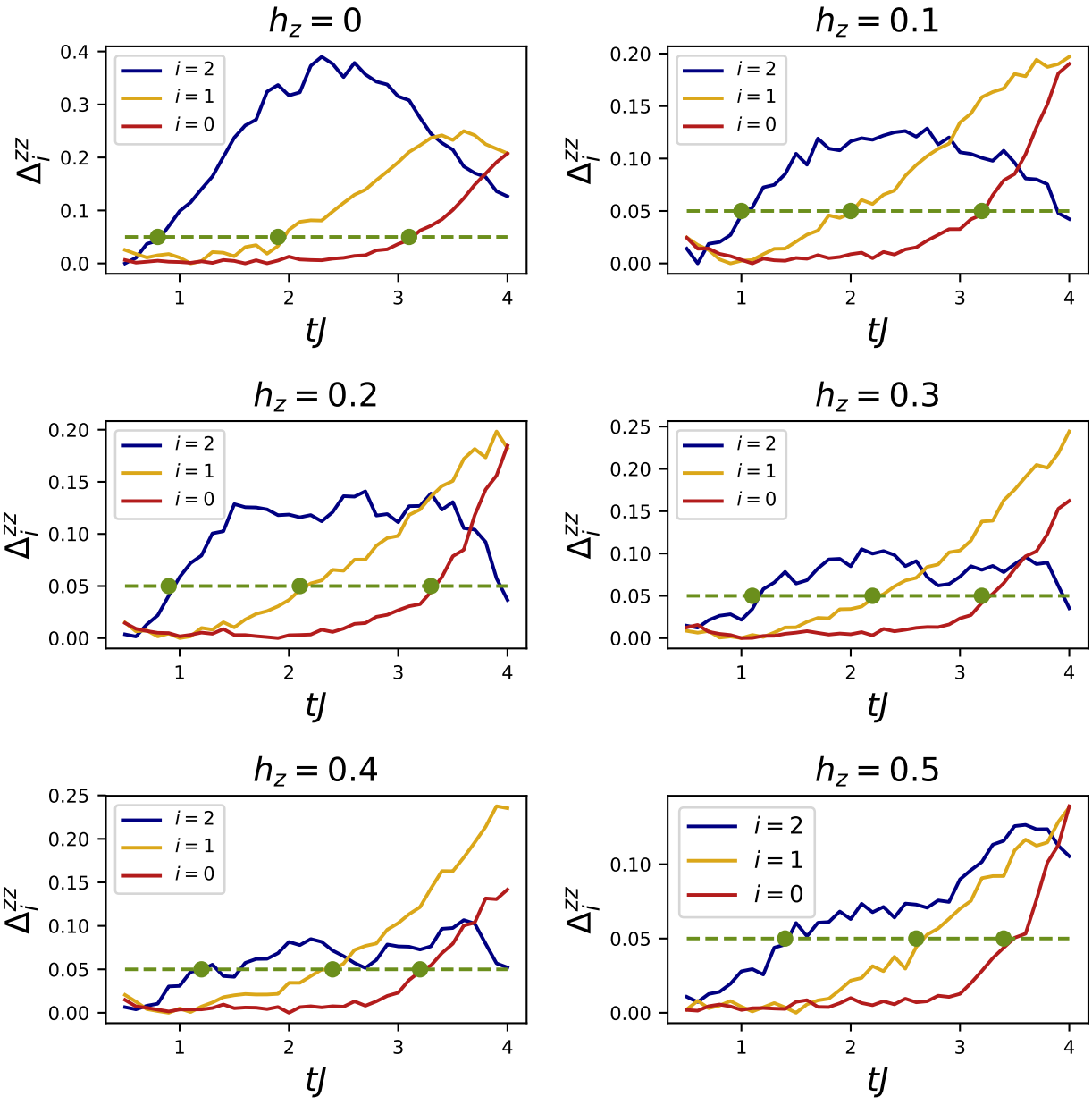

Figure 4.5: Re-scaled data for Δ_i^{zz} after a global quantum quench to the TFIM with a longitudinal field on the state $\left|\frac{L-1}{2}, 1\right\rangle$. In all presented data $h_x = 0.5$ and $L = 9$. Green points correspond to the (x, t) coordinates used to calculate the initial velocities for a saturation level of $S = 0.05$. Each figure shows clearly the free domain-wall movement from sites 2 to 0. The velocities measured depend heavily on the saturation levels used hence the use of a large range to get an average.

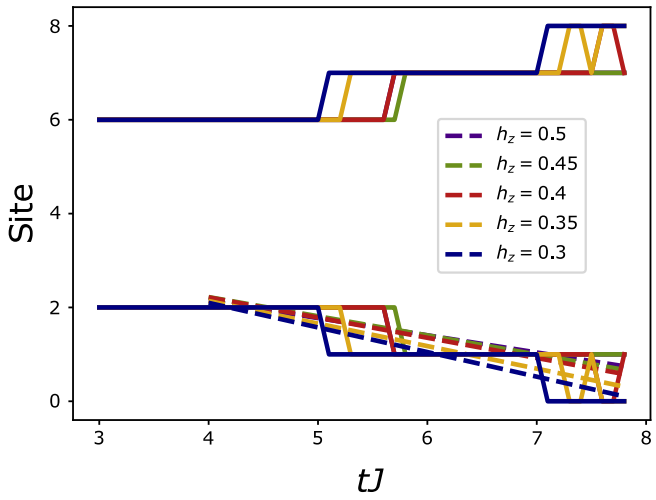

Figure 4.6: Light cones produced by saturating Δ_i^{zz} data. Data saturated at $S = 0.21$ for Δ_i^{zz} after a global quantum quench to the TFIM with a longitudinal field on the state $\left|\frac{L-1}{2}, 1\right\rangle$. In all presented data $h_x = 0.5$, and $L = 9$. Clear light cones are formed with varying velocities that depend on the strength of the longitudinal field.

longitudinal field. However, while the qualitative structure of Rényi entanglement entropy obtained on the IBM machine is correct, in order to obtain quantitative agreement with ED results a constant shift is needed.

To further probe this shift error we considered circuits with a varying number of Trotter steps that only evolve the state to very short times, $tJ = 0.01$, preparing a quantum state that will have an expected Rényi entropy of zero to the degree of accuracy which is obtainable by the IBM device. This protocol increases gate errors as a function of the number of Trotter steps, N_T. From the inset of Fig. 4.7 it can be seen that the error in performing gates on the IBM device has the effect of a constant entropy shift observed for all times measured on the device that grows with the number of Trotter steps used linearly. In Chapter 5, we diagnose this error and suggest a mitigation scheme that allows for the IBM devices to give quantitative results for entanglement entropy.

4.3.3 Probability Maps

The last result presented in this chapter is a simple viable diagnostic of confinement - the probability maps of domain-wall positions [122]. After time evolution the probabilities of the first domain-wall position with respect to the position of the second domain-wall is mapped to show that, in the presence of an additional longitudinal field, it is favourable for the two domain-walls to reside close to each

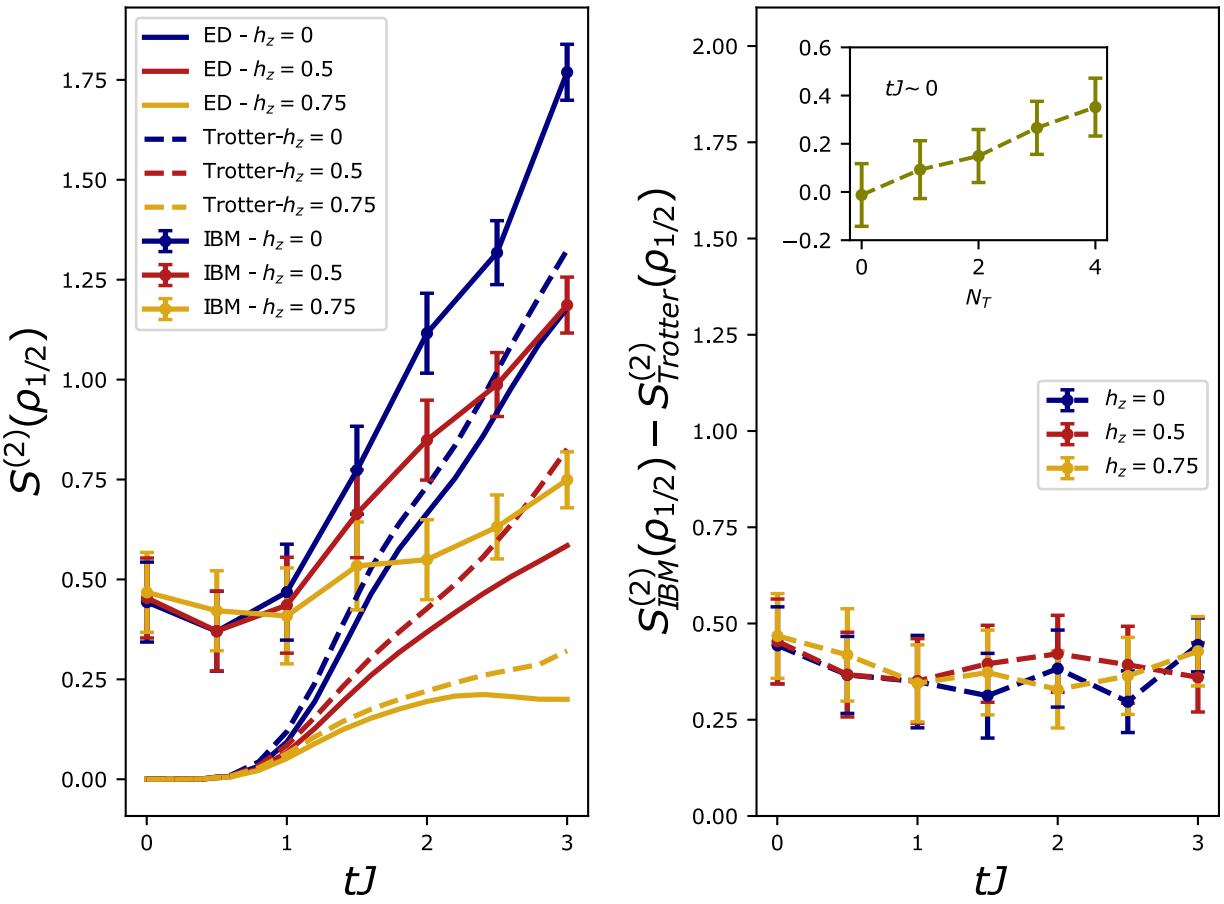

Figure 4.7: Time evolution of the half chain Rényi entropy measured on the IBM device. The left panel shows the data for the half chain second order Rényi entropy as a function of time after a quench to the initial state $|3, 2\rangle$. The right panel shows explicitly this constant shift due to gate error with the inset plot showing how this shift depends on the number of Trotter steps, N_T. This shift is time independent and grows with N_T

other, i.e. the domain-walls form a meson.

Fig. 4.8(a) displays the probability maps of domain-wall motion collected from the quantum computer after a global quench protocol to the TFIM with and without a longitudinal field. The initial state is a polarised state with a single spin flipped at the centre. In the free fermion picture, these domain-walls can freely propagate around the system and after some time will have an approximately uniform distribution; this is reflected in the $h_z = 0$ results. However, in the confining case, these domain-walls form a meson and should reside close to one another for long times, this can be seen in the $h_z = 0.5$ results by the large probability of measuring the domain-walls $1 - 2$ sites away from each other - the diagonal of the probability map.

Note, in order to corroborate our findings, it is crucial to confirm that the halting of domain-wall spreading for increasing h_z arises from coherent quantum dynamics and not just disorder or noise from the machine which have plagued previous attempts [92]. In Fig. 4.8(b) we show the evolution of the local magnetisation for a quench with $h_x = h_z = 0.5$ and $L = 7$. Clear oscillatory patterns of the confined domain-wall motion are observed in Fig. 4.8(c) which provide direct evidence of higher order interaction effects and not a simple featureless decay of correlations.

Despite the effectiveness of the error mitigation methods used in this work, to fully account for the constant shift seen in the Rényi entropy measurements as well as extract out more subtle signatures such as the meson masses, stronger mitigation is needed. Thus, in the following chapter a hardware agnostic, simply implementable and effective error mitigation protocol is presented.

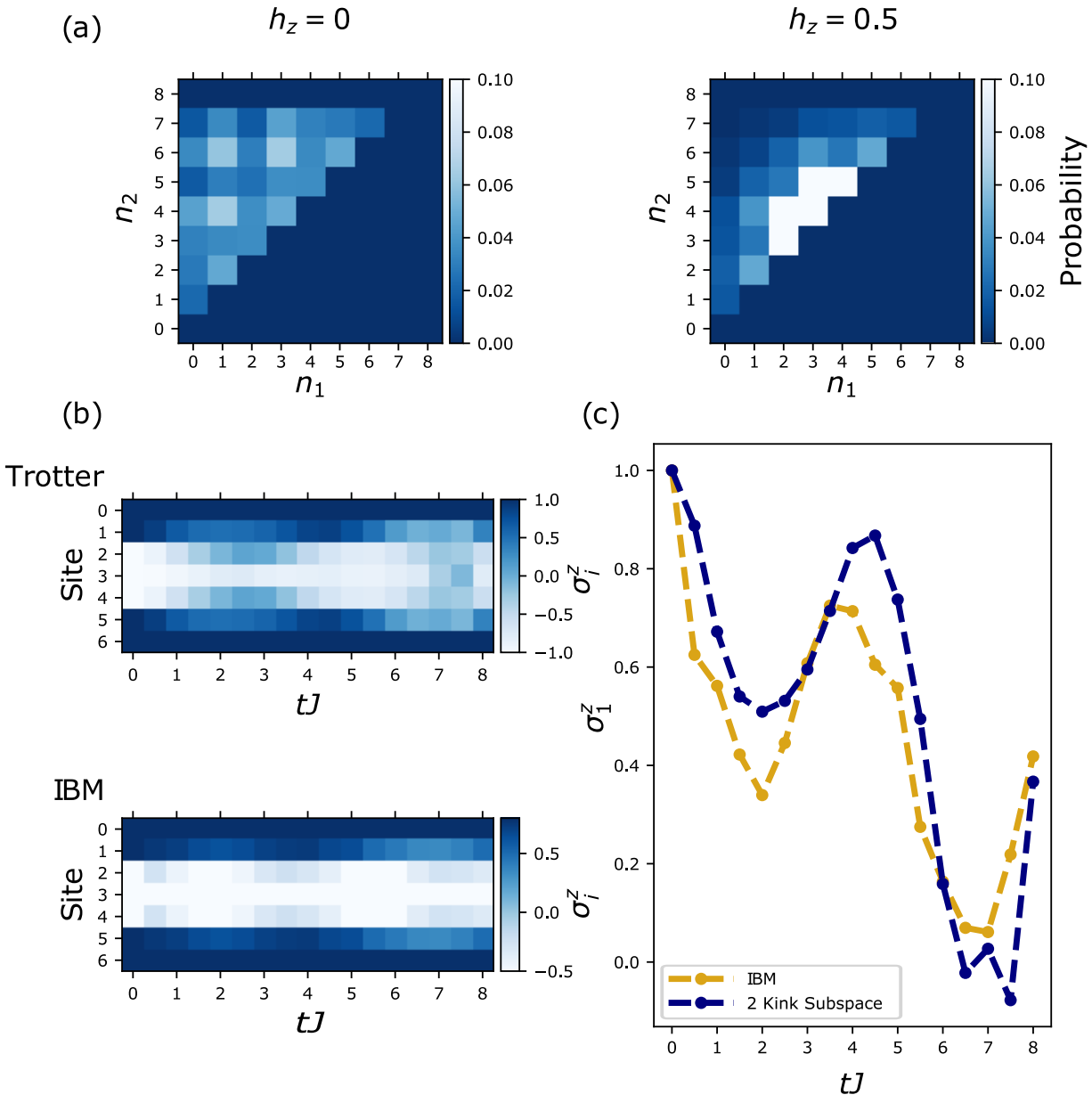

Figure 4.8: Data from the IBM device of the probability maps of domain-wall position after a global quantum quench with and without a longitudinal field (for $h_x = 0.5$ and $L = 9$) on the state $\left|\frac{L-1}{2}, 1\right\rangle$. The graph on the left shows the free domain-wall case, $h_z = 0$ and in the graph on the right $h_z = 0.5$. Clearly if $h_z = 0$, the domain-walls have no preference to remain close together as there is no confining field. However, for $h_z = 0.5$, the domain-walls have a much larger probability to reside close to one another than being separated. (b) The local magnetisation after a global quantum quench with $h_x = h_z = 0.5$ and $L = 7$ on the state $\left|\frac{L-1}{2} - 1, 3\right\rangle$. These results show clear oscillatory motion of domain-walls. This is a high order effect that is only seen with interactions and not just disorder. (c) The local magnetisation of the first qubit before symmetrisation, σ_1^z, is shown explicitly, highlighting the oscillatory behaviour captured by the quantum computer.

Chapter 5

Simple Mitigation of Global Depolarising Errors in Quantum Simulations

It is known that NISQ simulators are plagued with large initialisation, measurement and gate errors but a full description of their effect is beyond current knowledge. In general, errors using a NISQ device to perform quantum simulation will have both incoherent and coherent effects. This lack of understanding results in error mitigation methods either relying on strict knowledge of the device in use or the simulation being performed, and thus are not generally applicable, or attempting to learn the effects of errors currently being faced, leading to large overheads and computational costs. In this section, we present a mitigation protocol that does not attempt to fully understand the inherent errors on a quantum device but assumes that given the current circuit is deep enough, we can mitigate the average effect. The underlying approximation of this error mitigation protocol is outlined in the following section.

This chapter closely follows the work published in Ref. [3] in which Joseph Vovrosh was the main contributor with the other authors having significant input. In particular, all authors were involved in the preliminary discussions, with the conceptual ideas led by Joseph Vovrosh and Kiran E. Khosla. The classical simulations were performed by Kiran E. Khosla following discussions with Joseph Vovrosh. The experiments performed directly on the IBM digital quantum computers were jointly performed by Joseph Vovrosh and Sean Greenaway.

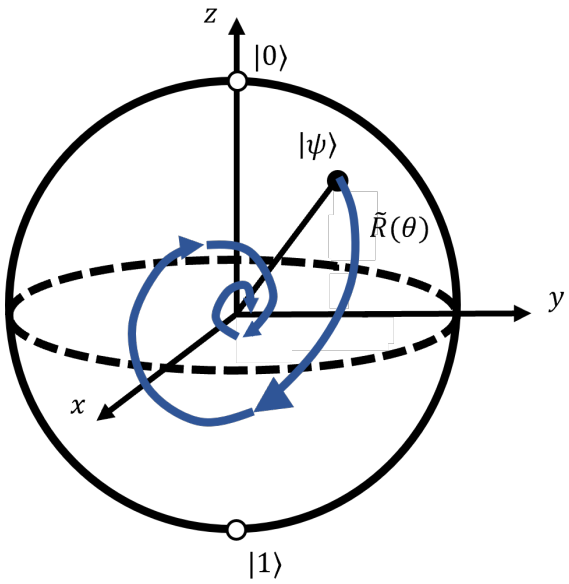

Figure 5.1: A schematic showing how the repetition of an entangling gate on a single qubit, $\tilde{R}(\theta)$, can lead to the maximally mixed state, i.e. a depolarising error.

5.1 A Global Depolarising Error Model

This error mitigation protocol is based on the assumption that the gate errors that plague a deep quantum circuit are well described by a *global depolarising* error model. For a rigorous derivation of the ansatz used in this paper we turn to work done by Zhenyu Cai [102]. In this, the author starts with the assumption that the noise of a quantum device can be well described by a general Pauli noise model. From this, they derive the resulting density matrix, which they present as a series expansion. The global depolarising ansatz used in our work is a special case of the leading order term in this expansion. However, here we give a heuristic argument to justify this approximation from the starting point of depolarising gate errors.

Depolarising errors are inevitably present in any digital quantum simulator platform and can be treated without much specific knowledge about the device performance (which also fluctuates over time [92]). An n-single qubit depolarising error channel can be modelled via

$$\mathcal{E}^{\otimes n}(\rho) = (1-p)^n \rho + \sum_{\alpha \in [x,y,z]} \sum_{j=1}^{n} (1-p)^{n-1} \frac{p}{3} \sigma_\alpha^j \rho \sigma_\alpha^j + \dots , \tag{5.1}$$

where $\mathcal{E}$ is the error channel, p is the probability of an error occurring for each qubit (assumed to be

equal for each qubit, and for each Pauli error) and '...' indicates higher-order terms corresponding to errors on multiple qubits [27]. One important feature of this mathematical formulation is that the second term, which describes the depolarising error, commutes with any unitary operator. Consequently, the error on the i^{th} qubit in a quantum circuit with purely depolarising errors is

$$\mathcal{E}^i(\rho) = (1 - p_i)\rho + p\,\mathrm{Tr}_i[\rho] \otimes \frac{\mathcal{I}_i}{2}, \tag{5.2}$$

in which ρ is the density matrix, $\mathcal{I}_i/2$ is the maximally mixed (i.e. completely depolarised) state for the i^{th} qubit, Tr_i is the partial trace over the i^{th} qubit and p_i is the error on the i^{th} qubit.

Instead of dealing with all combinations of single qubit errors, we approximate the total error channel of Eq. (5.1), under the assumption of symmetric depolarisation, Eq. (5.2), as an effective depolarising channel on the *entire* quantum state

$$\rho = (1 - p_{\mathrm{tot}})\rho_{\mathrm{exact}} + p_{\mathrm{tot}}\frac{\mathcal{I}^{\otimes n}}{2^n} \tag{5.3}$$

where the effective *total* error probability is p_{tot}. In principle p_{tot} is well approximated by $\prod_i(1-p_i)$, however, we do not make that identification here - we will soon show that p_{tot} can be measured directly on the device. The many partial traces over single qubits, which would have conserved some coherence in the remaining qubits, have been replaced by the maximally mixed state $\mathcal{I}^{\otimes n}/2^n$ over the global quantum state, destroying all coherence. We stress that even though this may not be a good approximation for a single layer of qubit errors, it becomes a reasonable approximation for the error channel of a many layer, many qubit circuit. Eq. (5.3) is our basic ansatz for an effective error model after a many-layered unitary circuit and ρ_{exact} is the exact density operator without noise.

The simplicity of this ansatz allows it to be easily calculated. It has already been shown to be useful when mitigating measurement error [123], however we later demonstrate that it is a powerful tool for mitigating global depolarising errors which do not themselves originate from local depolarising errors. Furthermore, we later numerically demonstrate that this ansatz does not rely on the assumption of single- and two-qubit depolarising errors. Moreover, our focus on depolarising errors has the advantage of being treatable mathematically in a controlled way as detailed below. Last but not least,

the large improvement in the quality of results on the IBM device motivate our choice of depolarising errors a posteriori. The full error mitigation protocol based on this ansatz is presented in the next section.

5.2 Mitigation Protocol

With this ansatz one can analytically calculate the effect of errors on a measured observable, $\hat{O}$, via

$$\langle \hat{O} \rangle = (1 - p_{\rm tot}) \, {\rm Tr}\Big[\hat{O}\rho_{\rm exact}\Big] + \frac{p_{\rm tot}}{2^n} \, {\rm Tr}\left[\hat{O}\right]. \tag{5.4}$$

Our approach estimates p_{tot} in order to apply error mitigation. We propose and test two approaches for finding p_{tot}; the first based on estimating the purity of the final state and the second based on studying specific observables. To estimate the purity, we employ the recent protocol for obtaining the trace of the reduced density matrix squared, ${\rm Tr}[\rho_A^2]$, via randomised measurements [124, 125], where A is a subspace of the full density matrix. This randomised measurement scheme has been successfully implemented in trapped ion quantum simulators [53] and recently by some of us on the IBM quantum computer [1]. We stress the present mitigation is a far simpler task compared to inverting the quantum error channel to tomographically reconstruct the error free quantum state ρ.

As current quantum devices initialise systems in pure states that are then manipulated with unitary transformations, ${\rm Tr}[\rho^2]$ over the full Hilbert space should lead to a result that is identically one. However, since the noisy implementation of quantum circuits will in general deviate from unitarity, after a given quantum circuit is run on a quantum processor this will generally not be the case. Instead, with Eq.(5.3) we expect that

$${\rm Tr}\left[\rho^2\right] = (1 - p_{\rm tot})^2 + \frac{p_{\rm tot}(1 - p_{\rm tot})}{2^{n-1}} + \frac{p_{tot}^2}{2^n} \tag{5.5}$$

using the fact that $\rho_{\rm exact}$ is pure. Now, given that the left hand side, ${\rm Tr}[\rho^2]$, can be measured directly on the device [1, 53], this quadratic equation can be solved to obtain the total error $p_{\rm tot}$ [123, 126]. We stress that unitary errors in quantum circuits do not increase entropy and thus $p_{\rm tot}$ obtained via this

method should really be understood as the *global depolarising* error probability. While this mitigation approach does not address coherent errors, it could additionally be combined with other techniques such as twirling [127, 128, 129, 130].

Therefore, with p_{tot} extracted and $\langle\hat{O}\rangle$ measured the only unknown quantity in Eq. 5.4 is the desired error-free observable $\text{Tr}\left[\hat{O}\rho_{\text{exact}}\right]$. Note, we assume that $\text{Tr}\left[\hat{O}\right]$ can be calculated, which for most practical cases should be the case, e.g. see our application examples in the following sections.

Putting all steps together, we finally obtain our general error mitigation protocol:

1. Prepare the quantum state of interest by running a quantum circuit and measure $\text{Tr}[\rho^2]$, e.g. via randomized measurements [125, 53, 1];
2. Use the results to obtain values for p_{tot} via Eq. 5.5;
3. Prepare the quantum state again and measure the desired observable $\langle\hat{O}\rangle$; [1]
4. Use Eq. 5.4 with the measured value of p_{tot} to obtain the desired $\text{Tr}\left[\hat{O}\rho_{\text{exact}}\right]$.

Statistical Errors Introduced by the Error Mitigation

As with any error mitigation protocol, the uncertainty of the simulation result grows through this process. The statistical uncertainty of p_{tot} can be derived assuming an error in the measurement of the purity from a NISQ device, $\delta\,\text{Tr}(\rho^2)$, as

$$\delta p_{tot} = \pm(1-p_{tot})\frac{\delta\,\text{Tr}(\rho^2)}{2(2^n-\text{Tr}(\rho^2))}. \tag{5.6}$$

Note that $\delta\,\text{Tr}(\rho^2)$ can be estimated by resampling e.g. Jackknife or Bootstrap [53, 1]. As a result, when using the proposed error mitigation on a measurement of an observable $\hat{O}$, the additional uncertainty on top of the measurement errors is given by

$$\delta\langle\hat{O}\rangle = \pm\left(\frac{\delta_{meas}\langle\hat{O}\rangle}{1-p_{tot}} + \frac{\delta p_{tot}\left(\langle\hat{O}\rangle - 2^{-n}\,\text{Tr}\left(\hat{O}\right)\right)}{(1-p_{tot})^2}\right), \tag{5.7}$$

[1] As errors on the quantum devices can vary over time (see Ref. [92]), the determination of p_{tot} has to be recalibrated accordingly.

where $\delta\langle\hat{O}\rangle$ is the error in the mitigated value of $\langle\hat{O}\rangle$ and $\delta_{meas}\langle\hat{O}\rangle$ is the error in the measurement of $\langle\hat{O}\rangle$. As alluded to earlier, it turns out that given the global depolarizing error ansatz, other, more simple error mitigation protocols can be proposed. In the following we introduce one such method that we saw some success with.

5.2.1 Simplified Method

An alternative approach to estimating p_{tot} is to consider specific observables whose expectation values are known. For example, consider the time dynamics of a system in which our quantum circuit approximates the time evolution operator $U(t) = \exp\{-iHt\}$ where we wish to measure $\langle O(t)\rangle$ for a range of times. We can tune the circuit such that $t * (E_{max}) = \epsilon << 1$, where E_{max} is the largest eigenvalue of the Hamiltonian (shifted so $E_{min} = 0$), so that our quantum circuit now approximates the identity operation. Assuming that $\langle O(t = 0)\rangle$ is known, we can use the measurements from the quantum device and Eq. 5.4 to obtain p_{tot}. In the following we are mainly interested in the time dependence of the local magnetization, which further simplifies with $\mathrm{Tr}[\sigma^\alpha] = 0$ in Eq. 5.4 to

$$\langle\sigma_i^\alpha\rangle = (1 - p_{\mathrm{tot}})\langle\sigma_i^\alpha\rangle_{\mathrm{exact}}. \tag{5.8}$$

Given that $\langle\sigma_i^\alpha\rangle$ is measured and $\langle\sigma_i^\alpha\rangle_{\mathrm{exact}}$ is known, p_{tot} can be calculated. Note, for infinite dimensional Hamiltonian with unbounded eigenvalues, the approximation is slightly more subtle, but does not apply to qubits. We show that while this method is more efficient, it does not discriminate between unitary and entangling errors and thus sometimes fails. In the following we compare the effectiveness of both the full mitigation protocol and this simplified method using classical simulations.

5.3 Simulated Results

Our protocol can be applied to essentially any quantum circuit and quantum simulation device. In order to obtain a large amount of data to support our mitigation technique, we numerically simulate the layered circuits with noisy gates. Qiskit's circuit simulator allows one to simulate arbitrary gate-based

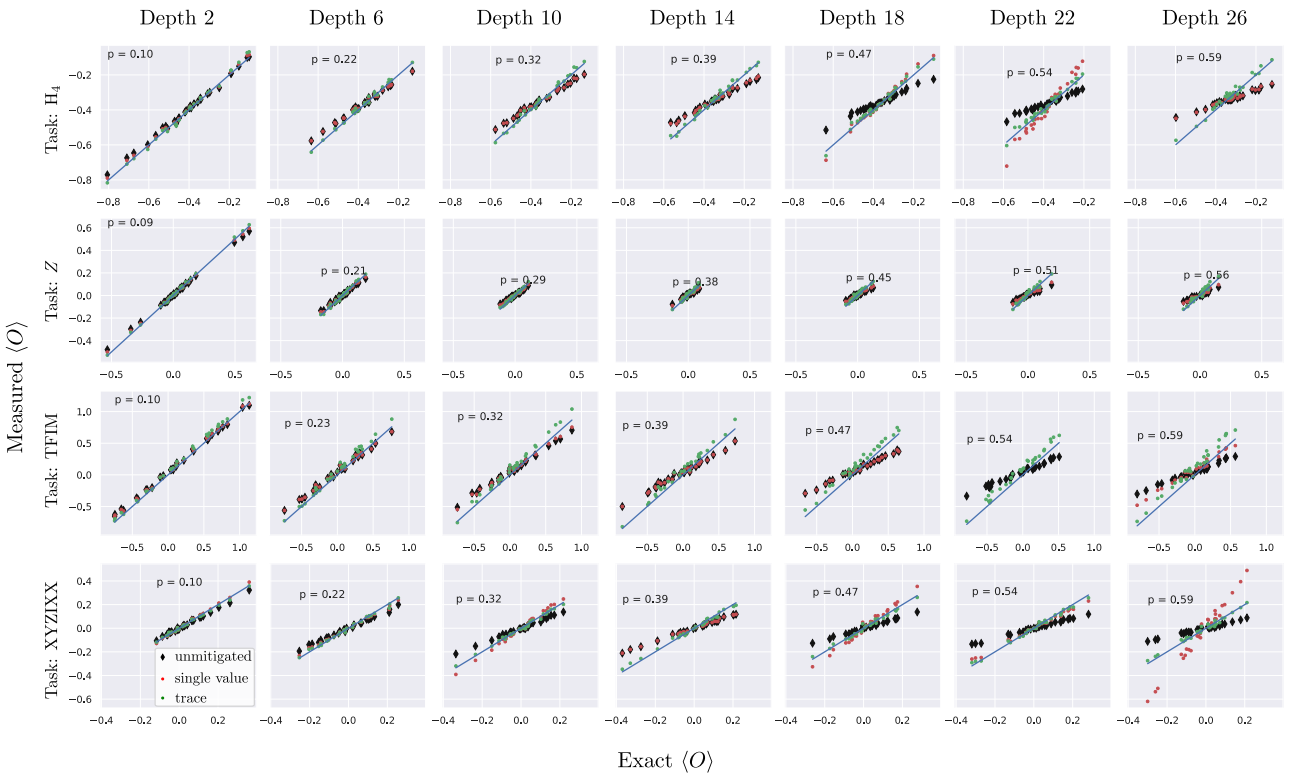

Figure 5.2: Scaling of our mitigation schemes (circles) with circuit depth for four different operator expectation values. Single operator (red circles) show some improvement, while trace mitigated (green circles) show a robust improvement over the unmitigated results. These numerical simulation uses the *ibmq_santiago* error model, and circuits are layers *u3* and CNOT, with the depth equal to the number of entangling layers. Note there are some combinations (e.g. TFIM at depth 14 etc) where the single expectation value mitigation found $p_{tot} = 1$, and therefore did not improve results. Likewise there are other combinations (e.g. TFIM depth 22) where the single expectation value mitigation is omitted because it gave an unphysical estimate of $p_{tot} < 0$. Inset numbers show p_{tot} as estimated for the trace estimation.

noise models by specifying independent Kraus operators for each single- and two-qubit gate [27]. Using this noisy simulator, we can directly test how gate-level non-depolarising errors can result in an effective global circuit-level depolarising error, and how well our mitigation technique works in the presence of local non-depolarising errors. To simulate a realistic noise model, we take the Kraus operators directly from the *ibmq_santiago* backend [131] (as of 12^{th} March 2021). This error model goes beyond the single gate depolarising assumption, by including (asymmetric) thermal relaxation.

In order to test local, non-local, single and many Pauli-string operators, we have chosen the following operators: a single Z operator (local, single term), the TFIM Hamiltonian (local, many terms), a random Pauli string (non-local, single term) and the molecular Hamiltonian of an H_4 (non-local, many terms). Here 'many terms' refers to the number of non-commuting Pauli strings that must

be measured to construct the expectation value, and 'locality' refers to only containing single and two-qubit Pauli strings. For this hydrogen Hamiltonian, openfermion [132] was used to compute the orbital integrals (for a row of four H-atoms with 0.1 nm inter-atomic distance), then map the problem to qubits using the symmetry conserving Bravyi-Kitaev transformation [133] and finally the $\mathbb{Z}_2$ symmetries (corresponding to particle spin) are removed, reducing the number of qubits by two. Note, the four hydrogen Hamiltonian is chosen as a simple molecular test case with a large Hilbert space, and where we can ignore complications from freezing out orbitals. For the TFIM, the Hamiltonian was reduced to two non-commuting Pauli strings from which the total Hamiltonian can be evaluated. Finally the single Z, and $XYZIXX$ (chosen randomly) operators were measured trivially. We do not directly account for State-Preparation and Measurement (SPAM) errors, but we note that we can (and do) include SPAM errors as contributing to p_{tot} in our channel ansatz.

We numerically simulate circuits consisting of layers of parameterized *u3* gates, generic single-qubit rotation gates with three Euler angles, followed by an entangling layer. The circuit depth is defined by the number of entangling (CNOT) layers. There is a final *u3* layer before measurement. The parameterized circuit now creates a state $\rho(\theta)$, and varying θ changes the state and corresponding operator expectation values. For the numerical simulations we consider how our mitigation performs for different depth circuits. For each depth the calibration p_{tot} must be done independently, as p_{tot} is an *effective* parameter for the whole quantum channel and cannot simply be calculated *a priori* for different depths.

5.3.1 Calibration

Two independent methods of calibrating p_{tot} are considered. Firstly, via a single expectation value: direct simulation of a circuit with fixed parameters, which is then compared to the error free expectation value to find p_{tot}. Secondly, via trace: from directly measuring $\mathrm{Tr}[\rho^2]$ and estimating p_{tot} via Eq. 5.5.

For single expectation calibration, a single fixed parameter circuit was used to find $\langle O \rangle$ (for each operator O considered). This result was compared to the error free simulation of the exact same circuit to estimate p_{tot}. To evaluate these expectation values 4096 shots were used for each non-

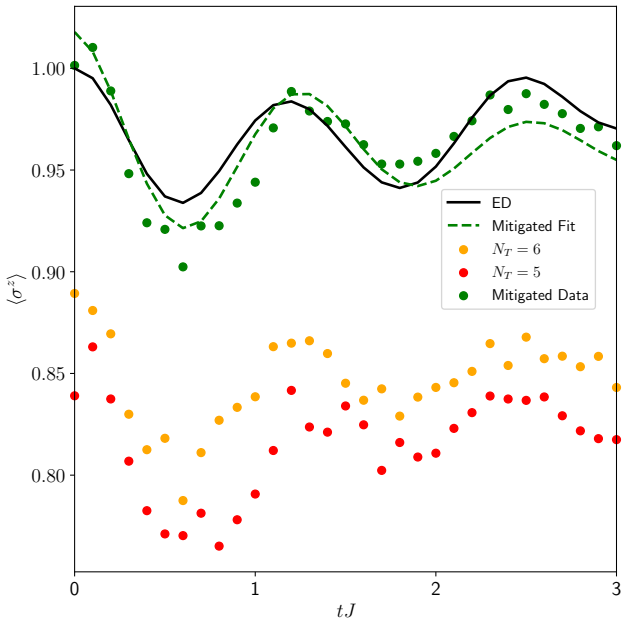

Figure 5.3: Quench dynamics of local magnetization from Trotterized time evolution of the TFIM with longitudinal field before and after error mitigation. Here, $J = 1$, $h_x = 0.5$, $h_x = 0.75$ and $n = 7$. Data is shown for, N_t, the number of trotter steps $N_t = 5, 6$. Results go from qualitative agreement to quantitative agreement. After fitting a cosine function (dashed green) to the mitigated data (green dots) the dominant frequency is clearly captured by the IBM device. Note, more details of the circuit composition of the evolution operator can be found in [1]

commuting term in the decomposition of the given operator into Pauli strings. For trace mitigation, an extra 500 circuits are used to estimate p_{tot} using 8196 shots per circuit. This was broken up into five lots of 100 circuits to estimate p_{tot} at five different (random) circuit parameterizations. For each parameterization, the method of Ref. [125] is used to find five independent estimates of p_{tot}, which are then averaged to reduce the bias in the estimate of p_{tot} for the circuit.

5.4 Results form the IBM Devices

5.4.1 Meson Masses

Recent work using a trapped ion quantum simulator to simulate the long-range TFIM model showed how, by choosing a variety of initial states, the meson masses can be measured through the persistent oscillations of local magnetization [120]. Previous attempts to perform a similar measurement on a digital quantum computer have failed for the short ranged TFIM because the results are too noisy

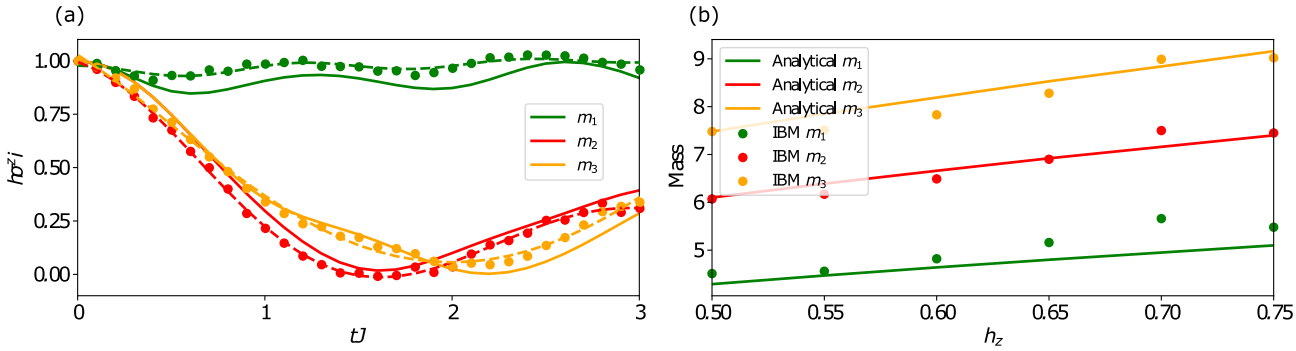

Figure 5.4: (a) The quench dynamics of the z-axis local magnetization is shown for different initial states. Here, $J = 1$, $h_x = 0.75$, $h_x = 0.75$ and $n = 7$. Results calculated via exact diagonalizionc are compared with the mitigated results from the IBM device *Toronto* [134]. Here, clear dominant oscillations are extracted that quantitatively agree with the analytically derived values. (b) A comparison of the masses obtained from the IBM device and the analytically derived values for varying h_z showing this quantitative agreement. Note, more details of the circuit composition of the evolution operator can be found in [1]

to resolve the smaller amplitude of oscillations [1]. Here, we show that our new error mitigation enables us to obtain the meson masses from the IBM device. As normal, the time dependence can be calculated by applying a quantum circuit from a Trotterisation of the time evolution operator. Increasing the number of trotter steps, N_T, leads to a deeper circuit and the ensuing increase in errors results in a peculiar dampening of the magnetization dynamics which can be removed via our error mitigation. We are then in a position to suppress the noise to a level which enables us to extract different meson masses on the IBM device by a basic fit of the main oscillation frequency. In Fig. 5.4 we show the data for the first three masses obtainable by starting from different initial states, see insets. Note, we obtained a range of results with a different number of trotter steps. Under the assumption that $(1 - p_{\text{tot}})$ scales as $(1 - p_T)^{N_T}$, where p_T is the error in one trotter step, we can extrapolate the results back to the error-free case, see green data points in Fig. 5.3. Here, 7 spins are mapped onto 5 qubits resulting in a circuit with $5N_T + 5$ single qubit gates and $8N_T$ CNOT gates with $N_T = 5, 6$. Remarkably, we find quantitative agreement between the mitigated results and the theoretical predictions for the scaling of the meson masses with the transverse and longitudinal fields [1].

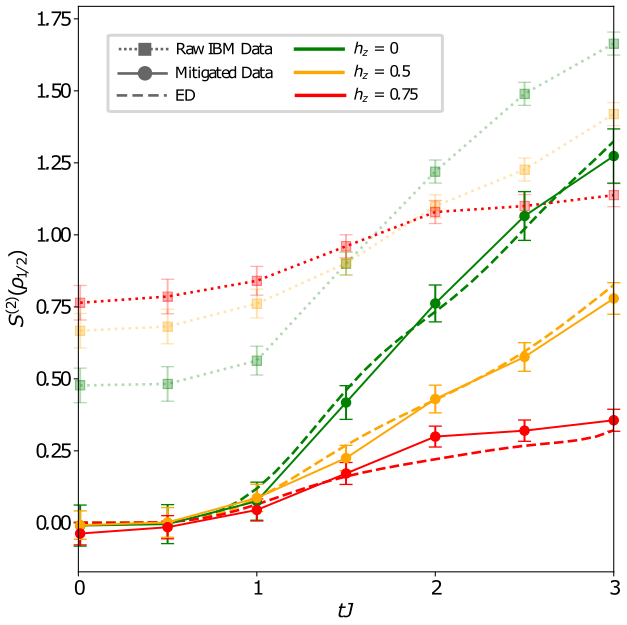

Figure 5.5: Results from the IBM device *Paris* [135] of the second order Rényi entanglement entropy. Quench dynamics before and after error mitigation of the second order Réyni entropy for the transverse field Ising model with varying longitudinal field strengths. Here, $J = 1$, $h_x = 0.5$ and $n = 6$. Note, 800 random unitaries were used to collect this data giving an uncertainty in the purity of $\delta\rho \sim O(10^{-2})$. Clearly the mitigation allows results to go from qualitative agreement to quantitative agreement with the results obtained numerically through ED.

5.4.2 Suppression of Entanglement Spread

As a second example of the effectiveness of this mitigation protocol we again study the suppression of half chain entanglement entropy spreading due to confinement. In Chapter 4 qualitative agreement for entanglement dynamics of six spins compared to an ED calculation was presented, but for a quantitative agreement a large shift of the results was needed. By using the ansatz in Eq. 5.3 we can see that the effect of global depolarizing errors on measurements of $\mathrm{Tr}[\rho_A^2]$, where A is a subsystem in consideration, is

$$\begin{aligned}\mathrm{Tr}\left[\rho_A^2\right] =&(1-p_{\mathrm{tot}})^2\,\mathrm{Tr}\left[\rho_{A,exact}^2\right]\\ &+\frac{p_{\mathrm{tot}}(1-p_{\mathrm{tot}})}{2^{n_A-1}}+\frac{p_{tot^2}}{2^{n_A}}.\end{aligned} \tag{5.9}$$

If p_{tot} is known, $\mathrm{Tr}\left[\rho_{A,exact}^2\right]$ can be extracted and the second order Rényi entropy measurement is calculated via

$$S^{(2)}(\rho_{\mathrm{exact}}) = -\log_2(\mathrm{Tr}\left[\rho_{A,exact}^2\right]). \tag{5.10}$$

Fig. 5.5 shows how this mitigation protocol eliminates the error in the second order Rényi entropy results. With our error mitigation protocol and Eq. 5.9 we now obtain quantitative agreement with ED results for six spins and can account for the large shift of the results.

With strong mitigation methods such as the one presented in this chapter, more ambitious simulation efforts can be performed. In the following chapters we consider two possible directions in which confinement effects can be used as a benchmark of NISQ devices in the future.

Chapter 6

Confinement Induced Impurity States in Spin Chains

Given the strict limitations when attempting to use a NISQ device for quantum simulation, we are restricted in the types of Hamiltonians that are feasible. Despite this, simple systems can result in deep physics that is yet to be unearthed. In this chapter we consider extensions to confinement in the short range TFIM with experimental feasibility in mind. This chapter closely follows the work published in Ref. [2] in which Joseph Vovrosh was the main contributor with the other authors having significant inputs. In particular, all authors were involved in the theoretical discussions led by Joseph Vovrosh and Alvise Bastianello. The analytical calculations were performed by Alvise Bastianello following discussions with Joseph Vovrosh. The semiclassical and two domain-wall simulations were performed by Joseph Vovrosh. Finally, the Time-Evolving Block Decimation simulations (TEBD) were preformed by Hongzheng Zhao.

Most of the studies of confinement in spin chains have focused essentially on single-meson physics and the interplay among mesons themselves, or with other constituents, is yet to be fully addressed. These are crucial questions from the perspective of simulating high-energy experiments which are based on scattering events. In a broader context, genuine many-body physics of confined excitations can be rightfully expected to be far richer – and challenging – than the already intriguing single-meson phenomena. Very recently, this program has been started in Refs. [136, 137, 138] with the

investigation of mesonic scattering in the TFIM with an additional longitudinal field. Due to the composite nature of mesons, the scattering of two wavepackets is deeply inelastic with the possibility of exciting mesonic internal degrees of freedom different from the injected ones. Nevertheless, only asymptotic states of two-quark mesons can be obtained and particles formed by a larger number of constituents, i.e. baryon analogues, do not exist in the spectrum of the theory (see however Refs. [139, 112]).

In condensed matter, scattering processes with the possibility of boundstate formation appear prominently in the context of impurities. On a practical side, any experimental setup unavoidably features defects whose effect must be understood. More interestingly in the quantum simulation realm, impurities in the form of localized potentials can themselves serve as *probes* of the quantum properties of the host. Famous examples are the distinct impurity response of singlet versus triplet superconductors (SCs) [140, 141], the characteristic impurity signal establishing the d-wave symmetry of high-temperature cuprate SCs [142], as well as the local response of fractionalized edge spins in Haldane spin chain compounds [143]. Alternatively, impurities as truly dynamical objects strongly couple to the background matter, giving rise to the venerable Kondo effect [144] or polaronic boundstates for mobile but heavy impurities [145, 146].

In this chapter, we study the interplay of confinement and impurity dynamics in a spin chain set-up. Similarly to the direct meson-meson interaction, scattering of a meson with an impurity is deeply inelastic. Apart from the main transmission (I) and reflection (III) processes of a scattering event, see Fig. 6.1, we show that in our system a nontrivial capture (II) may appear because the different nature of the impurity and the confined excitations allows for the creation of new composite particles, with a long lifetime. Thus, the confinement-induced impurity boundstate – an elementary example of baryon formation – can serve as a new probe of confinement physics, which is readily implementable in available quantum simulators.

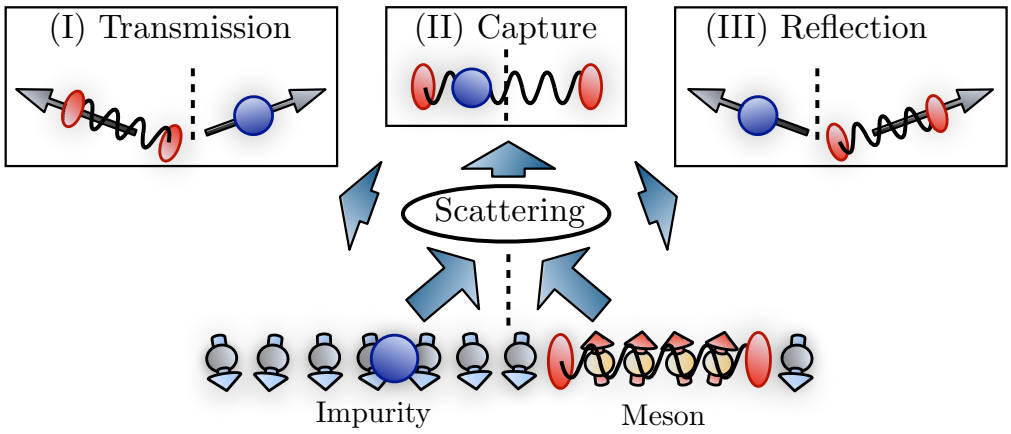

Figure 6.1: Pictorial representation of the impurity-meson scattering and boundstate formation. Besides the instantaneous transmission (I) and reflection (III), the colliding impurity can quantum-tunnel through the first quark and form a metastable boundstate (II). This composite excitation decays when the impurity tunnels again through one of the two quarks.

6.1 The Model

Given the quantum simulation results from previous chapters we focus on the TFIM with an additional longitudinal field, Eq. 3.8, as an experimentally feasible setting. In the following we have replaced the notation of j, the position of the first domain-wall, and n, the width of a meson, with j_1 and j_2 in which j_i labels the position of the i^{th} domain-wall. Furthermore, we set $J = 1$ without loss of generality. While the form of the Hamiltonian governing the bulk dynamics is crucial for the capture process, the precise form of the impurity is not, as clarified by the forthcoming semiclassical picture. Nevertheless, for the sake of concreteness we focus on a simple local spinflip coupling of the impurity to the spin chain,

$$V = \sum_j (h_x - d)\sigma_j^x c_j^\dagger c_j \,; \quad H_{\mathrm{I}} = -\sum_j \tau(c_{j+1}^\dagger c_j + c_j^\dagger c_{j+1}). \tag{6.1}$$

This basic tight-binding term allows the study of a dynamical impurity with hopping strength τ. The entire system evolves with $H = H_{\mathrm{Ising}} + H_{\mathrm{I}} + V$. For $d = 0$, the spin flip is entirely suppressed at the impurity's position and for $d = h_x$ the impurity is invisible. For a single impurity, c_j can be equivalently chosen to obey standard fermionic or bosonic commutation relations. In the following section we show that the interplay of confinement physics and an impurity can lead to exotic metastable particles.

6.2 Confinement and Metastable Trapping

In a scattering event between a meson and the impurity, the meson can be reflected by the impurity or transmitted through the impurity, the latter of which only occurs if both domain-walls tunnel through it. Given that the domain-wall-impurity transmission probability, T, is small but not negligible, a single domain-wall-impurity transmission may occur but the simultaneous tunneling of both domain-walls is suppressed as it has a probability of $O(T^2)$, see Fig. 6.1. In this case and in the absence of confinement, the transmitted and reflected fermions will eventually leave the scattering region. However, a confining force in combination with a small transmission rate can trap the two domain-walls on opposite sides of the impurity for very long times. To substantiate this intuitive picture, we first consider the limit of an infinitely massive impurity, $\tau = 0$, where the defect loses any dynamics and remains pinned. We first use a semiclassical description of meson impurity collisions which gives a surprising depth of understanding.

6.2.1 Semi Classical Approximation

In our spin chain the classical limit is approached for vanishing longitudinal field; this was introduced in Section 3.2.2. In the following we treat the static impurity as a point-like scattering center, which transmits a fermion with probability $T(k)$. Aside from the randomness in the scattering process, the fermions are evolved with the deterministic classical equation of motion. We stress that $T(k)$ is not the mesonic transmission rate, but the much simpler one-particle tunneling computed in the absence of confinement, given by

$$T(k) = \frac{4\sin^2 k}{(d/h_x)^2 + (d/h_x)^{-2} - 2\cos(2k)}; \tag{6.2}$$

the derivation of this can be found in Appendix C.1. We now consider the lifetime of an already trapped meson, which is most conveniently labeled by the momenta of the two fermions at the moment of impact with the impurity (k, q). Let $P_{t=0}(k, q)$ be the probability of forming the boundstate immediately after the scattering; we are now interested in addressing the probability that it remains bound after a time t. Notice that, in the case of a static impurity, $\tau = 0$, the fermions scatter with the

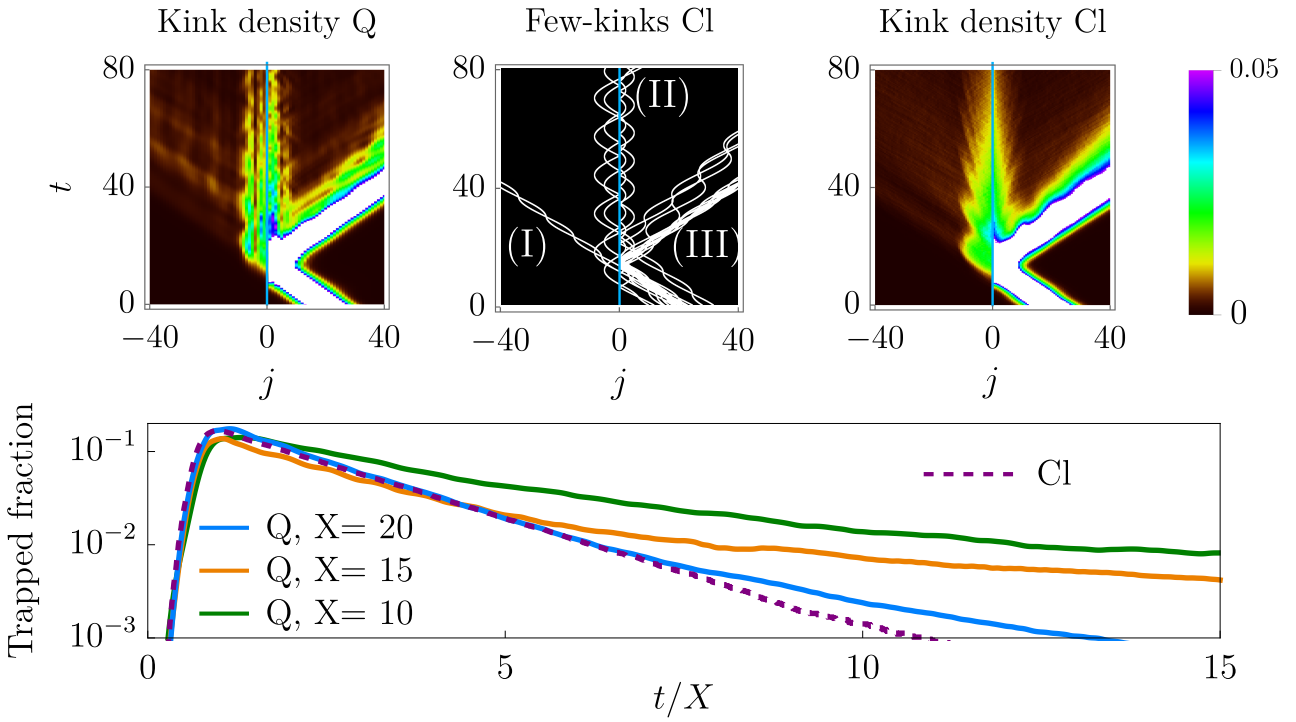

Figure 6.2: In the two domain-wall subspace, we initialize the two fermions in a wavepacket centered at X and shoot it at a static impurity ($\tau = 0$). X is used as control parameter to attain the classical limit $X \to \infty$, by increasing the variance of the wavepacket and reducing the confining potential $\chi \propto X^{-1}$, see Appendix C.1 for details. Top: the scattering event at short times is analyzed by plotting the fermion density for the largest $X = 20$. In particular: *left* quantum simulation, *middle* domain-wall trajectories for few classical events highlighting the three scattering process sketched in Fig. 6.1. While most of mesons are reflected (III), some are transmitted (I) and others remain trapped (II). *Right:* saturation to a large number of classical events ($\sim 4 \times 10^4$). Bottom: trapped fraction $\sum_{j_1 \leq 0, j_2 > 0} |\psi(j_1, j_2)|^2$ as a function of time. We show the quantum curves for $X = 10, 15, 20$ and the classical curve for $X = 20$, since only small differences were observed for the other choices. The time is measured in units of h_x^{-1}.

impurity always with momenta (k, q) for the whole boundstate lifetime. Boundstates with the longest lifetime are characterized by small transmission probability of the fermions. Their lifetime can thus be computed as the probability that neither of the two fermions is transmitted. Hence, the probability of being trapped at time t is

$$P_t(k,q) = \exp\left[-t\frac{\chi}{2}\left(|k|^{-1}T(k) + |q|^{-1}T(q)\right)\right] P_{t=0}(k,q)\,; \tag{6.3}$$

see Appendix C.2 for details. At low momentum, the discrete fermion-impurity Hamiltonian can be treated in the continuum $H_{\text{eff}} = -(2m_{\text{eff}})^{-1}\partial_x^2 + v_{\text{eff}}\delta(x)$, leading to a quadratically vanishing transmission $T(k) \propto k^2$ as $k \to 0$. Therefore, small momenta have a divergent lifetime. Following this argument, one could expect a power law decay of the total trapped fraction $\int \mathrm{d}k\mathrm{d}q P_t(k,q)$, but this is not the case because the two momenta (k, q) are not independent. In particular, it is not possible to have $k \simeq q \simeq 0$ at the same time and the exponential decay is restored. To determine the initial trapped probability $P_{t=0}$, the full time evolution of the colliding meson must be addressed. Remarkably, $P_{t=0}(k, q)$ can be explicitly computed in the limit of broad wavepackets, see Appendix C.2. While semiclassical methods are able to build out the intuitive picture of metastable trapping into a solid physical phenomenon, in order to capture the quantum details we utilise the two domain-wall approximation.

6.2.2 Two Domain-Wall Subspace

To test the general semiclassical treatment and clarify the nature of quantum corrections, we revert to the weak transverse field regime where the Ising dynamics can be projected onto the two domain-wall subspace given by Eq. 3.9. The effect of the defect is to replace the hopping amplitude on the defect site form $h_x \to d$. There are several advantages within this approximation. First, the effective two-body problem can be simulated for large system sizes and for long times. Second, one has far better control of the form of the initial wavepacket. Third, the fermion-impurity transmission probability $T(k)$ can be exactly computed.

In Appendix C.1 we show how a standard truncated Wigner approximation [147] allows to quan-

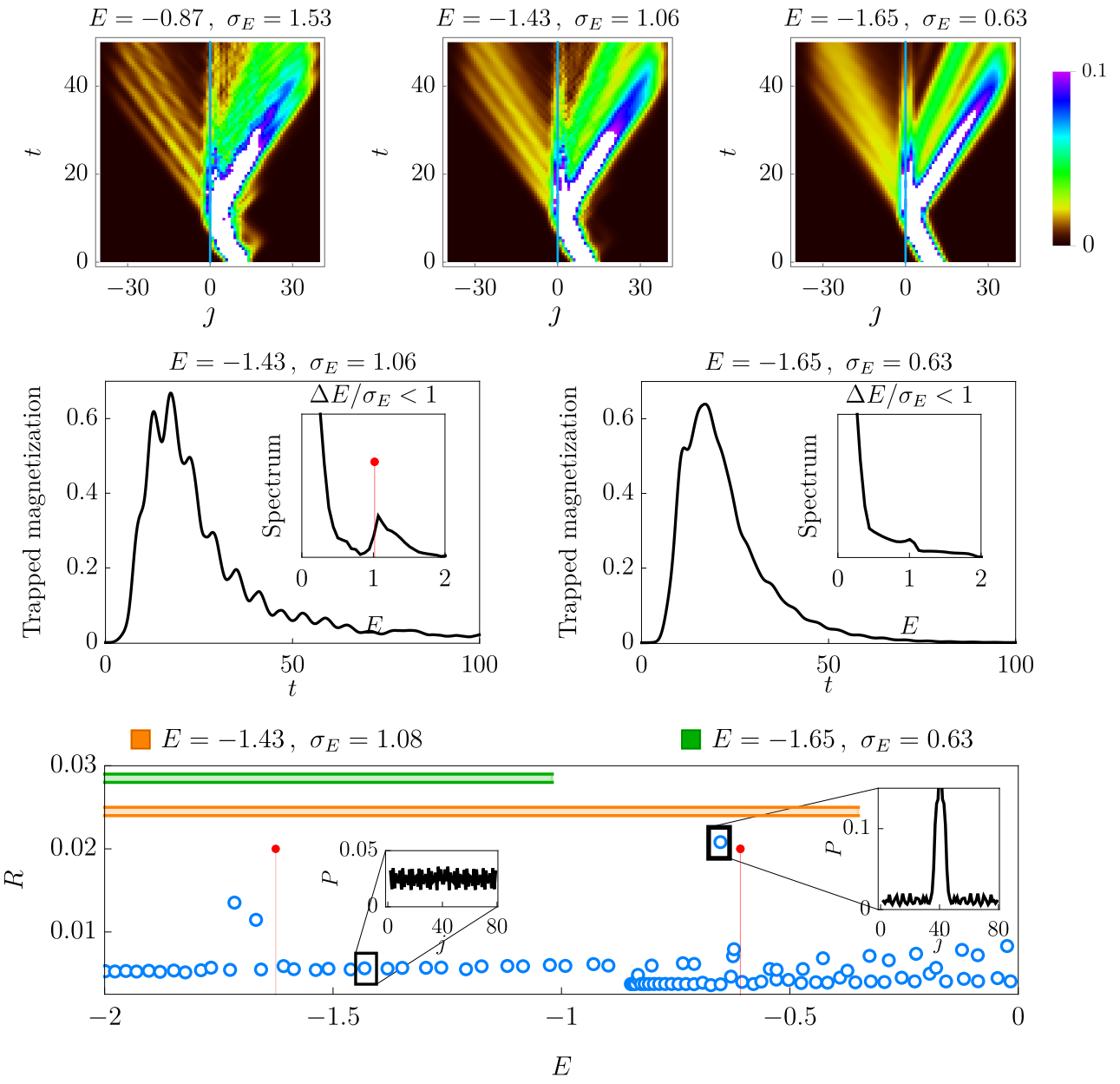

Figure 6.3: In the two domain-wall subspace, we fix $\chi/h_x = 0.5$ and $d/h_x = 0.4$. Top: wavepackets of similar envelope (see Appendix C.1 for details), but different mean energy E and variance σ_E are shot at the defect. The density plot of the fermion density is shown. Middle: for the middle and rightmost parameter choice displayed in the density plots, we show the trapped magnetization $\sum_{j_1\leq 0, j_2>0} |j_1 - j_2||\psi(j_1, j_2)|^2$ as a function of time. Insets: Fourier transform (vertical axis constant but arbitrary units), the pins track the energy differences of the semiclassical quantized boundstate energies within one sigma from the wavepacket mean energy. As σ_E is reduced, fewer metastable states are excited and the oscillations due to interferences are damped. The time is measure in units of h_x^{-1}. Bottom: on a system of $L = 80$ sites with periodic boundary conditions (defect at site 40), we numerically compute the participation ratio $R = \sum_{j_1<j_2} |\psi(j_1, j_2)|^4$ of the energy eigenstates. Pins are the semiclassical quantized energies. boundstates have large R when compared with naive asymptotic states. The small oscillating tails of the density profile leaving the defect region (inset, $P(j) = \sum_{j_1\leq j} |\psi(j_1, j)|^2 + \sum_{j_2>j} |\psi(j, j_2)|^2$) lead to the finite lifetime. Green and orange bar shown the extension of the energy interval within one sigma from the average energy probed by the two plots in the middle.

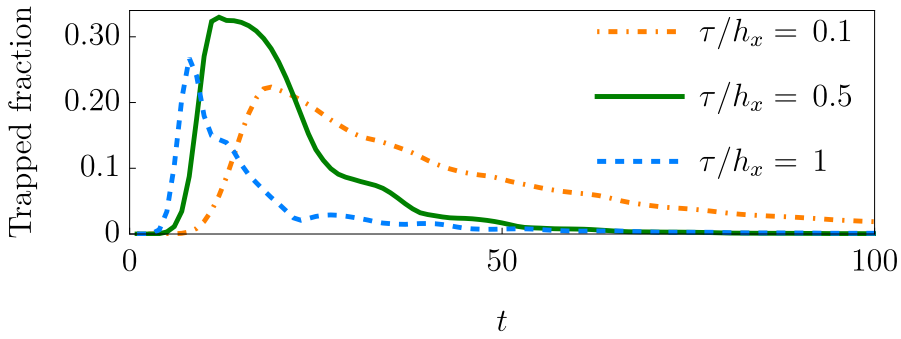

Figure 6.4: In the total zero momentum sector, we consider the scattering of a mobile impurity with a meson. The initial conditions, defect strength and confinement are kept fixed while varying τ and are such that for $\tau = 0$ they match Fig. 6.2 with $X = 20$.

titatively connect the initial quantum mechanical wavepacket with the proper classical phase space distribution. In Fig. 6.2 we provide the quantum-classical comparison, showing good agreement.

In Fig. 6.3 we consider a scattering event in the two domain-wall subspace, but with larger longitudinal field and far from the semiclassical regime. Pronounced oscillations appear in the density of fermions leaving the defect and in the time evolution of the trapped magnetization. We will now show that these frequencies are in good qualitative agreement with a semiclassical quantization of the boundstate energies.

From the classical perspective, a trapped meson is a pair of fermions on opposite sides of the impurity, see Fig. 6.1 (II). Each of the two fermions feels a constant force pulling towards the barrier, which acts as a hard wall until a tunneling event takes place. Pushing this interpretation to the quantum regime, we can write the single particle time-independent Schrodinger equation for the right fermion as $E_n\psi(j) = -h_x(\psi(j+1) + \psi(j-1)) + \chi|j|\psi(j)$, valid for $j > 0$ and with boundary condition $\psi(0) = 0$. An analogue equation holds for the left fermion. This equation can be analytically solved for the quantized energies $\{E_n\}_{n=0}^{\infty}$. Therefore, the energies of a metastable state are labelled by two quantum numbers $E_{n_1,n_2} = E_{n_1} + E_{n_2} - \chi$, with the $\chi-$shift taking into account the string tension on the defect link. In Fig. 6.3, we show that the oscillation frequencies are close to the energy differences of the quantized metastable states. We selectively excite the quantized metastable states by shooting wavepackets with mean energy E and narrow variance σ_E. If σ_E is large enough to excite more than one metastable energy, clear oscillations are produced.

We now address the case of a truly dynamical impurity with $\tau \neq 0$. For the sake of simplicity, we

consider the weak transverse field regime and the subspace of a fixed constant momentum, which can be addressed in the two domain-wall approximation. The semiclassical picture we discussed for a static impurity can be readily applied to the case $\tau \neq 0$ by using the equation of motion and the fermion-impurity transmissivity rate, which can be exactly computed for weak h_x, see Appendix C.1. As expected, $\tau \neq 0$ increases the relative impurity-fermion motility, increasing the transmission rate and shortening the lifetime of the metastable state which is nevertheless still present, see Fig. 6.2.2. However, the simple result of Eq. (6.3) cannot be applied any longer, since each fermion is not simply reflected as $k \to -k$ due to the momentum exchange with the impurity. In contrast, the fermion-impurity scattering process is largely affected by the defect's velocity [148, 149] and, outside the two domain-wall approximation, the moving impurity can act as a moving source of excitations [150].

Finally, in order to validate that metastable trapping of a meson around an impurity is not limited to subspace approximations, we turn to a time-evolving block decimation approximation to simulate the time dynamics of the full Hilbert space.

6.3 Time-Evolving Block Decimation Results

We finish by numerically simulating the meson-impurity scattering with the time evolving block decimation (TEBD) method to allow us to confirm that the few domain-wall approximations accurately describe the full Hilbert space [151, 152]. Details on the numerical implementation and the wavepacket preparation are given in Appendix C.3. After shooting a meson at the impurity (see Fig. 6.5) we see that part of the wavepacket can be trapped within the defect region for long times, depending on the confining force and the defect strength. We experience that for stronger defects the signal is mostly reflected, but a small part of it remains trapped for longer times, suggesting the sought after metastable boundstate does indeed form.

While the current capabilities of the IBM quantum computers restrict our focus to short range models, other setups do not - namely trapped ion and neutral atom based devices. Thus, in the following chapter we consider a broader context of experimental feasibility and explore collisions of mesons that form in the long-range TFIM introduced in Section 3.2.3.

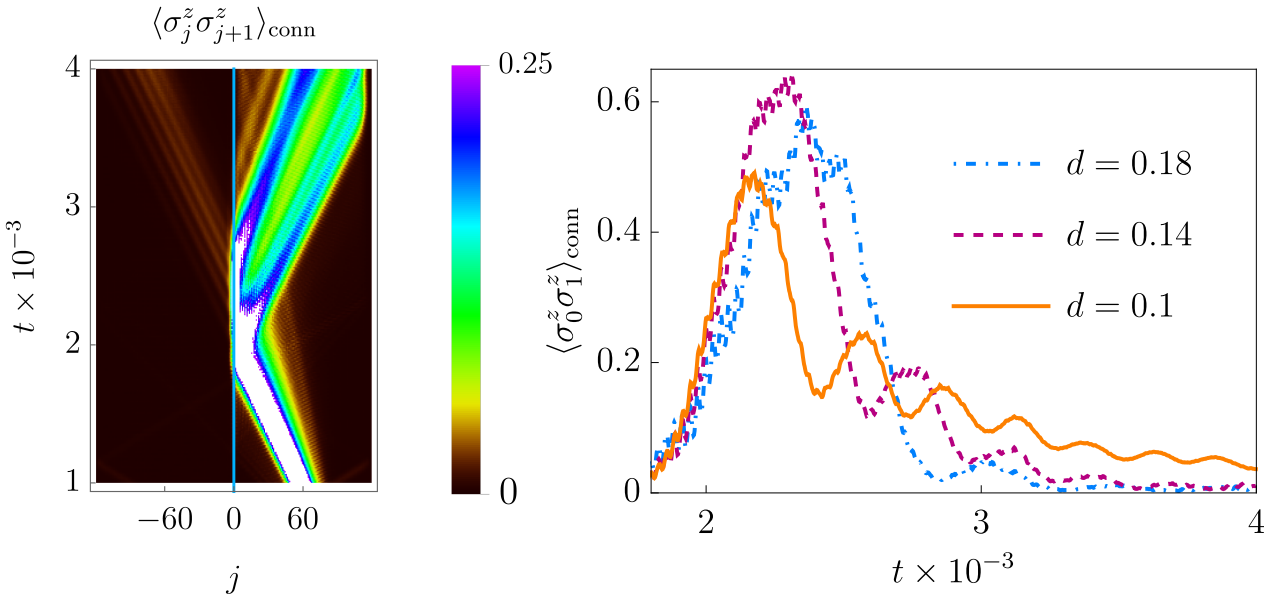

Figure 6.5: TEBD simulation of the scattering of a meson against an infinitely massive impurity. The correlator $\langle \sigma^z_j \sigma^z_{j+1} \rangle$ (connected part) tracks the position of domain-walls. We chose $h_x = 0.3$, $h_z = 0.12$. and different values of the defect strength. Left: density plot for $d = 0.1$, showing domain-walls are trapped on the impurity at the origin for very long times. Right: domain-wall density on the defect for different defect strengths. After a large peak corresponding to the impact of the meson wavepacket with the defect, some signal remains trapped for longer times. As the defect's strength is increased, the magnitude of the trapped signal is reduced, but its lifetime is increased. Details on the wavepacket implementation can be found in Appendix C.3

Chapter 7

Dynamical Hadron Formation in Long-Range Interacting Quantum Spin Chains

In the previous chapter we studied collision events in the short-range Ising model with both transverse and longitudinal fields. In order to observe a 'fusion' event we considered the addition of a heavy impurity to the system. Deep inelastic scattering events with exotic particle formation without the addition of a foreign body require richer microscopic dynamics. In this work, we investigate another mechanism that can lead to dynamical hadron formation by addressing the TFIM with long-range interactions which, in addition to confinement, naturally induces interactions among mesons and hosts multi-meson boundstates, akin to hadrons. We will further show that the presence of long-range interactions between mesons can result in the formation of long-lived hadronic *metastable* boundstates, which can form dynamically in scattering events between fundamental mesons as depicted in Fig. 7.1. This chapter closely follows the work published in Ref. [4] in which Joseph Vovrosh was the main contributor. In particular, all authors were involved in the theoretical discussions led by Joseph Vovrosh, the analytical calculations and numerical simulations were performed by Joseph Vovrosh and the experimental feasibility established by Rick Mukherjee following discussions with Joseph Vovrosh. We begin by showing how long-range interactions can lead to boundstates of pairs of mesons, which we call *tetraquarks*.

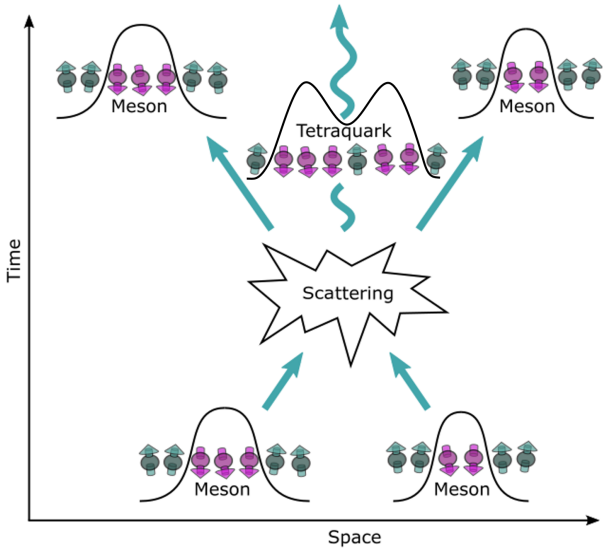

Figure 7.1: A schematic of a scattering event between two wavepackets of confinement-induced mesonic (two domain-wall) states. Apart from the elastic meson reflection, the long-range interaction between the composite particles may also lead to the formation of multi-particle boundstates, here in the form of a metastable four domain-wall state akin to a tetraquark.

7.1 Hadrons in the Long-Range Ising Model

In this work, we consider the one dimensional Ising spin chain with long-range interactions given in Eq. 3.17. As our goal is the observation of hadron-like excitations, we need to consider interactions among mesons. Thus, we focus on the dynamics within the four domain-wall subspace and use a straightforward extension of the two domain-wall projection Eq. 3.9. We consider the basis $|j_1, n_1, j_2, n_2\rangle = |\uparrow \ldots \uparrow\downarrow_{j_1} \ldots \downarrow\uparrow_{j_1+n_1} \ldots \uparrow\downarrow_{j_2} \ldots \downarrow\uparrow_{j_2+n_2} \ldots \uparrow\rangle$, in which the projected Hamiltonian takes the shorthand form

$$\begin{aligned} H = \sum_{j_1,n_1,j_2,n_2} & V(n_1)\,|j_1,n_1,j_2,n_2\rangle\,\langle j_1,n_1,j_2,n_2| \\ & + V(n_2)\,|j_1,n_1,j_2,n_2\rangle\,\langle j_1,n_1,j_2,n_2| \\ & + I(j_1,n_1,j_2,n_2)\,|j_1,n_1,j_2,n_2\rangle\,\langle j_1,n_1,j_2,n_2| \\ & - h\big[\text{hopping terms}\big]. \end{aligned} \tag{7.1}$$

Here, $I(j_1, n_1, j_2, n_2)$ can be seen as the meson interaction such that [153]

$$I(j_1,n_1,j_2,n_2) = -4 \sum_{j_1<r\leq j_1+n_1} \sum_{j_2<s\leq j_2+n_2} \frac{1}{(s-r)^\alpha} \tag{7.2}$$

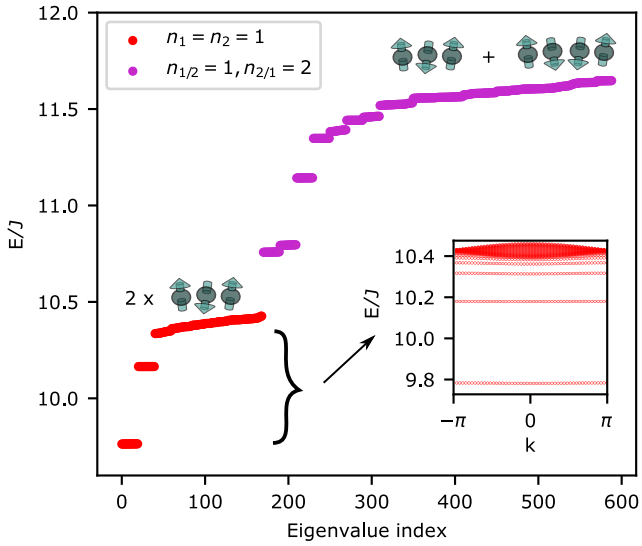

Figure 7.2: The low energy states of the four domain-wall subspace are shown for $L = 20$, $\alpha = 2.6$ and $h = 0.1$. The energies strongly depend on the average size of the constituent mesons resulting in large gaps between levels of different meson sizes. A schematic picture of the local spin configurations within each subspace are depicted above the corresponding energy levels. Importantly, due to the long-range interaction the energy within each subspace also depends on the distance between the two mesons, i.e. the closer the mesons are together the lower their energy. The inset shows the energies of the 1-meson subspace as a function of momentum. The lowest energy levels in this subspace are boundstates of multiple constituent domain-walls.

and "hopping terms" refer to those of the form $|j_1 \pm 1, n_1 \mp, j_2, n_2\rangle \langle j_1, n_1, j_2, n_2|$ or equivalently for the second meson. Note, the form of the interaction, I, depends on the choice of boundary conditions. Here, we consider open boundaries. This effective interaction between mesons falls off as $d^{-\alpha}$ in which d is the meson separation $\sim (j_2 - j_1)$. Thus, individual mesons which are far apart from each other interact only weakly.

In Fig. 7.2 we show some of the lower energy levels of the four domain-wall subspace. We clearly see large energy gaps in correspondence with internal quantum numbers, labeling the energy levels of the two domain-wall mesons. Additional structure is then provided by boundstates of fundamental mesons and asymptotic scattering states (see inset). In the case of deep boundstates where the binding energy is much larger than the transverse field h, the two domain-wall mesonic wavefunction is very peaked on integer values of the relative distance, hence the meson has approximately fixed length which is in one-to-one correspondence with the internal energy levels. In this regime, we can pictorially use the meson's size as a good quantum number. Nonetheless, this correspondence is blurred as boundstates become shallower and domain-walls can oscillate with internal dynamics. To further

substantiate this intuition, we spend some time analysing the subspace of two mesons each with width $n = 1$ in the next section.

Note, as mentioned previously in Section 3.2.3, confinement in a strict sense requires $1 < \alpha < 2$ such that domain-walls cannot be separated. Nonetheless, also for larger α the two domain-wall subspace shows the presence of deep boundstates and asymptotic states of freely propagating domain-walls can be very high in energy and extremely difficult to excite. Therefore, as long as asymptotically propagating domain-wall states can be neglected, the dynamics of these deep two domain-wall boundstates closely resemble those observed in the strictly confined regime, and with a slight abuse of jargon we refer to both as "mesons". Due to the fact that larger values of α mitigate finite-size corrections caused by the long-range potential, we will mainly focus on the regime $\alpha \sim 2.5$ but stress that similar physics appears for $1 < \alpha < 2$.

7.2 The 1-Meson Subspace

Consider the subspace of $n-$mesons in the low energy regime where n is a approximately conserved. To first order in h, projecting the four domain-wall subspace Hamiltonian, given in Eq. 7.1, to the $n-$meson subspace does not include dynamics of the mesons. This is due to the fact that any spin flip process will leave this subspace; the mechanism of dynamics within the $1-$meson subspace is depicted in Fig. 7.3. Thus, in order to get an accurate description within a restricted $n-$meson Hamiltonian we must consider second order processes. This derivation can be obtained through perturbation theory, for example, consider the $1-$meson subspace with the simplified basis $|j_1, j_2\rangle = |\uparrow \ldots \uparrow\downarrow_{j_1}\uparrow \ldots \uparrow\downarrow_{j_2}\uparrow \ldots \uparrow\rangle$. Our starting point for the projection of the Hamiltonian into the $1-$meson subspace is the Hamiltonian H given in Eq. 7.1 which may be factored into a diagonal part H_0 and an off-diagonal part V proportional to what we will consider the perturbative parameter h, that is $H = H_0 + hV$. Our goal is to find a unitary transformation generated by an operator S such that the expansion $H^{eff} = e^S H e^{-S} \sim H_0 + h^2 M + O(h^3)$ *i.e.* the lowest order hopping events are proportional to h^2. V contains the hopping terms of the Hamiltonian; the resulting effective Hamiltonian thus contains only on-site potentials and two-site hopping interactions (plus higher order terms which are absorbed into the $O(h^3)$ factor). This rotation is known as the Schrieffer-Wolff transforma-

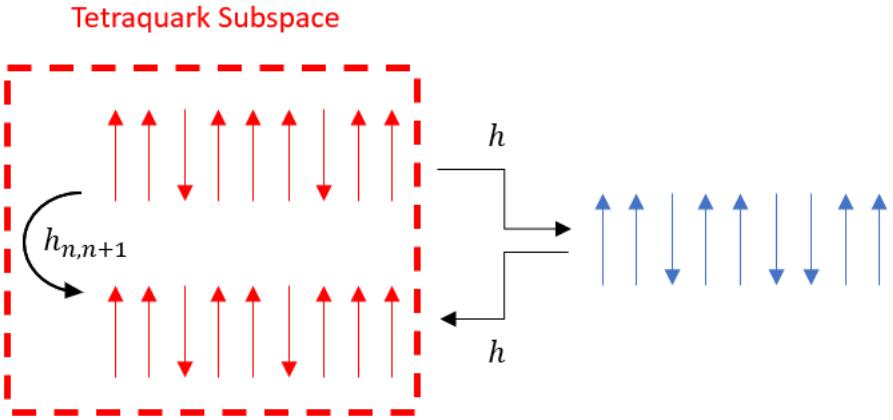

Figure 7.3: A schematic of the second order hopping process required for a $1-$meson to move.

tion [154]. To proceed, we write down the Baker–Campbell–Hausdorff expansion of $e^S H e^{-S}$ up to second order in h:

$$H^{eff} = e^S H e^{-S} = H_0 + hV + [S, H_0] + h[S, V] + \frac{1}{2}[S, [S, V]] + O(h^3) \, . \tag{7.3}$$

We can eliminate the first order terms by choosing S such that $[S, H_0] = -hV$. The simplest way to do this is element-by-element, enforcing

$$\langle p|S|q\rangle = \frac{h\langle p|V|q\rangle}{E_p - E_q} \, , \tag{7.4}$$

where $|p\rangle, |q\rangle$ are eigenvectors of H_0 with eigenvalues E_p, E_q. With this enforced, the effective Hamiltonian becomes

$$H^{eff} = H_0 + \frac{h}{2}[S, V] + O(h^3) \, . \tag{7.5}$$

We then project this effective Hamiltonian into the $1-$meson subspace and obtain two contributions to the Hamiltonian, a hopping coefficient, h_j, in which a $1-$meson hops one site away from the other. There is also a second order effect in which a $1-$meson can 'hop to itself' through a process in which a neighbouring spin flips and then flips again to leave the initial state unchanged, U_j. In the $1-$meson

subspace this can be seen as an effective on site potential. These contributions are given by

$$h_j = \frac{h^2}{2}\left[\frac{1}{V(1)-V(2)+\frac{4}{j+1^\alpha}}+\frac{1}{V(1)-V(2)+\frac{4}{j^\alpha}}\right], \tag{7.6}$$

$$U_j = 2h^2\left[\frac{1}{V(1)-V(2)+\frac{4}{j+1^\alpha}}+\frac{1}{V(1)-V(2)+\frac{4}{j-1^\alpha}}\right], \tag{7.7}$$

where $j = j_2 - j_1$. Given these contributions the $1-$meson subspace is

$$H = \sum_{j_1,j_2} h_{j_2-j_1}[|j_1, j_2+1\rangle\langle j_1, j_2| + |j_1-1, j_2\rangle\langle j_1, j_2| + h.c.] + \left(U_{j_2-j_1} - \frac{4}{n^\alpha}\right)|j_1, j_2\rangle\langle j_1, j_2|\,. \tag{7.8}$$

From here, we can take advantage of translational invariance and focus on the sector with global momentum k, where we use the relative distance $j = j_2 - j_1$. The momentum-dependent Hamiltonian, H_k, acting on the states $|k, j\rangle$ is given by

$$H = \sum_{k,j} 2h_j \cos\frac{k}{2}\left[\,|k, j+1\rangle\langle k, j| + h.c\right] + \left(U_j - \frac{4}{j^\alpha}\right)|k, j\rangle\langle k, j|\,, \tag{7.9}$$

which we can use to calculate the energies as a function of momentum. In Fig. 7.4 we compare the energies of the $1-$meson subspace with the corresponding energies of the four domain-wall subspace as well as the full Hilbert space. Here we see that not only does the $1-$meson subspace have good agreement with the four domain-wall subspace as expected but also with the full Hilbert space.

One can clearly see that the lowest energy levels are discrete with large gaps between them, which correspond to boundstates of two mesons that reside only a few sites away from each other, i.e. they describe tetraquarks. In addition, there is a continuum of energy levels at higher energy corresponding to mesons which are spatially separate and interact only weakly, i.e they are free to propagate.

Before turning to real-time numerical simulations of scattering events, it is useful to further comment on the meson-meson boundstate structure, i.e. our cartoon picture of hadrons. As shown in Fig. 7.2, energy levels corresponding to hadrons are clearly visible in the spectrum, their number and gap with respect to the asymptotic scattering states depends on the "size" (i.e. the energy) of the binding

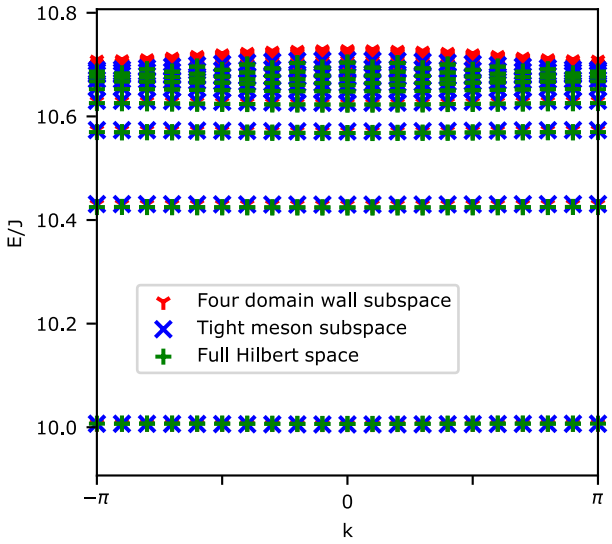

Figure 7.4: A comparison of $1-$meson energies in the $1-$meson subspace, the four domain-wall subspace as well as the full Hilbert space. Here $L = 20$, $h = 0.1$ and $\alpha = 2.5$. We see excellent agreement between all three. Note, the energies of the full Hilbert space have been shifted by a constant to account for finite size effects.

mesons. These boundstates are clearly orthogonal to asymptotic scattering states, hence scattering events cannot couple to them. If we wish to observe dynamical hadron formation, we should aim for metastable states arising from asymptotic scattering states whose wavefunction is large when mesons are close, which means that they are qualitatively close to true boundstates. Heuristically, these states are most likely to be present where the spectrum shows a smooth transition between boundstates and scattering states, i.e. when the energy gap between the two is small. As it is clear from Fig. 7.2, this is the case for large mesons. This picture is also suggested by semiclassical arguments, since for large mesons the relative position of the domain-walls can oscillate. Therefore, part of the scattering energy of the two incoming mesons can be converted to internal energy of the mesons upon scattering and a boundstate may form. This is not possible for tightly bound mesons, where the relative position of the domain-walls cannot be changed. These considerations motivate the use of large mesons in the following natural scattering protocol.

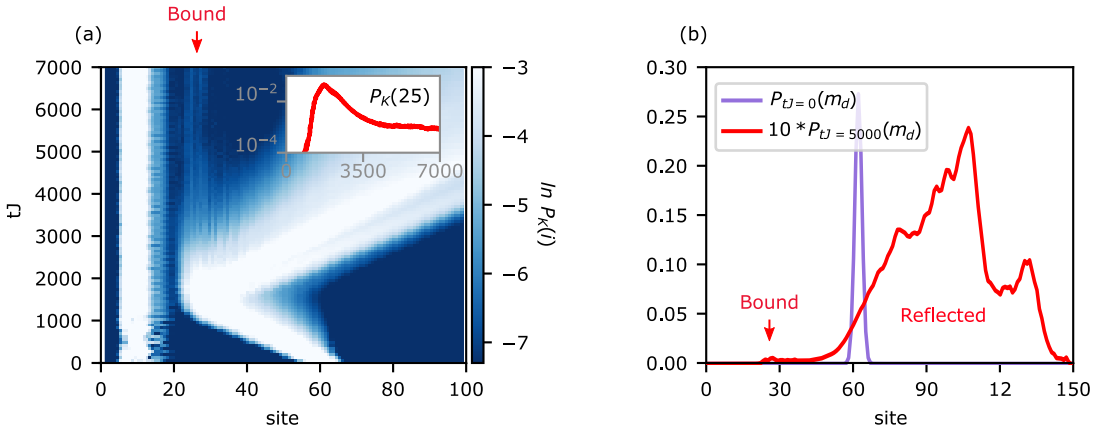

Figure 7.5: The dynamical formation of a tetraquark through an inelastic collision of large mesons. Here, the Hamiltonian parameters are $L = 150$, $\alpha = 2.6$ and $h = 0.1$. The full details of initial wavepacket can be found in Appendix D.1. (a) The collision between a mobile meson initialized with a width of 4 sites and a stationary meson with initial width of 10 sites. Although the vast majority of the incoming wavepacket is reflected there is a subtle excitation of a tetraquark that can be seen as the faint vertical lines at sites ~ 25. Furthermore, an inset plots the cross section of the time dynamics at site 25 showing the long life time of the tetraquark formed. Note, we choose to plot sites up to 100 as this contains the relevant information for our discussion. (b) The probability distribution of $m_d = j_2 + n_2$ at times $tJ = 0$, the initial wavepacket, and $tJ = 5000$, after the collision event. After the collision, we clearly see that the majority of the wavepacket is reflected, however, there is a subtle peak at site ~ 25 that corresponds to a bound tetraquark state.

7.3 Inelastic Collisions of Large Mesons

We now consider the Hamiltonian projected in the four domain-wall subspace and numerically explore scattering events between mesons. As initial states, we choose Gaussian meson wavepackets with a well-defined momentum. Furthermore, we fix the average length of each meson to cover a few lattice sites $\sim 4 - 12$. Details on the wavepacket wavefunctions can be found in Appendix D.1. Simulations in the four domain-wall subspace are challenging for large system sizes. Therefore, we take advantage of global momentum conservation and focus on the sector with zero total momentum. Using translational invariance we measure the domain-wall coordinates with respect to the leftmost domain-wall which can reduce the Hilbert space dimension by a factor L allowing us to access much larger systems.

In the zero-momentum sector we can then label the Hilbert space by only three variables $|n_1, j_2, n_2\rangle$ as the first domain-wall can be pinned to $j_1 = 0$. As a consequence of this convention, in our real-time simulation the leftmost meson will appear stationary. In Fig. 7.5(a) we show a collision event between

a left meson of initial width $n_1 = 10$ with a right meson with initial width $n_2 = 4$. We employ the observable $P_K(i) = |\langle\psi|(1 - \sigma_i^z\sigma_{i+1}^z)|\psi\rangle|^2$ which can be seen as the probability that a domain-wall is located on site i. In Fig. 7.5 we observe that scattering is dominated by elastic reflection events. However, by plotting the logarithm of the data we are able to highlight subtle details, e.g. a small portion of the wavepacket $\sim 10^{-3}$ remains close to the stationary meson for long times after the collision which can be seen as a vertical line of intensity at site ~ 25 in Fig. 7.5(a).

Next, we study a basic measure of the 'distance' between the two mesons $m_d = j_2 + n_2 - j_1$. In Fig. 7.5(b) we plot the probability distribution of m_d before ($tJ = 0$) and after the collision ($tJ = 5000$). After the collision the distribution has two components. First, the overwhelming probability accounts for reflection events seen as the large hump for sites > 40. However, there is a second, small peak around site ~ 25 which is a signature of our sought-after metastable tetraquark state. However, for all parameter and initial state choices we have explored, the signatures of dynamical tetraquark formation are weak as elastic scattering dominates. Therefore, in the following, we propose two simple extensions of the natural meson scattering protocol which allow for an unambiguous observation of dynamical tetraquark formation.

7.4 Inducing Fusion Events

To enhance the effect, we propose two different modifications of the scattering protocol. Firstly, by an abrupt dynamical change of an external field one can modify the mesons' kinetic energy and induce a non-trivial overlap between the initial asymptotic states and the hadronic boundstates of the post-quench Hamiltonian. As a result, infinitely long-lived boundstates are created and clearly observable. Secondly, we consider time-independent Hamiltonians with a modified long-range spin interaction, which leads to a non-monotonic meson-meson interaction. Consequently, scattering mesons can tunnel to a local minimum of the relative interaction and dynamically form a long-lived metastable boundstate, which again becomes clearly observable in the collision.

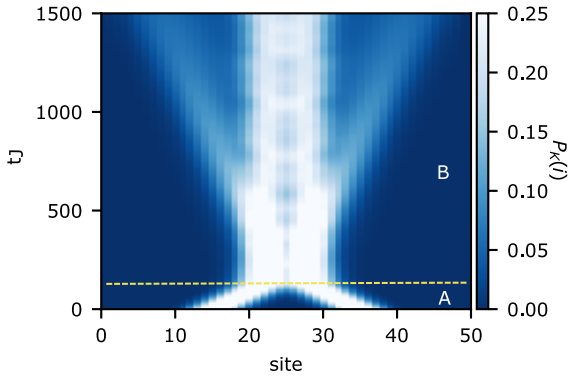

Figure 7.6: The dynamical formation of a tetraquark with an abrupt change of the transverse field (calculated in the full four domain-wall subspace). Here, the Hamiltonian parameters are $L = 50$ and for $\alpha = 2.6$. The full details of the initial wavepacket can be found in Appendix D.1. In section A (up to the yellow dashed line) two 1-meson wavepackets move toward each other with a large kinetic energy (transverse field $h = 0.2$). Then at the point of meson collision ($tJ = 125$) a abrupt change to a smaller transverse field ($h = 0.1$) is performed reducing the kinetic energy in section B. This reduction of kinetic energy can be seen by comparing the fast velocity of the meson wavepackets in section A to the slow velocity in section B. We see that this process induces the formation of a tetraquark with exotic internal dynamics.

7.4.1 An Abrupt Change to the Transverse Field

In natural collisions of mesons we only observed weak signals of dynamically formed tetraquark states. True boundstates are clearly present in the spectrum but as we have already mentioned, these are orthogonal to the scattering states of our wavepacket. In the following we explore the possibility to artificially induce non-trivial overlaps between these two classes of states by dynamical changes in the Hamiltonian. As the most basic example, we consider abrupt changes in the transverse field h at the time of collision t^*. We note that the very nature of the so-obtained hadrons is very different from the previously considered metastable states because now true boundstates are excited with an infinitely-long lifetime.

In Fig. 7.6 we implement the proposed protocol. We initialize the $1-$meson Gaussian wavepackets with well-defined momentum and suddenly reduce the transverse field at a time t^* when the scattering takes place (dotted horizontal line in the figure). The main part of the signal remains indeed trapped in a boundstate at the center of the chain, thus realising the desired dynamical hadron-forming event. In Fig. 7.7 we show the dispersion relations of the pre/post-quench Hamiltonians as a function of the total momentum k. Boundstates appear as well-separated bands below a high-energy continuum

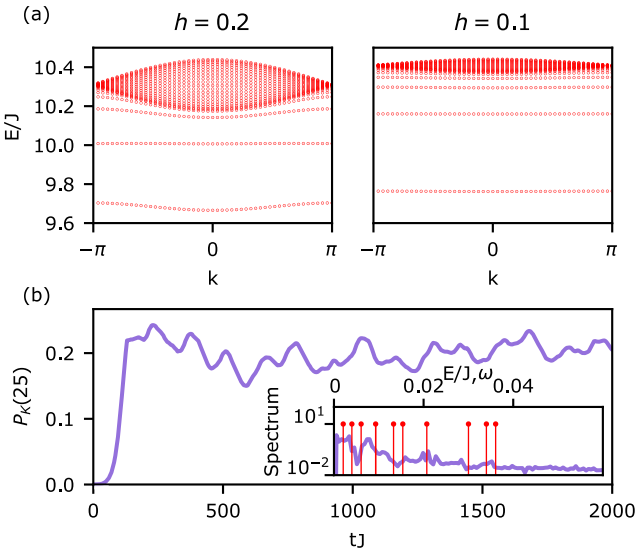

Figure 7.7: Analysis of oscillations in the fusion event shown in Fig. 7.6. (a) The energies of the $1-$meson subspace before (left) and after (right) the change in the transverse field at the time of collision. The larger transverse field broadens the continuum of free meson states which corresponds to increasing their kinetic energy. (b) The time dependence of the central site 25 from Fig. 7.6 showing the internal dynamics of the dynamically formed tetraquark. An inset shows the spectrum of the oscillation frequencies observed. Clear agreement is seen between the dominant frequencies observed and differences in the energy levels E_i of the $1-$meson subspace after the change of field to $h = 0.1$, these are shown by the vertical red lines.

of asymptotic states. Notice that the boundstates for $h = 0.1$ have an almost flat dispersion, hence very small velocities, which explains the trapped stationary signal observed in Fig. 7.6. Albeit hardly moving, the trapped boundstate is oscillating in time. In Fig. 7.7(b) we show that the oscillating frequencies are indeed compatible with the energy gaps between the boundstate energies of the post-quench Hamiltonian.

While the abrupt change of the transverse field protocol is very efficient in exciting boundstates, it can arguably be regarded as an artificial shortcut to our goal of observing multi-meson binding in scattering events. Therefore, we now consider possible modifications of the interactions which can enhance the phenomenon without time-dependent changes.

7.4.2 Modifying the Long-Range Interactions

In the following, it is again useful to focus on the $1-$meson subspace and consider the relative interaction between two mesons shown in Fig. 7.8(a) which is a monotonically decreasing function of

the relative distance (dashed line). An enhancement of boundstate trapping can then be achieved by modifying the spin interactions to form a potential well. For example, this can be achieved with the minor modification of the Hamiltonian

$$H = -\sum_{i,r} \frac{J}{r^\alpha}\sigma_i^z\sigma_{i+r}^z - h\sum_i \sigma_j^x + \frac{J}{d^\alpha}\sum_i \sigma_i^z\sigma_{i+d}^z, \tag{7.10}$$

inducing a potential well in the relative potential at separation d, see the solid curve in Fig. 7.8(a). Two colliding mesons will now see a potential barrier of finite width and a quantum tunneling event may occur in the collision. Physically, this can be understood as increasing the energy of states that have up spins d sites away from each other. In terms of the $1-$meson Hamiltonian this is equivalent to removing the interaction between mesons that are d sites away from each other.

Fig. 7.8(b) shows the effect of the modified interaction for allowing a long-lived tetraquark to form dynamically. Here, we initialized two meson wavepackets with opposite momentum. We observe, as expected, that in the presence of the effective potential well there is a small probability that the mesons tunnels through the potential barrier forming a metastable tetraquark decaying with a lifetime τ. We also show the results of measuring $P_{TQ}(i) = \sum_{\mathcal{C}} |\psi(j_1, n_1, j_2, n_2)|^2$ where $\mathcal{C}$ is the set of basis states such that there is a domain-wall at the i^{th} site and $j_2 - (j_1 + n_1) \leq d$. This observable can be seen as the probability that a tetraquark is located around site i. From this we indeed see that at the point of collision, a tetraquark forms and has a long lifetime (right panel).

The decay of a metastable boundstate via quantum tunnelling is reminiscent of one of the first paradigms of quantum physics – α-particle decay as observed about a century ago and explained by Gamow's famous semi-classical theory [155]. We can go one step further with our spin chain analogy and compare the decay times of bound tetraquarks for varying energies, which can be achieved through varying the depth of the potential well, $\frac{J}{d^\alpha} \to \frac{J}{d^\alpha} - \epsilon$. In Fig. 7.9(a) we plot $\sum_i P_{TQ}(i)$ to observe the decay of states initialized as a tetraquark wavepacket for varying potential well depths. We observe that tetraquarks decay exponentially in time. The lifetime is longer for tetraquarks with lower energy which is consistent with the larger potential barrier between the bound tetraquark and free meson states.

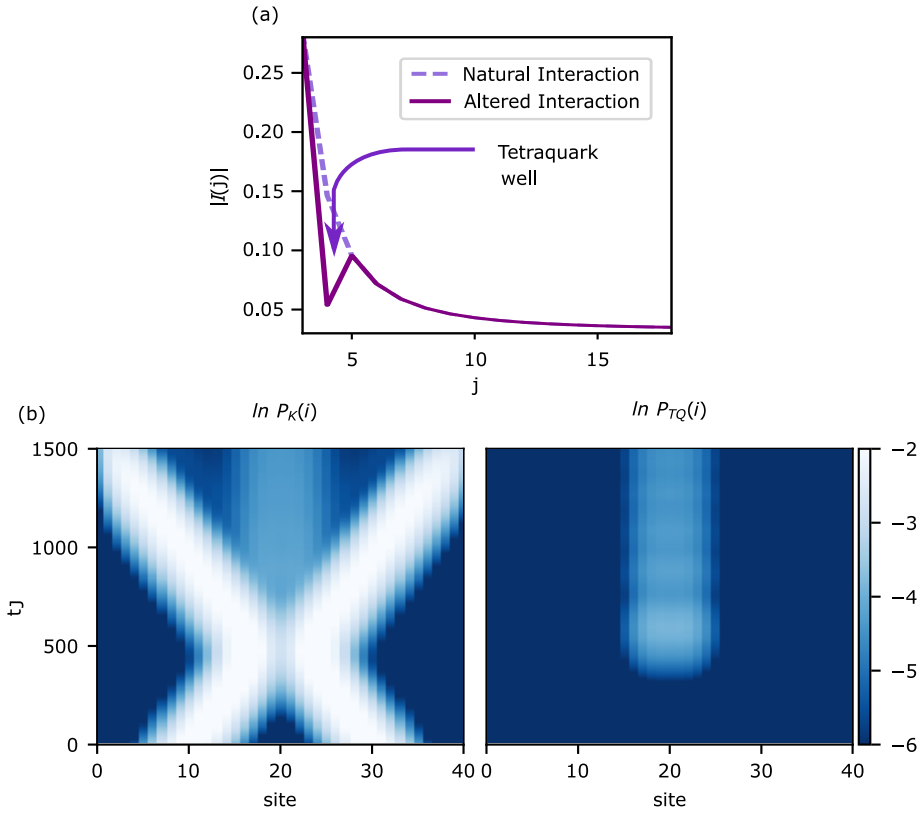

Figure 7.8: The dynamical formation of a tetraquark from a collision of $1-$mesons using a modified long-range interaction with an additional potential well in the form of Eq. 7.10 with $d = 4$. Here, the Hamiltonian parameters are $\alpha = 2.6$ and $h = 0.1$. The full details of the initial wavepacket can be found in the Appendix D.1. Panel (a): The resulting meson-meson interaction is displayed as a function of separation which shows the formation of a tetraquark well. Note, here $I(j) = U_j - \frac{4}{j^\alpha}$. Panel (b): In addition to the main elastic scattering channel, a small portion of the wavepacket quantum tunnels into the tetraquark well forming a long-lived tetraquark state. In the left hand plot we present the real time results for $P_K(i)$ of a meson collision. Here we see that while the majority of the incoming meson wavepackets are reflected, some tunnel into the tetraquark well and persist for long times. In the right hand plot we explicitly show the probability of a tetraquark forming by presenting $P_{TQ}(i)$ for the same collision event.

Tetraquark Decay

Similar to Gamow's theory of α-particle decay, we can utilize a WKB approximation to calculate the transmission probability of a tetraquark through the potential barrier. We note that our lattice calculation with a rapidly changing potential is beyond the strict range of applicability of any semi-classical approximation. Nonetheless, we will show decent agreement with our numerical calculations which corroborates the use of spin chain simulators of small size for probing confinement physics.

Here we derive transmission probability of a meson through a potential barrier of $V(n)$ for a Hamiltonian of the form of Eq. 7.9 with $k = 0$ given by

$$H = \sum_n \Big[J_n \big[\left|n+1\right\rangle \left\langle n\right| + \left|n\right\rangle \left\langle n+1\right| \big] + V(n) \left|n\right\rangle \left\langle n\right| \Big], \tag{7.11}$$

where J_n is the site dependent hopping strength. We use the WKB approximation, $\psi(n) = Ne^{\phi(n)}$, in which ϕ is a complex function and N is a normalization constant. This leads to the eigenvalue equation

$$Ee^{\phi(n)} = J_n e^{\phi(n+1)} + J_{n-1} e^{\phi(n-1)} + V(n) e^{\phi(n)}. \tag{7.12}$$

We make the approximation that $e^{i\phi(n+dx)} \sim e^{\phi(n)+dn\phi'(n)}$ such that $dn = 1$ leading to

$$E = J_n e^{\phi'(n)} + J_{n-1} e^{-\phi'(n)} + V(n). \tag{7.13}$$

Given that $\phi(n)$ is smooth, we let $\phi(n) = \int^n q(\epsilon) d\epsilon$. Now

$$(V(n) - E) + J_n e^{q(n)} + J_{n-1} e^{-q(n)} = 0. \tag{7.14}$$

We can solve this quadratic equation in $e^{q(n)}$ to obtain

$$q_\pm(n) = \ln \left[\frac{-(V(n) - E) \pm \sqrt{(V(n) - E)^2 - 4J_n J_{n-1}}}{2J_n} \right]. \tag{7.15}$$

It turns out that $q_+ \sim -q_-$ away from the potential barrier, thus, we can think of q_+ as a particle travelling to the right and $q-$ as a particle travelling to the left. Therefore, given that ψ_1 is the

wavefunction in the potential well, ψ_2 is the wavefunction in the classically forbidden region and ψ_3 is the wavefunction after the potential wall we set up the problem as

$$\begin{aligned}\psi_1(n) &= e^{\int_{n_0}^{n} q_+(x)dx} + Re^{\int_{n_0}^{n} q_-(x)dx},\\ \psi_2(n) &= Ae^{\int_{a}^{n} q_+(x)dx} + Be^{\int_{a}^{n} q_-(x)dx},\\ \psi_3(n) &= Te^{\int_{b}^{n} q_+(x)dx},\end{aligned} \tag{7.16}$$

where R is the reflection coefficient, T is the transmission coefficient and $n = a$ and $n = b$ are the classical turning points.

Physically these are interpreted as ψ_1: a particle in the well approaching the potential and a reflection term from a collision with the potential, ψ_2: a general solution to the eigenfunction problem above and ψ_3: the transmitted particle. We then use the standard procedure that $\psi_1(a) = \psi_2(a)$, $\psi_1'(a) = \psi_2'(a)$, $\psi_2(b) = \psi_3(b)$ and $\psi_2'(b) = \psi_3'(b)$ to solve for T:

$$T = \frac{e^{\int_{n_0}^{a} q_-(x)dx} e^{\int_{a}^{b} q_+(x)dx} (q_-^L(a) - q_+^L(a))}{(q_-(a) - q_+^L(a))}, \tag{7.17}$$

where the superscript 'L' indicates if the value of $q_\pm$ should be evaluated as the left hand limit of the potential at the discontinuity, $n = a$. Given that $q_-(x)$ is purely imaginary over the interval $n_0 < n < a$ and the transmission probability is given by $|T|^2$, we have that the exponential factor of the transmission probability is

$$|T|^2 \propto e^{2\int_{a}^{b} Re[q_+(x)]dx}. \tag{7.18}$$

One can estimate the probability of emission at any given time by $\frac{2x_1}{v}T$ in which v is the average velocity of the boundstate. Due to the exponential nature of T it gives the dominating contribution to the lifetime τ, which can be predicted within the WKB theory as

$$\ln(\tau) \sim C + 2\int_{x_0}^{x_1} q(x)dx, \tag{7.19}$$

with a constant C [155]. In Fig. 7.9(b) we show that by fitting the constant C, we see a remarkably good agreement between the WKB theory calculations of the lifetime of tetraquarks and those

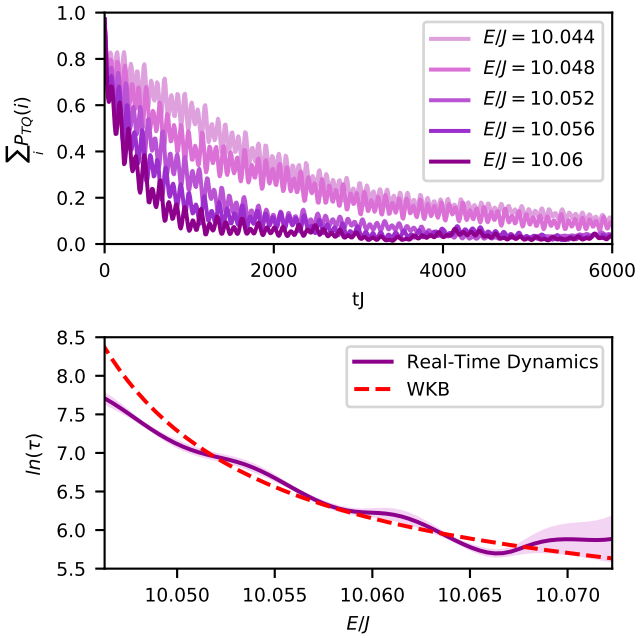

Figure 7.9: The lifetime of tetraquarks vary as a function of their energy. (a) The decay of tetraquarks for various initial energies. Here, the Hamiltonian parameters are $L = 40$, $\alpha = 2.6$ and $h = 0.1$. (b) A comparison of the relationship of the natural logarithm of lifetime, $\ln(\tau)$, of a tetraquark, calculated from the real time simulations as well as the WKB approximation as a function of the initial energy. The WKB approximation agrees well with the lifetimes observed in the real-time dynamics.

extracted from the numerical simulations up to the limit of a deep tetraquark well, $\frac{E}{J} < 10.045$.

7.4.3 Inducing Fusion Events for Larger Mesons

In this section we would like to confirm that our dynamical protocols enabling fusion events in meson collisions is not exclusive for $1-$mesons. One could argue that $1-$mesons are special because they do not have any internal dynamics and are simply equivalent to magnon spin flips. Here, we repeat both the abrupt change in the transverse field as well as the local alteration of the long-range interactions in the Hamiltonian for initial wavepackets composed of $2-$mesons. Fig. 7.10 shows the results which are very similar to the 1-meson collisions shown in the above sections. In these we clearly see that the protocols outlined in this work are not unique to $1-$mesons. The case of the abrupt change in the transverse field also results in continued oscillations localized for a long time around the scattering region for larger mesons. In the case of the induced tetraquark potential well we again see a long lived metastable tetraquark formed during the collision.

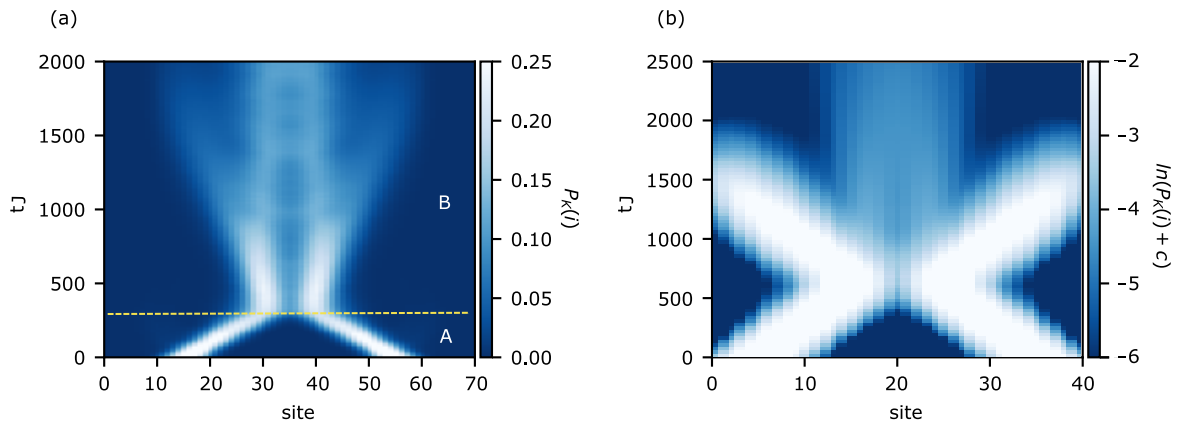

Figure 7.10: The dynamical formation of a tetraquark from a collision of 2-mesons. (a) Using an abrupt change of the transverse magnetic field at $tJ = 300$. Here, the Hamiltonian parameters are $\alpha = 2.6$, $h = 0.175$ in region A and $h = 0.1$ in region B. Similar results as in Fig. 7.6 are observable except that the oscillations of the tetraquark formed have a larger amplitude as well as slower frequencies, which is expected for a tetraquark formed from mesons with larger masses and non-trivial internal dynamics. (b) Performing a local alteration of the long-range interactions consisting of two terms of the form 7.10 with $d = 4$ and $d = 5$. Here, the Hamiltonian parameters are $\alpha = 2.6$, $h = 0.1$. We clearly see that in the collision a long lived metastable tetraquark is formed for $2-$mesons.

7.5 Experimental Feasibility

A physical realization of our meson scattering protocols requires the implementation of the one dimensional TFIM with power-law interactions as described by Eq. 3.17. Although there are several platforms available for the experimental realization of long-range Ising models with hundreds of spins e.g. with polar molecules [156, 157], trapped ions [158] and Rydberg atoms [159, 160, 161, 162], they are often realized in higher dimensional lattices. However for one dimensional systems, the number of spins available for quantum simulation range from 3-53 for ions trapped in a Paul trap [163, 164, 165, 166] or 20-51 in the case of a trapped array of Rydberg atoms in optical tweezers [167, 168], thus reaching the necessary system sizes for our scattering protocols.

In these setups, the many-body state with all spins down can be naturally realised. Then the initial state preparation of a pair of mesons (domains) located far apart from each other can be achieved through local quenches with help of lasers by performing flips on one or more spins at appropriate sites. The lattice spacing and the width of the laser beam determines the size of the domains which has been demonstrated both for trapped ions [169, 170, 171] and Rydberg atoms [167, 172, 168]. For initial states to propagate along the spin chain with well defined momentum, controlled nearest

neighbour spin exchange is required. For trapped ions, spin exchange between sites is engineered using Mølmer-Sørenson type protocols [169]. Effective transitions between $|\uparrow\rangle$ and $|\downarrow\rangle$ are driven with the help of a bichromatic laser with frequencies $\omega_{\pm} = \omega_0 \pm \Delta$ that shines upon the ion array, where Δ is the detuning of the laser field from the transition frequency ω_0 of the atomic transition $|\uparrow\rangle \leftrightarrow |\downarrow\rangle$. For Rydberg systems, the spin exchanges are achieved either by resonant dipole-dipole interactions or by off-diagonal van der Waals flip-flop interactions between Rydberg states [173]. In some cases, spin-exchange can also be induced via the standard van der Waals interaction [174].

Apart from the natural scattering dynamics of the mesons, we have proposed two other effective routes for the dynamical formation of tetraquarks: (i) by abruptly changing the kinetic energy as depicted in Fig. 7.6, and by (ii) fusion of mesons induced via a potential well as shown in Fig. 7.8(a). Method (i) can be implemented by abruptly changing the time dependent transverse field. Such type of quench dynamics are commonly executed in both systems, trapped ions [175, 120] as well as Rydberg atoms [176, 177]. An advantage of trapped ions is that one can easily tune the strength of the long-range interactions ($1 < \alpha < 3$) in the Ising model with the help of Raman lasers as recently demonstrated in the investigation of domain-wall dynamics [120].

However, the approach (ii) requires a non-trivial modification of the spin-spin interactions to a non-monotonic long-range form. Such exotic potentials may not be obvious for trapped ions, but in the following we sketch how they can be implemented using the highly tunable effective interactions of laser-dressed Rydberg atoms [178, 179, 180, 181]. A dressed Rydberg atom is primarily a ground state atom that is weakly superposed with an excited state corresponding to a large principal quantum number ($n \sim 20 - 100$) [182]. The amount and type of the Rydberg character in the dressed superposition state is controlled using dressing lasers that eventually determine the strength and shape of the effective potential [183, 184]. Recent experimental validations of Rydberg-dressed interactions include the measurement of pairwise interaction between two atoms [185], many-body Ising interactions [186, 187], as well as distance selective interactions [188].

The key idea for our modified long-range interactions is to construct a spin-1/2 state using two long-lived states ($|g_{\pm}\rangle$) of an atom which can either be a pair of hyperfine ground states or a ground state and a meta-stable state found in alkaline-earth atoms [184]. A pair of lasers (left and right

circularly polarized with phases set to zero without loss of generality) drive the atoms from $|g_\pm\rangle$ states to Rydberg states $|e_\pm\rangle$ off-resonantly with detunings $\Delta_\pm$ and Rabi frequencies $\Omega_\pm$. The full Hamiltonian in the atomic basis is $H = \sum_i (H_i^{\mathrm{A}} + H_i^{\mathrm{L}}) + \sum_{i<j} H_{ij}^{\mathrm{vdW}}$, where the individual terms are the following

$$H_i^{\mathrm{A}} = -\Delta_+ |e_+\rangle_i \langle e_+| - \Delta_- |e_-\rangle_i \langle e_-| , \tag{7.20}$$

$$H_i^{\mathrm{L}} = \frac{\Omega_+}{2} |g_-\rangle_i \langle e_+| + \frac{\Omega_-}{2} |g_+\rangle_i \langle e_-| , \tag{7.21}$$

$$H_{ij}^{\mathrm{vdW}} = V(\mathbf{r}_{ij}) |e_\alpha\rangle_i \langle e_\alpha| \otimes |e_{\alpha'}\rangle_j \langle e_{\alpha'}| , \tag{7.22}$$

where $V(\mathbf{r}_{ij}) = C_6(\theta,\phi)/r_{ij}^6$ is the van der Waals interaction between Rydberg atoms located at sites i and j and $\alpha, \alpha' \in \{\pm\}$.The effective spin-spin interactions between two atoms can then be obtained with respect to their ground states in the weak coupling limit $\Omega_\pm \ll E_{\alpha,\alpha'}$, where $E_{\alpha,\alpha'}$ are the eigenenergies of the relevant atomic systems, $H_i^{\mathrm{A}} + H_j^{\mathrm{A}} + H_{ij}^{\mathrm{vdW}}$. Using perturbation theory, one derives the effective interactions between the ground states which are expressed in the two-atom basis as follows,

$$H_{\mathrm{eff}} = \sum_{\substack{\alpha,\beta \\ \alpha',\beta'}} \tilde{V}_{\alpha',\beta'}^{\alpha,\beta}(\Omega_\pm, \Delta_\pm, V(\mathbf{r}_{ij})) |g_\alpha g_\beta\rangle_{ij} \langle g_{\alpha'} g_{\beta'}| . \tag{7.23}$$

The second order terms in the perturbation theory correspond to light shifts which serve as longitudinal fields for the spin Hamiltonian, while the fourth order terms provide the Ising interaction and transverse field term. The anisotropy in the van der Waals interaction depends on the magnetic quantum numbers and the relative angles (θ, ϕ) between the atoms with respect to the laser.

Overall, our main point is that there is sufficient tunability of the spatial interaction profile in order to engineer a local minimum of the effective interaction similar to the one of Fig. 7.8. However, while this effective modified potential between mesons can be achieved through the van der Waals interactions, its asymptotic decay $1/r_{ij}^6$ is not enough to ensure the stability of individual meson states. In order to stabilise them one can exploit the long-range dipole-dipole interactions which is also present. For this purpose, one then needs to consider both levels of the two-level system as Rydberg states for which boundstates have indeed been shown to exist [189]. Alternatively, switching on a weak longitudinal field would also ensure the formation of individual meson states while their

mutual interaction would be governed by the longer range potential discussed above.

A detailed quantitative modeling of experimental protocols is beyond the scope of this work, however we provide here some estimate for coherence times. In the case of Rydberg-dressed setups, the typical values of Rabi frequencies are in the range of tens of kHz to few MHz while the detunings are an order of magnitude larger. Rydberg states ranging from $n = 50 - 70$ for Rb atoms will have bare lifetimes around $80 - 130\mu$s [190]. However as a result of the weak coupling to Rydberg states, the lifetime of the effective two-level system is extended to milliseconds [188]. For such Rydberg states, the interactions are in the order of GHz [190] and thus for lattice spacings of 0.5-1.5 μm, one can simulate effective spin-spin interactions which are in the order of few kHz [186] to hundreds of kHz [185]. Assuming $J = 800$ kHz and the time of scattering occurring at $tJ = 100$ (after optimization of the protocol dynamics), coherence times of 0.125 ms are well within the reach of many-body Rydberg-dressed state lifetimes [188]. Although the dynamical timescales shown in this theoretical work are beyond what has been observed in experiments previously, the use of quantum optimal control theory [191, 192, 193] to reduce these timescales is promising especially with the access to a variety of control parameters such as maximising transverse field h while maintaining the domain-wall approximation, minimising the initial meson separation, tuning the initial meson size and exponent α. Indeed achieving the dynamical timescales and coherence times needed for this work is a challenge for future experiments.

Chapter 8

Conclusion

8.1 Summary of Thesis Achievements

This thesis presents results that further our understanding of quantum simulation, both in practical computation using a NISQ device (quantum simulation of confinement dynamics, Chapter 4 and error mitigation, Chapter 5) as well as paving the way for future simulation attempts (impurity states, Chapter 6 and dynamical hadron formation, Chapter 7).

In Chapter 4 we established that current IBM digital quantum computers are able to simulate non-perturbative quantum effects like confinement. Using a carefully designed quench setup has allowed us to show confinement signatures and the formation of domain-wall boundstates, deemed mesons, in the paradigmatic TFIM with a longitudinal field. Randomized measurement protocols have enabled us to show the confinement-induced slow-down of entanglement spreading on a digital quantum computer.

We propose an error mitigation technique in Chapter 5 that is simple to implement but also retains the mathematical rigour of more complicated techniques. This protocol is directly applicable to any quantum simulation whose measurements are basic expectation values of local observables. Furthermore, although our error mitigation method may not replace full state tomography, we expect it to be useful in measuring more complicated quantities beyond simple observables. With this error mitigation protocol we were able obtain quantitative results for confinement and entanglement dynamics of a

quantum spin chain which were previously unobtainable. We have been able to extract the first meson masses of confinement induced boundstates and observed the corresponding halting of entanglement spreading. In general, this simple error mitigation enables us to exploit available NISQ devices for their applications with significantly reduced errors.

In Chapter 6 we demonstrated the creation of exotic and long-lived composite particles from the interplay of confinement and impurity dynamics. We quantitatively framed the problem within a simple semiclassical picture and described quantum corrections by semiclassically quantizing the metastable boundstate eigenenergies. Our predictions should be readily observable in state-of-the-art quantum simulators, where defects can be easily engineered [170, 194].

Finally, in Chapter 7 we showed that confinement-induced boundstates of many elementary domain-wall excitations exist in the long-range Ising model akin to composite hadronic particles in QCD. We studied the collision of simple two-particle mesonic boundstates and found signatures of the dynamical formation of metastable four-domain-wall states in analogy to tetraquarks. However, natural meson collisions are mainly elastic and the signal for natural hadron formation is weak. Therefore, we proposed two alternative protocols to induce dynamical fusion events in the long-range Ising model that are much more controllable and allow for an unambiguous detection of dynamical hadron formation. Finally, we argued that all three of these methods, while challenging, are in principle realisable with current quantum simulator setups. In particular, we sketched the experimental requirements for initial state preparation as well as the use of laser-dressed Rydberg atoms for engineering the modified long-range interactions.

8.2 Future Work

Overall, the work presented in this thesis both benchmarks the capabilities of current digital quantum computers and builds on the useful software available. Furthermore, possible future directions for quantum simulation efforts are outlined that are one step closer to full simulations of confinement dynamics previously unachievable with a classical device. This thesis opens up many interesting questions for future research. In the following, two possible directions are briefly introduced; one

that builds upon the theoretical phenomena that are considered previously and one that considers improvements of quantum simulation methods.

8.2.1 Dynamical Hadron Formation in the Lattice Schwinger Model

A next step towards the long-term goal of understanding fusion events in the full SU(3) gauge theory of QCD would be the quantum simulation of scattering events with dynamical hadron formation in simplified lattice gauge theories (LGTs). For example, one dimensional versions of U(1) LGTs have been studied intensively in the past years with many connections to quantum simulation architectures [195, 170]. A prime candidate would be the Schwinger model in which confinement dynamics can be studied efficiently with time-dependent density-matrix renormalization group methods [13]. This Hamiltonian can be directly mapped to a spin model via the use of the Jordan Wigner transformation in which an excitation on the odd sites corresponds to a quark and an excitation on the even sites represents an anti-quark. In fact, scattering events in this model are considered in Ref. [196] in which it is shown that two colliding Schwinger bosons with high enough momentum can produce two boundstates, each of which contain two Schwinger bosons themselves. Thus, in principle such fusion events are theoretically possible.

8.2.2 Scalable Error Mitigation

The computational overhead of implementing the error mitigation protocol in Chapter 5 is dominated by the cost of evaluating the purity, $\mathrm{Tr}(\rho^2)$, on the quantum device. The number of corresponding measurements is $N_u N_m$ where N_u is the number of randomised unitaries and N_m is the number of random measurements. Within the randomised scheme of Ref. [125], for a given error level, this grows exponentially with the system size [53], which poses a potential problem for large quantum computers.

Given a local observable, this scalability issue could be elevated by considering the purity of a 'patch' around the sites being measured, i.e., a subsystem A that contains the qubits to be measured. By extension of the global depolarising error approximation we can make the assumption that the reduced

density matrix on the subsystem A is

$$\rho_A = p\,\mathrm{Tr}_{j\notin A}(|\psi\rangle\langle\psi|) + (1-p)\frac{\mathcal{I}}{2^{|A|}}, \tag{8.1}$$

where $|\psi\rangle$ is the quantum state prepared on the quantum device, $|A|$ is the cardinality of the patch A and $\mathcal{I}$ is the identity of size $|A| \times |A|$. The purity of this patch is thus

$$Tr(\rho_A^2) = p^2 Tr(\rho_{A,exact}^2) + \frac{(1-p)^2}{2^{|A|}} + \frac{p(1-p)}{2^{|A|-1}}. \tag{8.2}$$

Given knowledge of $Tr(\rho_{A,exact}^2)$ we are able to extract out the probability of error on this patch p. After p is known the rest of the mitigation protocol is equivalent to before. In general the calculation of $Tr(\rho_{A,exact}^2)$ is just as difficult as calculating the full density matrix of the system. However, if the quantum circuit in use is general enough to be tuned to the time dynamics of a well studied quantum system - this is typically the case for deep circuits - we are able to use universal results for Rényi entropy growth to extract p, for example in the TFIM [197]. Here, we are making the assumption that the error is a function of the gates in the quantum circuit not the parameterisations of the gates themselves. This method would allow error mitigation for local observables in a scalable manner that will be useful even after NISQ devices have achieved quantum advantage.

Bibliography

[1] J. Vovrosh and J. Knolle, "Confinement and entanglement dynamics on a digital quantum computer," *Scientific Reports*, vol. 11, p. 11577, Jun 2021.

[2] J. Vovrosh, H. Zhao, J. Knolle, and A. Bastianello, "Confinement-induced impurity states in spin chains," *Phys. Rev. B*, vol. 105, p. L100301, Mar 2022.

[3] J. Vovrosh, K. E. Khosla, S. Greenaway, C. Self, M. S. Kim, and J. Knolle, "Simple mitigation of global depolarizing errors in quantum simulations," *Phys. Rev. E*, vol. 104, p. 035309, Sep 2021.

[4] J. Vovrosh, R. Mukherjee, A. Bastianello, and J. Knolle, "Dynamical hadron formation in long-range interacting quantum spin chains," *arXiv preprint 2204.05641*, Apr 2022.

[5] H. Zhao, J. Vovrosh, F. Mintert, and J. Knolle, "Quantum many-body scars in optical lattices," *Phys. Rev. Lett.*, vol. 124, p. 160604, Apr 2020.

[6] D. Landau and K. Binder, *A guide to Monte Carlo simulations in statistical physics*. Cambridge university press, 2021.

[7] M. Troyer and U.-J. Wiese, "Computational complexity and fundamental limitations to fermionic quantum monte carlo simulations," *Phys. Rev. Lett.*, vol. 94, may 2005.

[8] U. Schollwöck, "The density-matrix renormalization group," *Reviews of Modern Physics*, vol. 77, pp. 259–315, Apr 2005.

[9] C. M. Institute, "Yang–mills and mass gap." https://www.claymath.org/millennium-problems/yang-mills-and-mass-gap, 2022. [Online; accessed 21-July-2022].

[10] B. M. McCoy and T. T. Wu, "Two-dimensional ising field theory in a magnetic field: Breakup of the cut in the two-point function," *Phys. Rev. D*, vol. 18, pp. 1259–1267, Aug 1978.

[11] P. Fonseca and A. Zamolodchikov, "Ising field theory in a magnetic field: Analytic properties of the free energy," *Journal of Statistical Physics*, vol. 110, pp. 527–590, Mar 2003.

[12] F. Liu, R. Lundgren, P. Titum, G. Pagano, J. Zhang, C. Monroe, and A. V. Gorshkov, "Confined quasiparticle dynamics in long-range interacting quantum spin chains," *Phys. Rev. Lett.*, vol. 122, p. 150601, Apr 2019.

[13] G. Magnifico, M. Dalmonte, P. Facchi, S. Pascazio, F. V. Pepe, and E. Ercolessi, "Real time dynamics and confinement in the $\mathbb{Z}_n$ schwinger-weyl lattice model for $1 + 1$ qed," *Quantum*, vol. 4, p. 281, Jun 2020.

[14] K. D. Raedt, K. Michielsen, H. D. Raedt, B. Trieu, G. Arnold, M. Richter, T. Lippert, H. Watanabe, and N. Ito, "Massively parallel quantum computer simulator," *Computer Physics Communications*, vol. 176, pp. 121–136, jan 2007.

[15] R. P. Feynman, "Simulating physics with computers," *International journal of theoretical physics*, vol. 21, no. 6, pp. 467–488, 1982.

[16] C. Gross and I. Bloch, "Quantum simulations with ultracold atoms in optical lattices," *Science*, vol. 357, pp. 995–1001, Sep 2017.

[17] I. Bloch, J. Dalibard, and W. Zwerger, "Many-body physics with ultracold gases," *Rev. Mod. Phys.*, vol. 80, pp. 885–964, Jul 2008.

[18] D. Jaksch and P. Zoller, "The cold atom hubbard toolbox," *Annals of Physics*, vol. 315, pp. 52–79, Jan 2005.

[19] A. Polkovnikov, K. Sengupta, A. Silva, and M. Vengalattore, "Colloquium: Nonequilibrium dynamics of closed interacting quantum systems," *Rev. Mod. Phys.*, vol. 83, pp. 863–883, Aug 2011.

[20] J. yoon Choi, S. Hild, J. Zeiher, P. Schauß, A. Rubio-Abadal, T. Yefsah, V. Khemani, D. A. Huse, I. Bloch, and C. Gross, "Exploring the many-body localization transition in two dimensions," *Science*, vol. 352, pp. 1547–1552, Jun 2016.

[21] J. Simon, W. S. Bakr, R. Ma, M. E. Tai, P. M. Preiss, and M. Greiner, "Quantum simulation of antiferromagnetic spin chains in an optical lattice," *Nature*, vol. 472, pp. 307–312, Apr 2011.

[22] C. H. Bennett, "Logical reversibility of computation," *IBM Journal of Research and Development*, vol. 17, pp. 525–532, Nov 1973.

[23] H. K. Büning and T. Lettmann, *Propositional logic: deduction and algorithms*, vol. 48. Cambridge University Press, Aug 1999.

[24] A. Y. Kitaev, "Quantum computations: algorithms and error correction," *Russian Mathematical Surveys*, vol. 52, pp. 1191–1249, dec 1997.

[25] A. Montanaro, "Quantum algorithms: an overview," *npj Quantum Information*, vol. 2, Jan 2016.

[26] A. Y. Kitaev, "Quantum measurements and the abelian stabilizer problem," *arXiv preprint quant-ph/9511026*, Nov 1995.

[27] M. A. Nielsen and I. Chuang, "Quantum computation and quantum information," 2002.

[28] L. Hales and S. Hallgren, "An improved quantum fourier transform algorithm and applications," in *Proceedings 41st Annual Symposium on Foundations of Computer Science*, pp. 515–525, Aug 2000.

[29] P. Shor, "Algorithms for quantum computation: discrete logarithms and factoring," in *Proceedings 35th Annual Symposium on Foundations of Computer Science*, pp. 124–134, Aug 1994.

[30] V. Bhatia and K. Ramkumar, "An efficient quantum computing technique for cracking rsa using shor's algorithm," in *2020 IEEE 5th International Conference on Computing Communication and Automation (ICCCA)*, pp. 89–94, Nov 2020.

[31] A. Peruzzo, J. McClean, P. Shadbolt, M.-H. Yung, X.-Q. Zhou, P. J. Love, A. Aspuru-Guzik, and J. L. O'Brien, "A variational eigenvalue solver on a photonic quantum processor," *Nat. Com.*, vol. 5, Jul 2014.

[32] J. Romero, R. Babbush, J. R. McClean, C. Hempel, P. Love, and A. Aspuru-Guzik, "Strategies for quantum computing molecular energies using the unitary coupled cluster ansatz," *arXiv preprint 1701.02691*, Feb 2018.

[33] J. R. McClean, J. Romero, R. Babbush, and A. Aspuru-Guzik, "The theory of variational hybrid quantum-classical algorithms," *New Journal of Physics*, vol. 18, p. 023023, Feb 2016.

[34] G. E. Crooks, "Gradients of parameterized quantum gates using the parameter-shift rule and gate decomposition," *arXiv preprint 1905.13311*, May 2019.

[35] L. M. Sieberer, T. Olsacher, A. Elben, M. Heyl, P. Hauke, F. Haake, and P. Zoller, "Digital quantum simulation, trotter errors, and quantum chaos of the kicked top," *npj Quantum Information*, vol. 5, Sep 2019.

[36] M. Heyl, P. Hauke, and P. Zoller, "Quantum localization bounds trotter errors in digital quantum simulation," *Science Advances*, vol. 5, Apr 2019.

[37] W. Rossmann, *Lie groups: an introduction through linear groups*, vol. 5. Oxford University Press on Demand, 2006.

[38] M. Suzuki, "Decomposition formulas of exponential operators and lie exponentials with some applications to quantum mechanics and statistical physics," *Journal of mathematical physics*, vol. 26, no. 4, pp. 601–612, 1985.

[39] F. Vatan and C. Williams, "Optimal quantum circuits for general two-qubit gates," *Phys. Rev. A*, vol. 69, p. 032315, Mar 2004.

[40] L. Herviou, S. Bera, and J. H. Bardarson, "Multiscale entanglement clusters at the many-body localization phase transition," *Phys. Rev. B*, vol. 99, Apr 2019.

[41] V. Shende, S. Bullock, and I. Markov, "Synthesis of quantum-logic circuits," *IEEE Transactions on Computer-Aided Design of Integrated Circuits and Systems*, vol. 25, pp. 1000–1010, Jun 2006.

[42] F. Vatan and C. P. Williams, "Realization of a general three-qubit quantum gate," *arXiv preprint quant-ph/0401178*, Jan 2004.

[43] A. S. Holevo, "Bounds for the quantity of information transmitted by a quantum communication channel," *Problemy Peredachi Informatsii*, vol. 9, no. 3, pp. 3–11, 1973.

[44] A. Elben, S. T. Flammia, H.-Y. Huang, R. Kueng, J. Preskill, B. Vermersch, and P. Zoller, "The randomized measurement toolbox," *arXiv preprint 2203.11374*, Mar 2022.

[45] A. Elben, J. Yu, G. Zhu, M. Hafezi, F. Pollmann, P. Zoller, and B. Vermersch, "Many-body topological invariants from randomized measurements in synthetic quantum matter," *Science advances*, vol. 6, no. 15, 2020.

[46] B. Vermersch, A. Elben, L. M. Sieberer, N. Y. Yao, and P. Zoller, "Probing scrambling using statistical correlations between randomized measurements," *Phys. Rev. X*, vol. 9, p. 021061, Jun 2019.

[47] H.-Y. Huang, R. Kueng, G. Torlai, V. V. Albert, and J. Preskill, "Provably efficient machine learning for quantum many-body problems," *arXiv preprint 2106.12627*, Feb 2022.

[48] P. Calabrese and J. Cardy, "Evolution of entanglement entropy in one-dimensional systems," *Journal of Statistical Mechanics: Theory and Experiment*, vol. 2005, p. P04010, Apr 2005.

[49] D. M. Basko, I. L. Aleiner, and B. L. Altshuler, "On the problem of many-body localization," *arXiv preprint cond-mat/0602510*, Feb 2006.

[50] D. A. Abanin, E. Altman, I. Bloch, and M. Serbyn, "Colloquium: Many-body localization, thermalization, and entanglement," *Reviews of Modern Physics*, vol. 91, may 2019.

[51] G. Vidal, "Efficient classical simulation of slightly entangled quantum computations," *Phys. Rev. Lett.*, vol. 91, p. 147902, Oct 2003.

[52] B. Vermersch, A. Elben, M. Dalmonte, J. I. Cirac, and P. Zoller, "Unitary n-designs via random quenches in atomic hubbard and spin models: Application to the measurement of rényi entropies," *Phys. Rev. A*, vol. 97, p. 023604, Feb 2018.

[53] T. Brydges, A. Elben, P. Jurcevic, B. Vermersch, C. Maier, B. P. Lanyon, P. Zoller, R. Blatt, and C. F. Roos, "Probing rényi entanglement entropy via randomized measurements," *Science*, vol. 364, no. 6437, pp. 260–263, 2019.

[54] J. I. Cirac and P. Zoller, "Quantum computations with cold trapped ions," *Phys. Rev. Lett.*, vol. 74, pp. 4091–4094, May 1995.

[55] C. Monroe, D. M. Meekhof, B. E. King, W. M. Itano, and D. J. Wineland, "Demonstration of a fundamental quantum logic gate," *Phys. Rev. Lett.*, vol. 75, pp. 4714–4717, Dec 1995.

[56] "Ionq, https://ionq.com/," Sept 2022.

[57] "Quantinuum, https://www.quantinuum.com/," Sept 2022.

[58] "Orca computing, https://www.orcacomputing.com/," Sept 2022.

[59] "Pasqal, https://pasqal.io/," Sept 2022.

[60] "planqc, https://www.planqc.eu/," Sept 2022.

[61] "Google quantum ai, https://quantumai.google/," Sept 2022.

[62] "Ibm quantum, https://quantum-computing.ibm.com/," Sept 2022.

[63] "Rigetti computing, https://www.rigetti.com/," Sept 2022.

[64] "Intel - quantum computing, https://www.intel.com/content/www/us/en/research/quantum-computing.html," Sept 2022.

[65] A. J. Leggett, "Macroscopic Quantum Systems and the Quantum Theory of Measurement," *Progress of Theoretical Physics Supplement*, vol. 69, pp. 80–100, Mar 1980.

[66] J. Koch, T. M. Yu, J. Gambetta, A. A. Houck, D. I. Schuster, J. Majer, A. Blais, M. H. Devoret, S. M. Girvin, and R. J. Schoelkopf, "Charge-insensitive qubit design derived from the cooper pair box," *Phys. Rev. A*, vol. 76, oct 2007.

[67] "*ibmq_washington* v1.3.2, ibm quantum team. retrieved from https://quantum-computing.ibm.com, (2022)."

[68] "*ibmq_nairobi* v1.0.24, ibm quantum team. retrieved from https://quantum-computing.ibm.com, (2022)."

[69] R. W. Hamming, "Error detecting and error correcting codes," *The Bell System Technical Journal*, vol. 29, no. 2, pp. 147–160, 1950.

[70] W. K. Wootters and W. H. Zurek, "A single quantum cannot be cloned," *Nature*, vol. 299, no. 5886, pp. 802–803, 1982.

[71] D. Dieks, "Communication by epr devices," *Physics Letters A*, vol. 92, no. 6, pp. 271–272, 1982.

[72] A. Peres, "Reversible logic and quantum computers," *Phys. Rev. A*, vol. 32, pp. 3266–3276, Dec 1985.

[73] S. J. Devitt, W. J. Munro, and K. Nemoto, "Quantum error correction for beginners," *Reports on Progress in Physics*, vol. 76, p. 076001, Jun 2013.

[74] S. Endo, S. C. Benjamin, and Y. Li, "Practical quantum error mitigation for near-future applications," *Phys. Rev. X*, vol. 8, p. 031027, Jul 2018.

[75] M. S. ANIS, Abby-Mitchell, H. Abraham, AduOffei, R. Agarwal, G. Agliardi, M. Aharoni, V. Ajith, I. Y. Akhalwaya, G. Aleksandrowicz, T. Alexander, M. Amy, S. Anagolum, Anthony-Gandon, E. Arbel, A. Asfaw, A. Athalye, A. Avkhadiev, C. Azaustre, P. BHOLE, A. Banerjee, S. Banerjee, W. Bang, A. Bansal, P. Barkoutsos, A. Barnawal, G. Barron, G. S. Barron, L. Bello, Y. Ben-Haim, M. C. Bennett, D. Bevenius, D. Bhatnagar, P. Bhatnagar, A. Bhobe, P. Bianchini, L. S. Bishop, C. Blank, S. Bolos, S. Bopardikar, S. Bosch, S. Brandhofer, Brandon, S. Bravyi, N. Bronn, Bryce-Fuller, D. Bucher, A. Burov, F. Cabrera, P. Calpin, L. Capelluto, J. Carballo, G. Carrascal, A. Carriker, I. Carvalho, A. Chen, C.-F. Chen, E. Chen, J. C. Chen, R. Chen, F. Chevallier, K. Chinda, R. Cholarajan, J. M. Chow, S. Churchill, CisterMoke, C. Claus, C. Clauss, C. Clothier, R. Cocking, R. Cocuzzo, J. Connor, F. Correa,

Z. Crockett, A. J. Cross, A. W. Cross, S. Cross, J. Cruz-Benito, C. Culver, A. D. Córcoles-Gonzales, N. D, S. Dague, T. E. Dandachi, A. N. Dangwal, J. Daniel, M. Daniels, M. Dartiailh, A. R. Davila, F. Debouni, A. Dekusar, A. Deshmukh, M. Deshpande, D. Ding, J. Doi, E. M. Dow, P. Downing, E. Drechsler, E. Dumitrescu, K. Dumon, I. Duran, K. EL-Safty, E. Eastman, G. Eberle, A. Ebrahimi, P. Eendebak, D. Egger, ElePT, Emilio, A. Espiricueta, M. Everitt, D. Facoetti, Farida, P. M. Fernández, S. Ferracin, D. Ferrari, A. H. Ferrera, R. Fouilland, A. Frisch, A. Fuhrer, B. Fuller, M. GEORGE, J. Gacon, B. G. Gago, C. Gambella, J. M. Gambetta, A. Gammanpila, L. Garcia, T. Garg, S. Garion, J. R. Garrison, J. Garrison, T. Gates, H. Georgiev, L. Gil, A. Gilliam, A. Giridharan, Glen, J. Gomez-Mosquera, Gonzalo, S. de la Puente González, J. Gorzinski, I. Gould, D. Greenberg, D. Grinko, W. Guan, D. Guijo, Guillermo-Mijares-Vilarino, J. A. Gunnels, H. Gupta, N. Gupta, J. M. Günther, M. Haglund, I. Haide, I. Hamamura, O. C. Hamido, F. Harkins, K. Hartman, A. Hasan, V. Havlicek, J. Hellmers, Ł. Herok, S. Hillmich, C. Hong, H. Horii, C. Howington, S. Hu, W. Hu, C.-H. Huang, J. Huang, R. Huisman, H. Imai, T. Imamichi, K. Ishizaki, Ishwor, R. Iten, T. Itoko, A. Ivrii, A. Javadi, A. Javadi-Abhari, W. Javed, Q. Jianhua, M. Jivrajani, K. Johns, S. Johnstun, Jonathan-Shoemaker, JosDenmark, JoshDumo, J. Judge, T. Kachmann, A. Kale, N. Kanazawa, J. Kane, Kang-Bae, A. Kapila, A. Karazeev, P. Kassebaum, T. Kehrer, J. Kelso, S. Kelso, H. van Kemenade, V. Khanderao, S. King, Y. Kobayashi, Kovi11Day, A. Kovyrshin, R. Krishnakumar, P. Krishnamurthy, V. Krishnan, K. Krsulich, P. Kumkar, G. Kus, R. LaRose, E. Lacal, R. Lambert, H. Landa, J. Lapeyre, J. Latone, S. Lawrence, C. Lee, G. Li, T. J. Liang, J. Lishman, D. Liu, P. Liu, Lolcroc, A. K. M, L. Madden, Y. Maeng, S. Maheshkar, K. Majmudar, A. Malyshev, M. E. Mandouh, J. Manela, Manjula, J. Marecek, M. Marques, K. Marwaha, D. Maslov, P. Maszota, D. Mathews, A. Matsuo, F. Mazhandu, D. McClure, M. McElaney, C. McGarry, D. McKay, D. McPherson, S. Meesala, D. Meirom, C. Mendell, T. Metcalfe, M. Mevissen, A. Meyer, A. Mezzacapo, R. Midha, D. Miller, H. Miller, Z. Minev, A. Mitchell, N. Moll, A. Montanez, G. Monteiro, M. D. Mooring, R. Morales, N. Moran, D. Morcuende, S. Mostafa, M. Motta, R. Moyard, P. Murali, D. Murata, J. Müggenburg, T. NEMOZ, D. Nadlinger, K. Nakanishi, G. Nannicini, P. Nation, E. Navarro, Y. Naveh, S. W. Neagle, P. Neuweiler, A. Ngoueya, T. Nguyen, J. Nicander, Nick-Singstock, P. Niroula,

H. Norlen, NuoWenLei, L. J. O'Riordan, O. Ogunbayo, P. Ollitrault, T. Onodera, R. Otaolea, S. Oud, D. Padilha, H. Paik, S. Pal, Y. Pang, A. Panigrahi, V. R. Pascuzzi, S. Perriello, E. Peterson, A. Phan, K. Pilch, F. Piro, M. Pistoia, C. Piveteau, J. Plewa, P. Pocreau, A. Pozas-Kerstjens, R. Pracht, M. Prokop, V. Prutyanov, S. Puri, D. Puzzuoli, Pythonix, J. Pérez, Quant02, Quintiii, R. I. Rahman, A. Raja, R. Rajeev, I. Rajput, N. Ramagiri, A. Rao, R. Raymond, O. Reardon-Smith, R. M.-C. Redondo, M. Reuter, J. Rice, M. Riedemann, Rietesh, D. Risinger, P. Rivero, M. L. Rocca, D. M. Rodríguez, RohithKarur, B. Rosand, M. Rossmannek, M. Ryu, T. SAPV, N. R. C. Sa, A. Saha, A. Ash-Saki, S. Sanand, M. Sandberg, H. Sandesara, R. SApra, H. Sargsyan, A. Sarkar, N. Sathaye, N. Savola, B. Schmitt, C. Schnabel, Z. Schoenfeld, T. L. Scholten, E. Schoute, M. Schulterbrandt, J. Schwarm, J. Seaward, Sergi, I. F. Sertage, K. Setia, F. Shah, N. Shammah, W. Shanks, R. Sharma, P. Shaw, Y. Shi, J. Shoemaker, A. Silva, A. Simonetto, D. Singh, D. Singh, P. Singh, P. Singkanipa, Y. Siraichi, Siri, J. Sistos, I. Sitdikov, S. Sivarajah, Slavikmew, M. B. Sletfjerding, J. A. Smolin, M. Soeken, I. O. Sokolov, I. Sokolov, V. P. Soloviev, SooluThomas, Starfish, D. Steenken, M. Stypulkoski, A. Suau, S. Sun, K. J. Sung, M. Suwama, O. Słowik, H. Takahashi, T. Takawale, I. Tavernelli, C. Taylor, P. Taylour, S. Thomas, K. Tian, M. Tillet, M. Tod, M. Tomasik, C. Tornow, E. de la Torre, J. L. S. Toural, K. Trabing, M. Treinish, D. Trenev, TrishaPe, F. Truger, G. Tsilimigkounakis, D. Tulsi, D. Tuna, W. Turner, Y. Vaknin, C. R. Valcarce, F. Varchon, A. Vartak, A. C. Vazquez, P. Vijaywargiya, V. Villar, B. Vishnu, D. Vogt-Lee, C. Vuillot, J. Weaver, J. Weidenfeller, R. Wieczorek, J. A. Wildstrom, J. Wilson, E. Winston, WinterSoldier, J. J. Woehr, S. Woerner, R. Woo, C. J. Wood, R. Wood, S. Wood, J. Wootton, M. Wright, L. Xing, J. YU, Yaiza, B. Yang, U. Yang, J. Yao, D. Yeralin, R. Yonekura, D. Yonge-Mallo, R. Yoshida, R. Young, J. Yu, L. Yu, Yuma-Nakamura, C. Zachow, L. Zdanski, H. Zhang, I. Zidaru, B. Zimmermann, C. Zoufal, aeddins ibm, alexzhang13, b63, bartek bartlomiej, bcamorrison, brandhsn, chetmurthy, deeplokhande, dekel.meirom, dime10, dlasecki, ehchen, ewinston, fanizzamarco, fs1132429, gadial, galeinston, georgezhou20, georgios ts, gruu, hhorii, hhyap, hykavitha, itoko, jeppevinkel, jessica angel7, jezerjojo14, jliu45, johannesgreiner, jscott2, kUmezawa, klinvill, krutik2966, ma5x, michelle4654, msuwama, nico lgrs, nrhawkins, ntgiwsvp, ordmoj, sagar pahwa, pritamsinha2304, rithikaadiga, ryancocuzzo, saktar unr, saswati qiskit, septembrr,

sethmerkel, sg495, shaashwat, smturro2, sternparky, strickroman, tigerjack, tsura crisaldo, upsideon, vadebayo49, welien, willhbang, wmurphy collabstar, yang.luh, and M. Čepulkovskis, "Qiskit: An open-source framework for quantum computing," 2021.

[76] M. S. Jattana, F. Jin, H. De Raedt, and K. Michielsen, "General error mitigation for quantum circuits," *Quantum Information Processing*, vol. 19, no. 11, pp. 1–17, 2020.

[77] F. B. Maciejewski, Z. Zimborás, and M. Oszmaniec, "Mitigation of readout noise in near-term quantum devices by classical post-processing based on detector tomography," *Quantum*, vol. 4, p. 257, 2020.

[78] S. Bravyi, S. Sheldon, A. Kandala, D. C. Mckay, and J. M. Gambetta, "Mitigating measurement errors in multiqubit experiments," *Phys. Rev. A*, vol. 103, p. 042605, Apr 2021.

[79] Y. Chen, M. Farahzad, S. Yoo, and T.-C. Wei, "Detector tomography on ibm quantum computers and mitigation of an imperfect measurement," *Phys. Rev. A*, vol. 100, no. 5, p. 052315, 2019.

[80] J. R. McClean, Z. Jiang, N. C. Rubin, R. Babbush, and H. Neven, "Decoding quantum errors with subspace expansions," *Nat. Com.*, vol. 11, no. 1, pp. 1–9, 2020.

[81] X. Bonet-Monroig, R. Sagastizabal, M. Singh, and T. O'Brien, "Low-cost error mitigation by symmetry verification," *Phys. Rev. A*, vol. 98, no. 6, p. 062339, 2018.

[82] R. Sagastizabal, X. Bonet-Monroig, M. Singh, M. A. Rol, C. Bultink, X. Fu, C. Price, V. Ostroukh, N. Muthusubramanian, A. Bruno, *et al.*, "Experimental error mitigation via symmetry verification in a variational quantum eigensolver," *Phys. Rev. A*, vol. 100, no. 1, p. 010302, 2019.

[83] M. C. Tran, Y. Su, D. Carney, and J. M. Taylor, "Faster digital quantum simulation by symmetry protection," *PRX Quantum*, vol. 2, p. 010323, Feb 2021.

[84] W. J. Huggins, J. R. McClean, N. C. Rubin, Z. Jiang, N. Wiebe, K. B. Whaley, and R. Babbush, "Efficient and noise resilient measurements for quantum chemistry on near-term quantum computers," *npj Quantum Information*, vol. 7, Feb 2021.

[85] S. McArdle, X. Yuan, and S. Benjamin, "Error-mitigated digital quantum simulation," *Phys. Rev. Lett.*, vol. 122, no. 18, p. 180501, 2019.

[86] E. F. Dumitrescu, A. J. McCaskey, G. Hagen, G. R. Jansen, T. D. Morris, T. Papenbrock, R. C. Pooser, D. J. Dean, and P. Lougovski, "Cloud quantum computing of an atomic nucleus," *Phys. Rev. Lett.*, vol. 120, no. 21, p. 210501, 2018.

[87] J. R. McClean, M. E. Kimchi-Schwartz, J. Carter, and W. A. De Jong, "Hybrid quantum-classical hierarchy for mitigation of decoherence and determination of excited states," *Phys. Rev. A*, vol. 95, no. 4, p. 042308, 2017.

[88] J. I. Colless, V. V. Ramasesh, D. Dahlen, M. S. Blok, M. Kimchi-Schwartz, J. McClean, J. Carter, W. De Jong, and I. Siddiqi, "Computation of molecular spectra on a quantum processor with an error-resilient algorithm," *Physical Review X*, vol. 8, no. 1, p. 011021, 2018.

[89] A. Kandala, K. Temme, A. D. Córcoles, A. Mezzacapo, J. M. Chow, and J. M. Gambetta, "Error mitigation extends the computational reach of a noisy quantum processor," *Nature*, vol. 567, no. 7749, pp. 491–495, 2019.

[90] M. Otten and S. K. Gray, "Accounting for errors in quantum algorithms via individual error reduction," *npj Quantum Information*, vol. 5, no. 1, pp. 1–6, 2019.

[91] M. Otten and S. K. Gray, "Recovering noise-free quantum observables," *Phys. Rev. A*, vol. 99, no. 1, p. 012338, 2019.

[92] A. Smith, M. Kim, F. Pollmann, and J. Knolle, "Simulating quantum many-body dynamics on a current digital quantum computer," *npj Quantum Information*, vol. 5, no. 106, 2019.

[93] A. Strikis, D. Qin, Y. Chen, S. C. Benjamin, and Y. Li, "Learning-based quantum error mitigation," *PRX Quantum*, vol. 2, p. 040330, Nov 2021.

[94] A. Zlokapa and A. Gheorghiu, "A deep learning model for noise prediction on near-term quantum devices," *arXiv preprint arXiv:2005.10811*, May 2020.

[95] P. Czarnik, A. Arrasmith, P. J. Coles, and L. Cincio, "Error mitigation with clifford quantum-circuit data," *Quantum*, vol. 5, p. 592, Nov 2021.

[96] A. Lowe, M. H. Gordon, P. Czarnik, A. Arrasmith, P. J. Coles, and L. Cincio, "Unified approach to data-driven quantum error mitigation," *Phys. Rev. Research*, vol. 3, p. 033098, Jul 2021.

[97] Y. Li and S. C. Benjamin, "Efficient variational quantum simulator incorporating active error minimization," *Physical Review X*, vol. 7, no. 2, p. 021050, 2017.

[98] S. Endo, S. C. Benjamin, and Y. Li, "Practical quantum error mitigation for near-future applications," *Physical Review X*, vol. 8, no. 3, p. 031027, 2018.

[99] K. Temme, S. Bravyi, and J. M. Gambetta, "Error mitigation for short-depth quantum circuits," *Phys. Rev. Lett.*, vol. 119, no. 18, p. 180509, 2017.

[100] E. Gustafson, Y. Meurice, and J. Unmuth-Yockey, "Quantum simulation of scattering in the quantum ising model," *Phys. Rev. D*, vol. 99, no. 9, p. 094503, 2019.

[101] T. Giurgica-Tiron, Y. Hindy, R. LaRose, A. Mari, and W. J. Zeng, "Digital zero noise extrapolation for quantum error mitigation," in *2020 IEEE International Conference on Quantum Computing and Engineering (QCE)*, pp. 306–316, 2020.

[102] Z. Cai, "Multi-exponential error extrapolation and combining error mitigation techniques for nisq applications," *npj Quantum Information*, vol. 7, no. 1, pp. 1–12, 2021.

[103] A. He, B. Nachman, W. A. de Jong, and C. W. Bauer, "Zero-noise extrapolation for quantum-gate error mitigation with identity insertions," *Phys. Rev. A*, vol. 102, p. 012426, Jul 2020.

[104] P. D. Nation, H. Kang, N. Sundaresan, and J. M. Gambetta, "Scalable mitigation of measurement errors on quantum computers," *PRX Quantum*, vol. 2, p. 040326, Nov 2021.

[105] A. W. R. Smith, K. E. Khosla, C. N. Self, and M. S. Kim, "Qubit readout error mitigation with bit-flip averaging," *Science Advances*, vol. 7, nov 2021.

[106] W. P. Hwang and T.-Y. Wu, *Relativistic Quantum Mechanics and Quantum Fields: for the 21st Century*. World Scientific, 2018.

[107] J. Greensite, *An introduction to the confinement problem*, vol. 821. Springer, 2011.

[108] M. Kormos, M. Collura, G. Takács, and P. Calabrese, "Real-time confinement following a quantum quench to a non-integrable model," *Nature Physics*, vol. 13, pp. 246–249, Mar 2017.

[109] T. Chanda, J. Zakrzewski, M. Lewenstein, and L. Tagliacozzo, "Confinement and lack of thermalization after quenches in the bosonic schwinger model," *Phys. Rev. Lett.*, vol. 124, p. 180602, May 2020.

[110] G. Delfino and P. Grinza, "Confinement in the q-state potts field theory," *Nuclear Physics B*, vol. 791, pp. 265–283, mar 2008.

[111] L. Lepori, G. Z. Tó th, and G. Delfino, "The particle spectrum of the three-state potts field theory: a numerical study," *Journal of Statistical Mechanics: Theory and Experiment*, vol. 2009, p. P11007, nov 2009.

[112] S. B. Rutkevich, "Baryon masses in the three-state potts field theory in a weak magnetic field," *Journal of Statistical Mechanics: Theory and Experiment*, vol. 2015, p. P01010, jan 2015.

[113] F. Liu, S. Whitsitt, P. Bienias, R. Lundgren, and A. V. Gorshkov, "Realizing and probing baryonic excitations in rydberg atom arrays," *arXiv [reprint 2007.07258*, Jul 2020.

[114] S. B. Rutkevich, "On the weak confinement of kinks in the one-dimensional quantum ferromagnet conb2o6," *Journal of Statistical Mechanics: Theory and Experiment*, vol. 2010, p. P07015, Jul 2010.

[115] R. Coldea, D. Tennant, E. Wheeler, E. Wawrzynska, D. Prabhakaran, M. Telling, K. Habicht, P. Smeibidl, and K. Kiefer, "Quantum criticality in an ising chain: experimental evidence for emergent e8 symmetry," *Science*, vol. 327, no. 5962, pp. 177–180, 2010.

[116] B. Lake, A. M. Tsvelik, S. Notbohm, D. Alan Tennant, T. G. Perring, M. Reehuis, C. Sekar, G. Krabbes, and B. Büchner, "Confinement of fractional quantum number particles in a condensed-matter system," *Nature Physics*, vol. 6, pp. 50–55, Jan 2010.

[117] J. Simon, W. S. Bakr, R. Ma, M. E. Tai, P. M. Preiss, and M. Greiner, "Quantum simulation of antiferromagnetic spin chains in an optical lattice," *Nature*, vol. 472, no. 7343, p. 307, 2011.

[118] S. B. Rutkevich, "Energy spectrum of bound-spinons in the quantum ising spin-chain ferromagnet," *Journal of Statistical Physics*, vol. 131, pp. 917–939, Jun 2008.

[119] P. Calabrese, F. H. L. Essler, and M. Fagotti, "Quantum quench in the transverse-field ising chain," *Phys. Rev. Lett.*, vol. 106, p. 227203, Jun 2011.

[120] W. L. Tan, P. Becker, F. Liu, G. Pagano, K. S. Collins, A. De, L. Feng, H. B. Kaplan, A. Kyprianidis, R. Lundgren, W. Morong, S. Whitsitt, A. V. Gorshkov, and C. Monroe, "Domain-wall confinement and dynamics in a quantum simulator," *Nature Physics*, vol. 17, pp. 742–747, Jun 2021.

[121] E. H. Lieb and D. W. Robinson, "The finite group velocity of quantum spin systems," in *Statistical mechanics*, pp. 425–431, Springer, 1972.

[122] T. Fukuhara, P. Schauß, M. Endres, S. Hild, M. Cheneau, I. Bloch, and C. Gross, "Microscopic observation of magnon bound states and their dynamics," *Nature*, vol. 502, no. 7469, p. 76, 2013.

[123] B. Vermersch, A. Elben, M. Dalmonte, J. I. Cirac, and P. Zoller, "Unitary n-designs via random quenches in atomic hubbard and spin models: Application to the measurement of rényi entropies," *Phys. Rev. A*, vol. 97, no. 2, p. 023604, 2018.

[124] S. van Enk and C. Beenakker, "Measuring tr ρ n on single copies of ρ using random measurements," *Phys. Rev. Lett.*, vol. 108, no. 11, p. 110503, 2012.

[125] A. Elben, B. Vermersch, M. Dalmonte, J. I. Cirac, and P. Zoller, "Rényi entropies from random quenches in atomic hubbard and spin models," *Phys. Rev. Lett.*, vol. 120, no. 5, p. 050406, 2018.

[126] A. Elben, B. Vermersch, R. van Bijnen, C. Kokail, T. Brydges, C. Maier, M. K. Joshi, R. Blatt, C. F. Roos, and P. Zoller, "Cross-platform verification of intermediate scale quantum devices," *Phys. Rev. Lett.*, vol. 124, no. 1, p. 010504, 2020.

[127] C. H. Bennett, D. P. DiVincenzo, J. A. Smolin, and W. K. Wootters, "Mixed-state entanglement and quantum error correction," *Phys. Rev. A*, vol. 54, no. 5, p. 3824, 1996.

[128] C. H. Bennett, G. Brassard, S. Popescu, B. Schumacher, J. A. Smolin, and W. K. Wootters, "Purification of noisy entanglement and faithful teleportation via noisy channels," *Phys. Rev. Lett.*, vol. 76, no. 5, p. 722, 1996.

[129] E. Knill, D. Leibfried, R. Reichle, J. Britton, R. B. Blakestad, J. D. Jost, C. Langer, R. Ozeri, S. Seidelin, and D. J. Wineland, "Randomized benchmarking of quantum gates," *Phys. Rev. A*, vol. 77, no. 1, p. 012307, 2008.

[130] J. Emerson, M. Silva, O. Moussa, C. Ryan, M. Laforest, J. Baugh, D. G. Cory, and R. Laflamme, "Symmetrized characterization of noisy quantum processes," *Science*, vol. 317, no. 5846, pp. 1893–1896, 2007.

[131] "*ibmq_santiago* v1.3.19, ibm quantum team. retrieved from https://quantum-computing.ibm.com, (2021)."

[132] J. R. McClean, N. C. Rubin, K. J. Sung, I. D. Kivlichan, X. Bonet-Monroig, Y. Cao, C. Dai, E. S. Fried, C. Gidney, B. Gimby, P. Gokhale, T. Häner, T. Hardikar, V. Havlíček, O. Higgott, C. Huang, J. Izaac, Z. Jiang, X. Liu, S. McArdle, M. Neeley, T. O'Brien, B. O'Gorman, I. Ozfidan, M. D. Radin, J. Romero, N. P. D. Sawaya, B. Senjean, K. Setia, S. Sim, D. S. Steiger, M. Steudtner, Q. Sun, W. Sun, D. Wang, F. Zhang, and R. Babbush, "OpenFermion: the electronic structure package for quantum computers," *Quantum Sci. Technol.*, vol. 5, p. 034014, Jun 2020.

[133] S. Bravyi, J. M. Gambetta, A. Mezzacapo, and K. Temme, "Tapering off qubits to simulate fermionic Hamiltonians," *arXiv preprint 1701.08213*, Jan 2017.

[134] "*ibmq_toronto* v1.1.6, ibm quantum team. retrieved from https://quantum-computing.ibm.com, (2020)."

[135] "*ibmq_paris* v1.6.23, ibm quantum team. retrieved from https://quantum-computing.ibm.com, (2020)."

[136] F. M. Surace and A. Lerose, "Scattering of mesons in quantum simulators," *New Journal of Physics*, vol. 23, p. 062001, Jun 2021.

[137] P. I. Karpov, G. Y. Zhu, M. P. Heller, and M. Heyl, "Spatiotemporal dynamics of particle collisions in quantum spin chains," *arXiv preprint 2011.11624*, Nov 2020.

[138] A. Milsted, J. Liu, J. Preskill, and G. Vidal, "Collisions of false-vacuum bubble walls in a quantum spin chain," *PRX Quantum*, vol. 3, Apr 2022.

[139] F. Liu, S. Whitsitt, P. Bienias, R. Lundgren, and A. V. Gorshkov, "Realizing and probing baryonic excitations in rydberg atom arrays," *arXiv preprint 2007.07258*, Jul 2020.

[140] P. Anderson, "Theory of dirty superconductors," *Journal of Physics and Chemistry of Solids*, vol. 11, no. 1, pp. 26–30, 1959.

[141] A. P. Mackenzie, R. K. W. Haselwimmer, A. W. Tyler, G. G. Lonzarich, Y. Mori, S. Nishizaki, and Y. Maeno, "Extremely strong dependence of superconductivity on disorder in $\mathrm{sr_2ruo_4}$," *Phys. Rev. Lett.*, vol. 80, pp. 161–164, Jan 1998.

[142] S. H. Pan, E. W. Hudson, K. M. Lang, H. Eisaki, S. Uchida, and J. C. Davis, "Imaging the effects of individual zinc impurity atoms on superconductivity in bi2sr2cacu2o8+δ," *Nature*, vol. 403, pp. 746–750, Feb 2000.

[143] M. Hagiwara, K. Katsumata, I. Affleck, B. I. Halperin, and J. P. Renard, "Observation of s=1/2 degrees of freedom in an s=1 linear-chain heisenberg antiferromagnet," *Phys. Rev. Lett.*, vol. 65, pp. 3181–3184, Dec 1990.

[144] J. Kondo, "Resistance Minimum in Dilute Magnetic Alloys," *Progress of Theoretical Physics*, vol. 32, pp. 37–49, 07 1964.

[145] "67 - the effective mass of the polaron," pp. 478–483, 1965.

[146] R. Schmidt, M. Knap, D. A. Ivanov, J.-S. You, M. Cetina, and E. Demler, "Universal many-body response of heavy impurities coupled to a fermi sea: a review of recent progress," *Reports on Progress in Physics*, vol. 81, p. 024401, jan 2018.

[147] A. Polkovnikov, "Phase space representation of quantum dynamics," *Annals of Physics*, vol. 325, no. 8, pp. 1790–1852, 2010.

[148] A. Bastianello and A. De Luca, "Nonequilibrium steady state generated by a moving defect: The supersonic threshold," *Phys. Rev. Lett.*, vol. 120, p. 060602, Feb 2018.

[149] A. Bastianello and A. De Luca, "Superluminal moving defects in the ising spin chain," *Phys. Rev. B*, vol. 98, p. 064304, Aug 2018.

[150] A. De Luca and A. Bastianello, "Entanglement front generated by an impurity traveling in an isolated many-body quantum system," *Phys. Rev. B*, vol. 101, p. 085139, Feb 2020.

[151] G. Vidal, "Efficient simulation of one-dimensional quantum many-body systems," *Phys. Rev. Lett.*, vol. 93, p. 040502, Jul 2004.

[152] J. Hauschild and F. Pollmann, "Efficient numerical simulations with Tensor Networks: Tensor Network Python (TeNPy)," *SciPost Phys. Lect. Notes*, p. 5, 2018.

[153] M. Collura, A. De Luca, D. Rossini, and A. Lerose, "Discrete time-crystalline response stabilized by domain-wall confinement," *arXiv preprint 2110.14705*, Jun 2022.

[154] S. Bravyi, D. P. DiVincenzo, and D. Loss, "Schrieffer–wolff transformation for quantum many-body systems," *Annals of Physics*, vol. 326, no. 10, pp. 2793–2826, 2011.

[155] D. J. Griffiths and D. F. Schroeter, *Introduction to quantum mechanics*. Cambridge University Press, 2018.

[156] K.-K. Ni, S. Ospelkaus, D. Wang, G. Quéméner, B. Neyenhuis, M. H. G. de Miranda, J. L. Bohn, J. Ye, and D. S. Jin, "Dipolar collisions of polar molecules in the quantum regime," *Nature*, vol. 464, p. 1324–1328, Apr 2010.

[157] B. Yan, S. A. Moses, B. Gadway, J. P. Covey, K. R. A. Hazzard, A. M. Rey, D. S. Jin, and J. Ye, "Observation of dipolar spin-exchange interactions with lattice-confined polar molecules," *Nature*, vol. 501, no. 7468, pp. 521–525, 2013.

[158] J. W. Britton, B. C. Sawyer, A. C. Keith, C.-C. J. Wang, J. K. Freericks, H. Uys, M. J. Biercuk, and J. J. Bollinger, "Engineered two-dimensional ising interactions in a trapped-ion quantum simulator with hundreds of spins," *Nature*, vol. 484, no. 7395, pp. 489–492, 2012.

[159] P. Schauß, M. Cheneau, M. Endres, T. Fukuhara, S. Hild, A. Omran, T. Pohl, C. Gross, S. Kuhr, and I. Bloch, "Observation of spatially ordered structures in a two-dimensional rydberg gas," *Nature*, vol. 491, no. 7422, pp. 87–91, 2012.

[160] H. Labuhn, D. Barredo, S. Ravets, S. de Léséleuc, T. Macrì, T. Lahaye, and A. Browaeys, "Tunable two-dimensional arrays of single rydberg atoms for realizing quantum ising models," *Nature*, vol. 534, no. 7609, pp. 667–670, 2016.

[161] S. Ebadi, T. T. Wang, H. Levine, A. Keesling, G. Semeghini, A. Omran, D. Bluvstein, R. Samajdar, H. Pichler, W. W. Ho, S. Choi, S. Sachdev, M. Greiner, V. Vuletić, and M. D. Lukin, "Quantum phases of matter on a 256-atom programmable quantum simulator," *Nature*, vol. 595, no. 7866, pp. 227–232, 2021.

[162] M. O. Brown, T. Thiele, C. Kiehl, T.-W. Hsu, and C. A. Regal, "Gray-molasses optical-tweezer loading: Controlling collisions for scaling atom-array assembly," *Phys. Rev. X*, vol. 9, p. 011057, Mar 2019.

[163] E. E. Edwards, S. Korenblit, K. Kim, R. Islam, M.-S. Chang, J. K. Freericks, G.-D. Lin, L.-M. Duan, and C. Monroe, "Quantum simulation and phase diagram of the transverse-field ising model with three atomic spins," *Phys. Rev. B*, vol. 82, p. 060412, Aug 2010.

[164] K. Kim, M.-S. Chang, R. Islam, S. Korenblit, L.-M. Duan, and C. Monroe, "Entanglement and tunable spin-spin couplings between trapped ions using multiple transverse modes," *Phys. Rev. Lett.*, vol. 103, p. 120502, Sep 2009.

[165] R. Islam, C. Senko, W. C. Campbell, S. Korenblit, J. Smith, A. Lee, E. E. Edwards, C.-C. J. Wang, J. K. Freericks, and C. Monroe, "Emergence and frustration of magnetism with variable-range interactions in a quantum simulator," *Science*, vol. 340, no. 6132, pp. 583–587, 2013.

[166] J. Zhang, G. Pagano, P. W. Hess, A. Kyprianidis, P. Becker, H. Kaplan, A. V. Gorshkov, Z.-X. Gong, and C. Monroe, "Observation of a many-body dynamical phase transition with a 53-qubit quantum simulator," *Nature*, vol. 551, no. 7682, pp. 601–604, 2017.

[167] A. Omran, H. Levine, A. Keesling, G. Semeghini, T. T. Wang, S. Ebadi, H. Bernien, A. S. Zibrov, H. Pichler, S. Choi, J. Cui, M. Rossignolo, P. Rembold, S. Montangero, T. Calarco,

M. Endres, M. Greiner, V. Vuletić, and M. D. Lukin, "Generation and manipulation of schrödinger cat states in rydberg atom arrays," *Science*, vol. 365, no. 6453, pp. 570–574, 2019.

[168] H. Bernien, S. Schwartz, A. Keesling, H. Levine, A. Omran, H. Pichler, S. Choi, A. S. Zibrov, M. Endres, M. Greiner, V. Vuletić, and M. D. Lukin, "Probing many-body dynamics on a 51-atom quantum simulator," *Nature*, vol. 551, no. 7682, pp. 579–584, 2017.

[169] P. Jurcevic, B. P. Lanyon, P. Hauke, C. Hempel, P. Zoller, R. Blatt, and C. F. Roos, "Quasiparticle engineering and entanglement propagation in a quantum many-body system," *Nature*, vol. 511, p. 202–205, Jul 2014.

[170] E. A. Martinez, C. A. Muschik, P. Schindler, D. Nigg, A. Erhard, M. Heyl, P. Hauke, M. Dalmonte, T. Monz, P. Zoller, and R. Blatt, "Real-time dynamics of lattice gauge theories with a few-qubit quantum computer," *Nature*, vol. 534, pp. 516–519, Jun 2016.

[171] N. Friis, O. Marty, C. Maier, C. Hempel, M. Holzäpfel, P. Jurcevic, M. B. Plenio, M. Huber, C. Roos, R. Blatt, and B. Lanyon, "Observation of entangled states of a fully controlled 20-qubit system," *Phys. Rev. X*, vol. 8, p. 021012, Apr 2018.

[172] H. Labuhn, S. Ravets, D. Barredo, L. Béguin, F. Nogrette, T. Lahaye, and A. Browaeys, "Single-atom addressing in microtraps for quantum-state engineering using rydberg atoms," *Phys. Rev. A*, vol. 90, p. 023415, Aug 2014.

[173] H. Schempp, G. Günter, S. Wüster, M. Weidemüller, and S. Whitlock, "Correlated exciton transport in rydberg-dressed-atom spin chains," *Phys. Rev. Lett.*, vol. 115, p. 093002, Aug 2015.

[174] F. Yang, S. Yang, and L. You, "Quantum transport of rydberg excitons with synthetic spin-exchange interactions," *Phys. Rev. Lett.*, vol. 123, p. 063001, Aug 2019.

[175] P. Richerme, Z.-X. Gong, A. Lee, C. Senko, J. Smith, M. Foss-Feig, S. Michalakis, A. V. Gorshkov, and C. Monroe, "Non-local propagation of correlations in quantum systems with long-range interactions," *Nature*, vol. 511, p. 198–201, Jul 2014.

[176] P. Schauß, J. Zeiher, T. Fukuhara, S. Hild, M. Cheneau, T. Macrì, T. Pohl, I. Bloch, and C. Gross, "Crystallization in ising quantum magnets," *Science*, vol. 347, no. 6229, pp. 1455–1458, 2015.

[177] A. Keesling, A. Omran, H. Levine, H. Bernien, H. Pichler, S. Choi, R. Samajdar, S. Schwartz, P. Silvi, S. Sachdev, P. Zoller, M. Endres, M. Greiner, V. Vuletić, and M. D. Lukin, "Quantum kibble–zurek mechanism and critical dynamics on a programmable rydberg simulator," *Nature*, vol. 568, no. 7751, pp. 207–211, 2019.

[178] A. W. Glaetzle, M. Dalmonte, R. Nath, I. Rousochatzakis, R. Moessner, and P. Zoller, "Quantum spin-ice and dimer models with rydberg atoms," *Phys. Rev. X*, vol. 4, p. 041037, Nov 2014.

[179] L. I. R. Gil, R. Mukherjee, E. M. Bridge, M. P. A. Jones, and T. Pohl, "Spin squeezing in a rydberg lattice clock," *Phys. Rev. Lett.*, vol. 112, p. 103601, Mar 2014.

[180] R. M. W. van Bijnen and T. Pohl, "Quantum magnetism and topological ordering via rydberg dressing near förster resonances," *Phys. Rev. Lett.*, vol. 114, p. 243002, Jun 2015.

[181] A. W. Glaetzle, M. Dalmonte, R. Nath, C. Gross, I. Bloch, and P. Zoller, "Designing frustrated quantum magnets with laser-dressed rydberg atoms," *Phys. Rev. Lett.*, vol. 114, p. 173002, Apr 2015.

[182] J. E. Johnson and S. L. Rolston, "Interactions between rydberg-dressed atoms," *Phys. Rev. A*, vol. 82, p. 033412, Sep 2010.

[183] J. B. Balewski, A. T. Krupp, A. Gaj, S. Hofferberth, R. Löw, and T. Pfau, "Rydberg dressing: understanding of collective many-body effects and implications for experiments," *New Journal of Physics*, vol. 16, p. 063012, Jun 2014.

[184] R. Mukherjee, T. C. Killian, and K. R. A. Hazzard, "Accessing rydberg-dressed interactions using many-body ramsey dynamics," *Phys. Rev. A*, vol. 94, p. 053422, Nov 2016.

[185] Y. Y. Jau, A. M. Hankin, T. Keating, I. H. Deutsch, and G. W. Biedermann, "Entangling atomic spins with a rydberg-dressed spin-flip blockade," *Nature Physics*, vol. 12, no. 1, pp. 71–74, 2016.

[186] J. Zeiher, R. van Bijnen, P. Schauß, S. Hild, J.-y. Choi, T. Pohl, I. Bloch, and C. Gross, "Many-body interferometry of a rydberg-dressed spin lattice," *Nature Physics*, vol. 12, no. 12, pp. 1095–1099, 2016.

[187] V. Borish, O. Marković, J. A. Hines, S. V. Rajagopal, and M. Schleier-Smith, "Transverse-field ising dynamics in a rydberg-dressed atomic gas," *Phys. Rev. Lett.*, vol. 124, p. 063601, Feb 2020.

[188] S. Hollerith, K. Srakaew, D. Wei, A. Rubio-Abadal, D. Adler, P. Weckesser, A. Kruckenhauser, V. Walther, R. van Bijnen, J. Rui, C. Gross, I. Bloch, and J. Zeiher, "Realizing distance-selective interactions in a rydberg-dressed atom array," *Phys. Rev. Lett.*, vol. 128, p. 113602, Mar 2022.

[189] F. Letscher and D. Petrosyan, "Mobile bound states of rydberg excitations in a lattice," *Phys. Rev. A*, vol. 97, p. 043415, Apr 2018.

[190] M. Saffman, T. G. Walker, and K. Mølmer, "Quantum information with rydberg atoms," *Rev. Mod. Phys.*, vol. 82, pp. 2313–2363, Aug 2010.

[191] H. Rabitz, R. de Vivie-Riedle, M. Motzkus, and K. Kompa, "Whither the future of controlling quantum phenomena?," *Science*, vol. 288, no. 5467, pp. 824–828, 2000.

[192] J. Werschnik and E. K. U. Gross, "Quantum optimal control theory," *J. Phys. B:At. Mol. Opt. Phys.*, vol. 40, pp. R175–R211, Sep 2007.

[193] R. Mukherjee, H. Xie, and F. Mintert, "Bayesian optimal control of greenberger-horne-zeilinger states in rydberg lattices," *Phys. Rev. Lett.*, vol. 125, p. 203603, Nov 2020.

[194] H. Bernien, S. Schwartz, A. Keesling, H. Levine, A. Omran, H. Pichler, S. Choi, A. S. Zibrov, M. Endres, M. Greiner, V. Vuletić, and M. D. Lukin, "Probing many-body dynamics on a 51-atom quantum simulator," *Nature*, vol. 551, pp. 579–584, Nov 2017.

[195] M. C. Bañuls, R. Blatt, J. Catani, A. Celi, J. I. Cirac, M. Dalmonte, L. Fallani, K. Jansen, M. Lewenstein, S. Montangero, C. A. Muschik, B. Reznik, E. Rico, L. Tagliacozzo, K. Van Acoleyen, F. Verstraete, U.-J. Wiese, M. Wingate, J. Zakrzewski, and P. Zoller, "Simulating lattice gauge theories within quantum technologies," *The European Physical Journal D*, vol. 74, p. 165, Aug 2020.

[196] C. Adam, "Scattering processes in the massive schwinger model," *Phys. Rev. D*, vol. 55, pp. 6299–6312, May 1997.

[197] T. Rakovszky, F. Pollmann, and C. W. von Keyserlingk, "Sub-ballistic growth of rényi entropies due to diffusion," *Phys. Rev. Lett.*, vol. 122, p. 250602, Jun 2019.

Appendix A

A.1 The Jordan-Wigner Transformation

In this section, we introduce the Jordan-Wigner transformation in the context of diagonalising the transverse field Ising model (TFIM). The TFIM is given by the Hamiltonian:

$$H = -J \sum_{i}^{L} [\sigma_i^z \sigma_{i+1}^z + h\sigma_i^x]. \tag{A.1}$$

This Hamiltonian is exactly mapped to a free fermion system via Jordan-Wigner and Bogoliubov transformations. The Jordan-Wigner transformation is given by

$$c_j^\dagger = e^{+i\pi \sum_{k=1}^{j-1} \sigma_k^+ \sigma_k^-} \sigma_j^+, \tag{A.2}$$

$$c_j = e^{-i\pi \sum_{k=1}^{j-1} \sigma_k^+ \sigma_k^-} \sigma_j^-. \tag{A.3}$$

It helps to note the following properties of this transformation

$$c_j^\dagger c_j = \sigma_j^+ \sigma_j^-, \tag{A.4}$$

$$\sigma_j^x = 2c_j^\dagger c_j - 1, \tag{A.5}$$

$$\sigma_j^z = \frac{\sigma_j^+ + \sigma_j^1}{2} = \prod_{k=1}^{j-1} (1 - 2n_k)\big(c_j + c_j^\dagger\big), \tag{A.6}$$

$$e^{\pm\sum_{k=1}^{j-1}\sigma_k^+\sigma_k^-} = \prod_{k=1}^{j-1}(1-2n_k). \tag{A.7}$$

Substituting these into the Hamiltonian gives

$$\begin{aligned} H &= -\sum_{j=1}^{L}\prod_{k=1}^{j-1}(1-2n_k)\big(c_j+c_j^\dagger\big)\prod_{k'=1}^{j}(1-2n_{k'})\big(c_{j+1}+c_{j+1}^\dagger\big) - h\sum_{j=1}^{L}(2c_j^\dagger c_j-1) \\ &= -\sum_{i=1}^{L}\left[\prod_{j=1}^{i}(1-2n_j)\right]^2\big(c_i+c_i^\dagger\big)(1-2n_i)\big(c_{i+1}+c_{i+1}^\dagger\big) - h\sum_{j=1}^{L}(2c_j^\dagger c_j-1) \\ &\equiv -\sum_{i=1}^{L}\big(c_i^\dagger-c_i\big)\big(c_{i+1}+c_{i+1}^\dagger\big) - 2h\sum_{j=1}^{L}c_j^\dagger c_j. \end{aligned} \tag{A.8}$$

We exploit the translational symmetry by computing the Fourier transform of the Hamiltonian

$$c_j = \frac{1}{\sqrt{N}}\sum_k e^{ikj}c_k, \tag{A.9}$$

$$c_j^\dagger = \frac{1}{\sqrt{N}}\sum_k e^{-ikj}c_k^\dagger. \tag{A.10}$$

This gives

$$H = \sum_k \begin{bmatrix} c_k^\dagger & c_{-k} \end{bmatrix} \begin{bmatrix} -\cos(k)-h & -i\sin(k) \\ i\sin(k) & \cos(k)+h \end{bmatrix} \begin{bmatrix} c_k \\ c_{-k}^\dagger \end{bmatrix}. \tag{A.11}$$

From here, this Hamiltonian can be diagonalised via a Bogoliubov Transformation of the form

$$\begin{bmatrix} \eta_q \\ \eta_{-q}^\dagger \end{bmatrix} = \begin{bmatrix} u_q & iv_q \\ iv_q & u_q \end{bmatrix} \begin{bmatrix} c_q \\ c_{-q}^\dagger \end{bmatrix}, \tag{A.12}$$

in which the new η operators obey the standard fermionic commutation relations. This leads to the Hamiltonian taking the form

$$H = \sum_q \omega(q)\eta_q^\dagger\eta_q, \tag{A.13}$$

$$\omega(q) = 2J\sqrt{1-2h\cos k+h^2}. \tag{A.14}$$

where, the fermionic operators $\eta_q^\dagger$ approximately describe domain-walls in the spin chain in the limit $J \gg h$.

A.2 Semiclassical Two Fermion Subspace Hamiltonian

To derive the two fermion subspace for the TFIM with a longitudinal field we start from $H = H_0 + H_I$, where H_0 is the transverse field Ising model and H_I is the longitudinal,

$$H_I = -h_z \sum_i \sigma_i^z. \tag{A.15}$$

We can project this Hamiltonian in the two fermion subspace and obtain

$$\mathcal{PH} \left|k_1, k_2\right\rangle = \left(\epsilon(k_1) + \epsilon(k_2)\right) \left|k_1, k_2\right\rangle - h_z \int \frac{dq_1 dq_2}{(2\pi)^2} \left|q_1, q_2\right\rangle \left\langle q_1, q_2\right| \sum_i \sigma_i^z \left|k_1, k_2\right\rangle . \tag{A.16}$$

To continue let us consider

$$\int \frac{dq_1 dq_2}{(2\pi)^2} \left|q_1, q_2\right\rangle \left\langle q_1, q_2\right| \sum_i \sigma_i^z \left|k_1, k_2\right\rangle . \tag{A.17}$$

By using the translational symmetry of the system we can make the transformation, i.e $\sigma_j^x = e^{iPj} \sigma_0 e^{-iPj}$ and get

$$\int \frac{dq_1 dq_2}{(2\pi)^2} \left|q_1, q_2\right\rangle \sum_i e^{-i(q_1+q_2-k_1-k_2)j} \left\langle q_1, q_2\right| \sigma_0^x \left|k_1, k_2\right\rangle . \tag{A.18}$$

From here we can use a form factor approach outlined by S. B. Rutkevich in Ref. [118], and consider the limit that the transverse field strength is small. This results in the approximation

$$\bar{\sigma}^{-1} \left\langle q_1, q_2\right| \sigma_0^x \left|k_1, k_2\right\rangle \sim \frac{2i}{q_1 - k_1} \frac{2i}{q_2 - k_2} - \frac{2i}{q_1 - k_2} \frac{2i}{q_2 - k_1}. \tag{A.19}$$

Leaving us with

$$\bar{\sigma} \int \frac{dq_1 dq_2}{(2\pi)^2} \left|q_1, q_2\right\rangle \sum_i e^{-i(q_1+q_2-k_1-k_2)j} \left[\frac{2i}{q_1 - k_1} \frac{2i}{q_2 - k_2} - \frac{2i}{q_1 - k_2} \frac{2i}{q_2 - k_1}\right]. \tag{A.20}$$

To proceed we define the states in the coordinate representation as the Fourier transforms of the fermion eigenstates

$$\left|j_1, j_2\right\rangle = \int \frac{dk_1 dk_2}{(2\pi)^2} e^{ik_1 j_1 + ik_2 j_2} \left|k_1, k_2\right\rangle \tag{A.21}$$

Then

$$\langle l_1, l_2| H_I |j_1, j_2\rangle \sim h_z\bar{\sigma}\int \frac{dq_1dq_2dk_1dk_2}{(2\pi)^4}|q_1, q_2\rangle \sum_i e^{-i(q_1+q_2-k_1-k_2)j} \times e^{-i(q_1-k_1)l_1}e^{-i(q_2-k_2)l_2}\left[\frac{2i}{q_1-k_1}\frac{2i}{q_2-k_2}-\frac{2i}{q_1-k_2}\frac{2i}{q_2-k_1}\right] \quad \text{(A.22)}$$

We now consider only the first term and define $P_i = \frac{q_i+k_i}{2}$ and $p_i = q_i - k_i$

$$\bar{\sigma}h_z\sum_i\int\frac{dP_1dP_2dp_1dp_2}{(2\pi)^4}e^{-iP_1(l_1-j_1)-iP_2(l_2-j_2)}e^{\frac{-il_1p_1}{2}+\frac{-il_2p_2}{2}+\frac{-ij_1p_1}{2}+\frac{-ij_2p_2}{2}}e^{-i(p_1+p_2)j}\frac{2i}{p_1}\frac{2i}{p_2}. \quad \text{(A.23)}$$

Computing the integrals over P_1 and P_2 we obtain

$$\bar{\sigma}h_z\delta_{l_1,j_1}\delta_{l_2,j_2}\sum_i\int\frac{dp_1dp_2}{(2\pi)^2}e^{-ij_1p_1-ij_2p_2}e^{-i(p_1+p_2)j}\frac{2i}{p_1}\frac{2i}{p_2}. \quad \text{(A.24)}$$

The sum over j gives a factor of $2\pi\delta(p_1+p_2)$ leaving us with

$$\bar{\sigma}h_z\delta_{l_1,j_1}\delta_{l_2,j_2}\int\frac{dp_1}{2\pi}e^{-i(j_1-j_2)p_1}\frac{4}{p_1^2}. \quad \text{(A.25)}$$

This is a standard integral type, leaving us with (now including both contributing terms)

$$\langle l_1, l_2| H_I |j_1, j_2\rangle \sim 2\bar{\sigma}h_z(\delta_{l_1,j_1}\delta_{l_2,j_2}-\delta_{l_1,j_2}\delta_{l_2,j_1})|j_1-j_2|. \quad \text{(A.26)}$$

Form here is clear to see the semiclassical effect of the longitudinal field is a confining potential linear in fermion separation with a gradient of $2\bar{\sigma}h_z$.

A.3 Eigensystem of the Two domain-wall Subspace

Recall the two domain-wall subspace Hamiltonian given by Eq. 3.15,

$$\mathcal{H} = \sum_n 2h_z n|n\rangle\langle n| - 2h_x\cos\frac{k}{2}\left[|n\rangle\langle n-1| + |n\rangle\langle n+1|\right], \quad \text{(A.27)}$$

where $|n\rangle$ is corresponds to a meson state with width n, k is the meson momentum, h_x and h_z are constants. Note, as the Hamiltonian is already diagonal in momentum space we have dropped is as a quantum number for clarity. The eigenvalue equation for this Hamiltonian is given by

$$(2h_z n - E)\psi(n) - 2h_x \cos\frac{k}{2}[\psi(n+1) + \psi(n-1)] = 0. \tag{A.28}$$

By defining the variables $\nu_{k,\alpha} = \frac{E_{k,\alpha}}{2h_z}$ and $x_k = \frac{2h_x \cos\frac{k}{2}}{h_z}$, this eigenvalue equation becomes

$$\psi(n+1) + \psi(n-1) = \frac{2(n-\nu_{k,\alpha})}{x_k}\psi(n). \tag{A.29}$$

The recurrence relation for the Bessel functions is given by $\mathcal{F}_{\xi+1}(x) + \mathcal{F}_{\xi-1}(x) = \frac{2\xi}{x}\mathcal{F}_\xi(x)$, thus we can quickly read of that

$$\psi(n) = A\mathcal{J}_{n-\nu_{k,\alpha}}(x_k) + B\mathcal{Y}_{n-\nu_{k,\alpha}}(x_k), \tag{A.30}$$

where $\mathcal{J}$ is the Bessel function of the first kinda and $\mathcal{Y}$ is the Bessel function of the second kind. For an infinite system we know $B = 0$ as the Bessel function of the second kind is unbounded. Hence, the eigenfunctions of this Hilbert space on an infinitely long spin chain are given by

$$|k,\alpha\rangle = \sum_n C_\alpha \mathcal{J}_{n-\nu_{k,\alpha}}(x_k)\,|k,n\rangle\,, \tag{A.31}$$

where we have recovered the momentum as a quantum number and C_α is a normalisation constant.

Appendix B

B.1 Effectiveness of Error Mitigation Methods

This section is lifted from the supplementary material of Ref. [1].

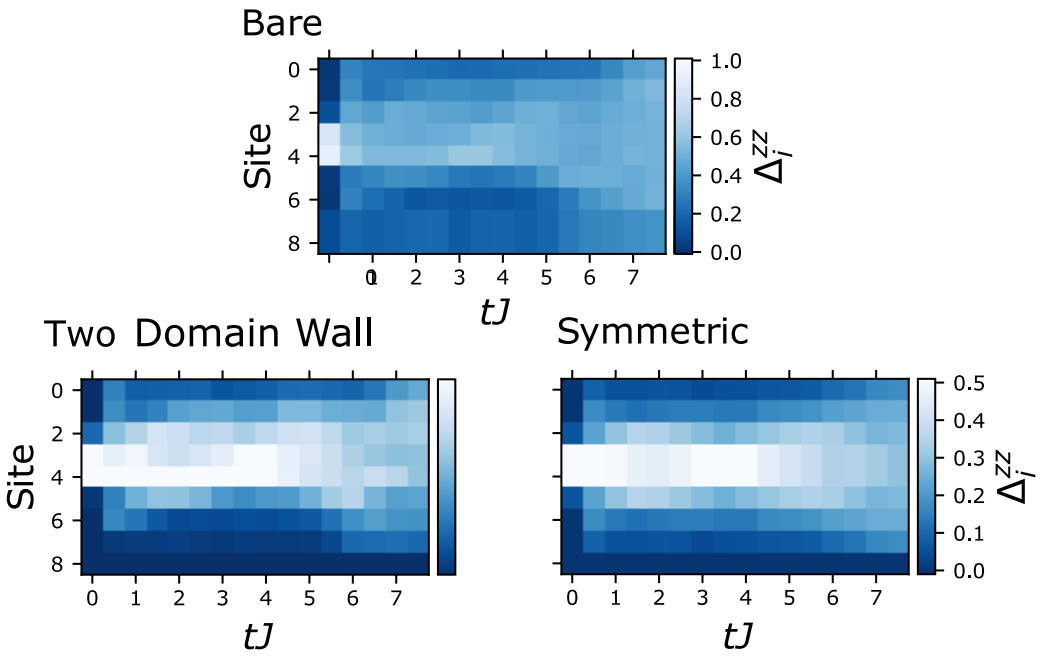

Figure B.1: A comparison of result collected from the IBM device with and without error mitigation. The IBM results for Δ_i^{zz} with $h_x = 0.5$, $h_z = 0.5$ and $L = 9$. The bare result are shown first followed by the same data after post selection of the two domain-wall subspace states, and finally the symmetrised results. The background noise is considerably reduced by the two domain-wall subspace projection and the light cones are restored by the process of forcing the inversion symmetry of the initial state. This allows the confinement physics to be observed and the gradients of light cones to be measured.

In Fig. B.1 a comparison of the results taken from the IBM device before and after error mitigation are presented. In the bare results we see that there is some evidence of the qualitative structure of

the light cones expected, but it is not obvious. After the two domain-wall subspace projection, the background noise of the results is reduced highlighting the domain-wall position more clearly. Finally, after symmetrisation two light cones can be seen, one corresponding to each expected velocity. This highlights the effect of the subspace projection as well as enforcing the inversion symmetry of the initial state in projecting away background noise and extracting the physical results.

Appendix C

This appendix is lifted from the supplementary material of Ref. [2].

C.1 Impurities in the Two Domain-Wall Subspace

Let us consider the subspace with two domain-walls and an impurity $|j_1, j_2, y\rangle = |\uparrow \ldots \uparrow\downarrow_{j_1} \ldots \downarrow\uparrow_{j_2} \ldots \uparrow\rangle$ and a single impurity with position y. We label the three particle state as $|j_1, j_2, y\rangle$ and wavefunction $\psi(j_1, j_2, y) = \langle j_1, j_2, y|\psi\rangle$. By projecting the Hamiltonian in this subspace $\hat{H} \to \hat{H}^P$ we find

$$\begin{aligned}\hat{H}^P\psi(j_1,j_2,y) = -h_x\big[\psi(j_1+1,j_2,y)+\psi(j_1-1,j_2,y)+\psi(j_1,j_2+1,y)+\psi(j_1,j_2-1,y)\big]\\ +\chi|j_1-j_2|\psi(j_1,j_2,y)+-\tau\left[\psi(j_1,j_2,y+1)+\psi(j_1,j_2,y-1)\right]\\ -(d-h_x)\left[\delta_{j_1,y+1}\psi(j_1-1,j_2,y)+\delta_{j_1,y}\psi(j_1+1,j_2,y)+\delta_{j_2,y+1}\psi(j_1,j_2-1,y)+\delta_{j_2,y}\psi(j_1,j_2+1,y)\right].\end{aligned} \tag{C.1}$$

Above, the exclusion $j_1 < j_2$ is enforced when needed. The confining force is $\chi = 2h_z$ and the first line describes the fermion-fermion (i.e. meson) dynamics, the second line contains the impurity dynamics and lastly the third line captures the meson-impurity interaction. We can conveniently focus on a sector with a well defined total momentum and reduce the problem to a two dimensional one. With a slight abuse of notation we set

$$\psi(j_1, j_2, y) \to e^{iK(j_1+j_2+y)}\psi(j_1 - y, j_2 - y) \tag{C.2}$$

and Hamiltonian

$$\hat{H}^P\psi(j_1,j_2) = -h_x\big[e^{iK}\psi(j_1+1,j_2)+e^{-iK}\psi(j_1-1,j_2)+e^{iK}\psi(j_1,j_2+1)+e^{-iK}\psi(j_1,j_2-1)\big] + \chi|j_1-j_2|\psi(j_1,j_2)+-\tau\big[e^{iK}\psi(j_1-1,j_2-1)+e^{-iK}\psi(j_1+1,j_2+1)\big] -(d-h_x)\big[\delta_{j_1,1}e^{-iK}\psi(j_1-1,j_2)+\delta_{j_1,0}e^{iK}\psi(j_1+1,j_2)+\delta_{j_2,1}e^{-iK}\psi(j_1,j_2-1)+\delta_{j_2,0}e^{iK}\psi(j_1,j_2+1)\big]. \tag{C.3}$$

For the sake of simplicity, in this work we always focus on the case of zero total momentum $K=0$.

The fermion-impurity scattering matrix

A key ingredient in the semiclassical treatment of the metastable state is the transmission amplitude of the fermion-impurity scattering. In the weak transverse field limit, this can be analytically computed. In order to do this, we now remove the confinement in Eq. (C.3) and focus on the single domain-wall problem $\psi(j_1,j_2)\to\psi(j_1)$. In this case, we now look for the eigenvectors of the time-independent Schrodinger equation

$$E\psi(j) = -(h_xe^{iK}+\tau e^{-iK})\psi(j+1)-(h_xe^{-iK}+\tau e^{iK})\psi(j-1)-(d-h_x)[\delta_{j,1}e^{-iK}\psi(j-1) + \delta_{j,0}e^{iK}\psi(j+1)]. \tag{C.4}$$

The asymptotic scattering solution can be written as

$$\tilde{\psi}(j) = \begin{cases} \psi_{\text{in}}(j) = e^{iqj}+r(q,K)e^{i\bar{q}j} & j\le 0, \\ \psi_{\text{out}}(j) = t(q,K)e^{i\bar{q}j} & j\ge 1. \end{cases} \tag{C.5}$$

Notice that due to the motion of the impurity the incoming momentum q is not reflected to $-q$, but rather on all the possible eigenenergy solutions $\bar{q}$ where $E=\epsilon(q)=\epsilon(\bar{q})$ and

$$\epsilon(q) = -2h_x\cos(K+q)-2\tau\cos(K-q). \tag{C.6}$$

Above, we are assuming $\partial_q \epsilon(q) = v(q) > 0$, the case $v(q) < 0$ is symmetric under parity reflection. $r(q,K)$ and $t(q,K)$ are the reflection and transmission coefficient respectively, while $R(q,K) = |r(q,K)|^2$ and $T(q,K) = |t(q,K)|^2$ are the reflection and transmission probability. Of course, one has $R+T=1$. The coefficients r,t are determined by imposing the Schrodinger equation at $j = \{0,1\}$ and after some simple algebraic manipulations one gets the conditions

$$\Big(\frac{(h_x e^{iK} + \tau e^{-iK})}{(d-h_x)e^{iK}} + 1\Big)\psi_{\text{out}}(1) = \frac{(h_x e^{iK} + \tau e^{-iK})}{(d-h_x)e^{iK}}\psi_{\text{in}}(1), \tag{C.7}$$

$$\Big(\frac{(h_x e^{-iK} + \tau e^{iK})}{(d-h_x)e^{iK}} + 1\Big)\psi_{\text{in}}(0) = \frac{(h_x e^{-iK} + \tau e^{iK})}{(d-h_x)e^{-iK}}\psi_{\text{out}}(0)\,. \tag{C.8}$$

From these, the following expression for $r(q,K)$ is easily computed

$$r(q,K) = -\frac{1 - \Big(\frac{(d-h_x)}{(h_x+\tau e^{i2K})} + 1\Big)^{-1}\Big(\frac{(d-h_x)}{(h_x+\tau e^{-i2K})} + 1\Big)^{-1}}{1 - e^{i(\bar{q}-q)}\Big(\frac{(d-h_x)}{(h_x+\tau e^{i2K})} + 1\Big)^{-1}\Big(\frac{(d-h_x)}{(h_x+\tau e^{-i2K})} + 1\Big)^{-1}} \tag{C.9}$$

and the transmission rate follows as $T(q,K) = 1 - |r(q,K)|^2$. Notice that in the case of static a impurity $\tau = 0$, the transmission rate becomes $K-$independent as expected and has the simple form

$$T(q) = \frac{4\sin^2 q}{(d/h_x)^2 + (d/h_x)^{-2} - 2\cos(2q)}\,. \tag{C.10}$$

The mesonic energies

The form of the mesonic energies in the bulk are given in Appendix A.3. We use a similar analysis to now provide the details on the semiclassical requantization of the energies of the metastable bound states, focusing on $\tau = 0$. As we discussed in the main text, we look at the metastable state as two independent fermions bouncing on a hard wall potential. In this respect, the energy of the metastable boundstate is given by $E_{j_1,j_2} = E_{j_1} + E_{j_2} + \chi$ with E_j the quantized energy levels of each fermion. Focusing on the right fermion, its wavefunction obeys the time-independent Schrodinger equation

$$E_j\psi_{E_j}(x) = -h_x\psi_{E_j}(x+1) - h_x\psi_{E_j}(x-1) + \chi x\psi_{E_j}(x) \qquad x > 0 \tag{C.11}$$

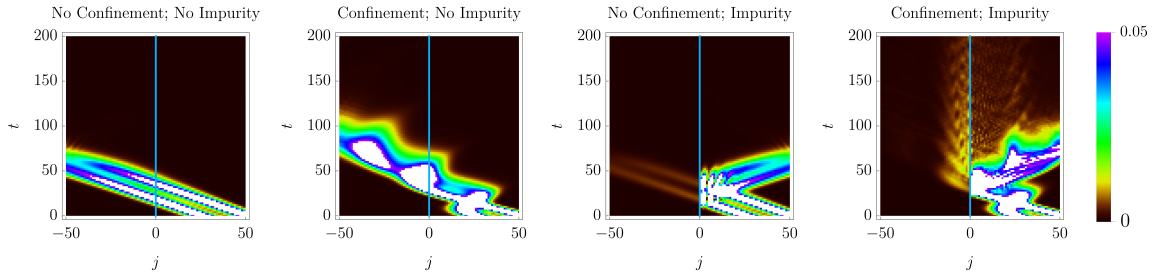

Figure C.1: Two-fermion wavepacket collision against a static impurity for the same initial conditions, but in the presence and absence of confinement and defected bond (see text). Here, we focus on the domain-wall probability as a function of space and time (measured in units of h_x).

and boundary condition $\psi_{E_j}(0) = 0$. This equation, apart from a numerical factor, is very similar to the wavefunction in the relative coordinates of two confined domain-walls, hence it can be solved in a similar manner. The eigenfunctions are parametrized by Bessel functions

$$\psi_{E_j}(x) = J_{x-E_j/\chi}\left(-2h_x/\chi\right) . \tag{C.12}$$

The energies are then found by imposing the condition $J_{-E_j/\chi}\left(-2h_x/\chi\right) = 0$.

Numerical simulations in the two domain-wall subspace

Within the two domain-wall subspace, we have great control on the numerical simulations of the meson scattering. In Fig. C.1 we provide extra evidence on the possibility of forming metastable bound states through the interplay of the confinement and impurity-scattering. We initialize the two domain-walls in two narrow wavepackets with momentum $-\pi/2$ and relative distance 25 sites. The domain-wall closest to the static impurity (centered at $j = 0$) is placed at 25 sites from it. Then, we let evolve the two domain-walls in four different cases. From the left to the right: no confining force $\chi = 0$ and no impurity $d = h_x$; confinement $\chi = 0.1h_x$ but no defect $d = h_x$; no confinement $\chi = 0$ but non-trivial defect $d = 0.2h_x$; and finally the case where both confinement $\chi = 0.1h_x$ and defect $d = 0.2h_x$ are present. In the latter case, there is clearly a finite probability of trapping the meson on the impurity. We wish now to supplement the analysis of Fig. 6.3 concerning the metastable state formation in the quantum regime with further analysis.

Hence, we take the quantization of the metastable states one step further by exploring the effect on the

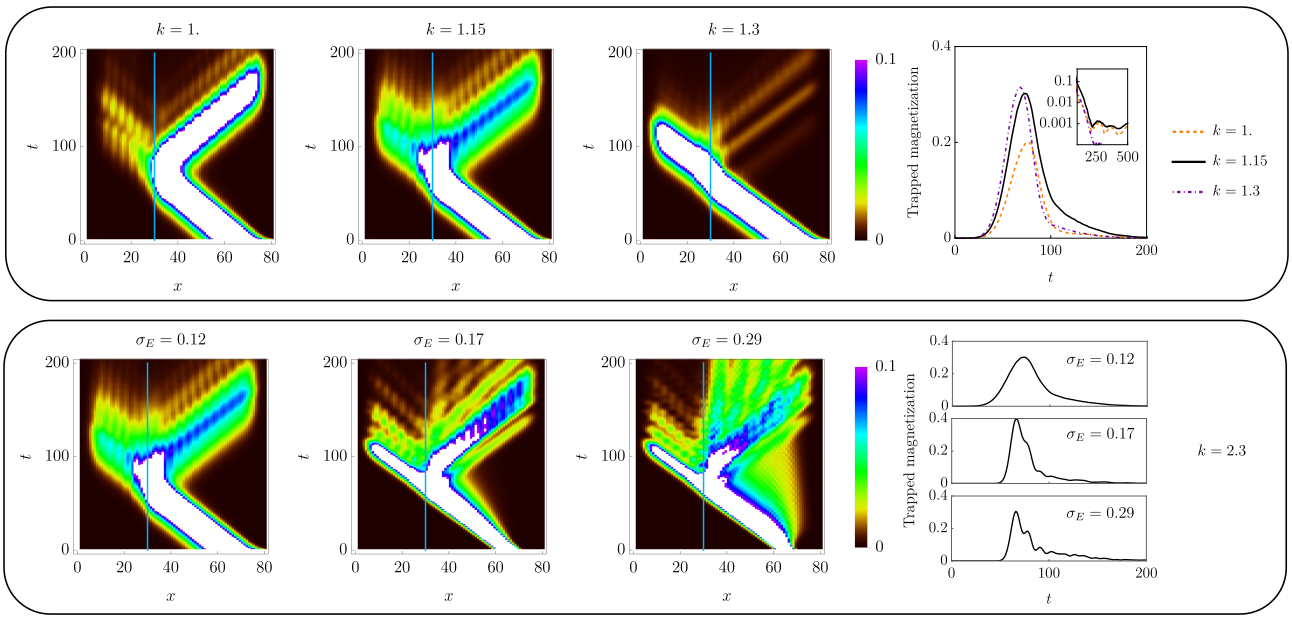

Figure C.2: By initialising in the wavepacket given in Eq. C.13 with carefully chosen values of k and σ_k we are able to explore energy space precisely. Here we use $h_x = 1$, $h_z = \frac{1}{3}$, $X = 65$ and $\alpha = 2$ with a stationary impurity located at site 30 such that $d = 0.7$. In the upper panel we choose σ_k^2 such that the variance in energy space is small, $\sigma_E \sim 0.12$. By varying k we are able to 'scan' across energy space and directly capture metastable states via a resulting long lived meson at the impurity. In the lower panel we initialise k such that we observe a metastable state and slowly increase σ_E by decreasing σ_k. This allows us to observe the resonances between different metastable states in the form of emergent oscillations in the trapped fraction of wavepacket in the non-equilibrium dynamics.

resulting non-equilibrium dynamics of the initial wave packet with respect to changes in its energy, E, as well as the variance of this energy, σ_E. In order to have optimal control we turn to a sophisticated initial wavepacket given by

$$\langle j_1, j_2|\psi\rangle = \int dq\, e^{-\sigma_k^2(q-k)^2} e^{iq(\frac{j_1+j_2}{2}-X)} \mathcal{J}_{j_2-j_1-\nu_{q,\alpha}}\left(\frac{2h_x}{h_z}\cos\frac{q}{2}\right) \tag{C.13}$$

where k is the initial expected momentum of the wavepacket, X is the initial centre of the wavepacket and $\nu_{q,\alpha} = \frac{\epsilon_{q,\alpha}}{2h_z}$ in which $\epsilon_{q,\alpha}$ is the energy of the two domain-wall subspace and α labels the energy level [1]. This wave packet allows us to directly choose the energy level we consider but also, via the choice of k and σ_k, we have good control of E and σ_E.

Firstly, we 'scan' through energy space with a wavepacket that has a small σ_E. This directly shows that, when a wavepacket is centred on the energy of a metastable state, we observe the long lifetime of a meson trapped at the defect. As we move away form this energy, we in turn loose this signature, this

can be seen in the upper panel of Fig. C.2. Furthermore, we present results of the resonances observed as we increase σ_E of a wavepacket with energy centered such that we are capturing a metastable state. Clearly seen in lower panel of Fig. C.2, as the variance grows, more resonances are captured leading to more pronounced oscillations in the trapped fraction of the wavepacket. This is consistent with the interpretation that these oscillations are due to resonances between metastable state energies, i.e., as we increase σ_E a large number of metastable states are excited.

Further details about Fig. 6.3 and 6.2.2

To generate the data for Figs. 6.3 and 6.2.2, we used a wavepacket similar to Eq. (C.13), but in a simpler factorized form

$$\langle j_1, j_2|\psi\rangle = e^{-\sigma^2\left(\frac{j_1+j_2}{2}-X\right)^2} e^{ik/2(j_1+j_2)}\phi(j_1-j_2)\,. \tag{C.14}$$

This factorized wavefunction naturally arises when considering the semiclassical limit in the next section and, if the wavepacket is sufficiently smooth, it is very close to Eq. (C.13). In Fig. 6.3 we choose the free parameters trying to not alter the global envelope of the wavepacket, hence we kept σ, X, k fixed and vary the energy spreading by acting on ϕ. In particular, we chose $k = 1.15$, $\sigma^2 = 0.08$ and $X = 10$, while the defect and confinement strengths are $d/h_x = 0.4$ and $\chi/h_x = 2h_z/h_x = 0.5$. The time scale is in units of h_x, which plays the role of a global energy scale. Then, the relative wavefunction is chosen as the exact wavefunction within a finite range $\phi(|j| \leq \Lambda) = \mathcal{J}_{j-\nu_{k,1}}\left(\frac{2h_x}{h_z}\cos(k/2)\right)$ and zero beyond $\phi(|j| > \Lambda) = 0$. The choices $\Lambda = \{3, 4, 12\}$ create the wavepackets with $\sigma_E = \{1.53, 1.06, 0.63\}$ respectively.

In Fig. 6.2.2 we present quantum simulations within the two domain-wall approximation of the metastable state lifetimes in the presence of impurities with varying mobility. We achieve this by using different values of τ. Here, we use the same initial wavepacket of Fig. 6.2, which we discuss in the next section. With reference to the parametrization of Eq. (C.14) and (C.19), we choose $d/h_x = 0.2$, $\chi/h_x = 0.25$, $k = -2$, $\sigma = 0.125$, $\ell = 1$, $\bar{x} = 3\ell$.

Numerical simulations are carried out by considering the two dimensional wavefunction on a fi-

nite segment $[-L/2, L/2]$ and the wavefunction is evolved through matrix-exponentiation of the two domain-walls subspace Hamiltonian (C.3). In order to remove finite size corrections by simulating a true infinite system, we add dissipation at the boundaries, thus removing the departing meson and preventing the wavepacket to return to the defect after it has been scattered away. This approach is thoroughly discussed in the framework of tensor network simulations in Sec. C.3.

C.2 The Semiclassical Limit

In this section we quantitatively match the semiclassical approximation against the quantum problem by means of a truncated Wigner approximation [147]. For the sake of simplicity, we focus on the two domain-wall subspace and consider a static impurity, but the method is readily generalized to the moving case. Let the initial state be described by a density matrix $\hat{\rho}$, then we use a coordinate representation $|j_1, j_2\rangle$ and define the Wigner quasi-distribution as

$$\langle j_1 + y_1/2, j_2 + y_2/2|\hat{\rho}|j_1 - y_1/2, j_2 - y_2/2\rangle = \int \mathrm{d}p_1 \mathrm{d}p_2 \, W(j_1, p_1, j_2, p_2) e^{iy_1 p_1 + iy_2 p_2}. \quad \text{(C.15)}$$

In principle, one needs to enforce $j_1 + y_1/2$ and all the other coordinates to be integers, but this will not be important. Indeed, classical physics emerges in the case where the wavefunction is smooth and the confinement is weak, thus coarse graining the discrete nature of the underlying lattice. We focus on the bulk of the dynamics, leaving the impurity aside for the moment, and consider the Schrodinger equation of motion $i\partial_t \hat{\rho} = [\hat{H}, \hat{\rho}]$ with $\hat{H}$ given in Eq. (C.1). By applying the equations of motion to the left hand side of Eq. (C.15) and expressing them in terms of the Wigner distribution, after some long but straightforward algebra one finds

$$\partial_t W(j_1, p_1, j_2, p_2) + 2h_z \left(\sin(p_1) + \sin(p_2)\right) W(j_1, p_1, j_2, p_2) \\ - V'(j_1 - j_2)(\partial_{p_1} - \partial_{p_2}) W(j_1, p_1, j_2, p_2) \simeq 0 \quad \text{(C.16)}$$

with $V'(x) = \partial_x V(x)$ and $V(x) = \chi|x|$. In the derivation, one assumes W to have a slow dependence on j_1, j_2 (smooth wavepacket) and asks $V(x)$ to be a smooth potential. In the case of confinement,

$V(x) = \chi|x|$ is not smooth in the origin, but this correction vanishes in the limit of small χ. In Eq. (C.16) one recognizes the classical Liouville equation for the phase space distribution $W(j_1, p_1, j_2, p_2)$ evolving with the classical Hamiltonian $\mathcal{H}_{\rm cl}$ reported in the main text (in the weak transverse field regime, $\epsilon(k) = -2h_z \cos(k)$ and $v(k) = \partial_k \epsilon(k) = 2h_z \sin k$). It is useful to consider the classical equation of motion

$$\begin{cases} \partial_t p_1 = -\chi \text{sgn}(j_1 - j_2) \\ \partial_t j_1 = v(p_1) \end{cases} \qquad \begin{cases} \partial_t p_2 = -\chi \text{sgn}(j_2 - j_1) \\ \partial_t j_2 = v(p_2) \end{cases} , \tag{C.17}$$

and notice the following scale invariance

$$t \to Xt \qquad x_{1,2} \to X x_{1,2} \qquad \chi \to \chi/X \tag{C.18}$$

where X is some positive scale. Notice that this invariance holds in the classical limit, but it is broken in the quantum regime. Nevertheless, we can use it as a convenient way to attain the classical limit, by means of rescaling to larger spaces and times.

The Wigner distribution of the wavepacket

When comparing quantum simulations with semiclassics, it is important to correctly capture the initial conditions. Here, we provide the initial Wigner distribution for simple wavepackets that we use in the simulations. We consider pure states $\hat{\rho} = |\psi\rangle\langle\psi|$ in the factorized form already anticipated in Eq. (C.14), but the wavefunction in the relative coordinates $\phi(x)$ is now chosen to be smooth. For example, a convenient choice is

$$\phi(x) \propto \begin{cases} e^{-\frac{1}{4\ell^2}(|x|-\bar{x})^2} & x < 0 \\ 0 & x \geq 0 \end{cases} . \tag{C.19}$$

Above, we ensured that the wavefunction vanishes when $j_1 < j_2$. By tuning the free parameters $\sigma, k, X, \ell, \bar{x}$ one can engineer a wavepacket of well defined momentum and control its energy. Notice that the wavefunction is factorized in terms of the center of mass and relative coordinates, therefore

the Wigner distribution has a factorized form as well

$$W(j_1, p_1, j_2, p_2) = \mathcal{W}\left(\frac{j_1 + j_2}{2}, p_1 + p_2\right) w\left(j_1 - j_2, \frac{p_1 - p_2}{2}\right) . \tag{C.20}$$

With this specific choice of wavefunction, one finds

$$\mathcal{W}(x, p) = \frac{1}{\sqrt{2\pi\sigma^2}} \exp\left(-\frac{1}{2\sigma^2}(p - k)^2 - 2\sigma\,(x - X)^2\right) . \tag{C.21}$$

The truncation of the Gaussian defining $\phi(x)$ in Eq. (C.19) prevents a simple analytical solution. However, in the limit where $e^{-\bar{x}^2/(2\ell^2)} \ll 1$ the tails can be neglected and one simply finds

$$w(x, p) \propto \exp\left(-\frac{|x| - \bar{x})^2}{2\ell^2} - 2\ell^2 p^2\right) . \tag{C.22}$$

The proportionality constant is not important and it can be fixed by ensuring the correct normalization of the state.

Details on Fig. 6.2

In Fig. 6.2 we compared simulations within the two domain-wall approximation against the truncated Wigner approach. We consider different choices of wavepackets governed by a global length scale in such a way the limit of infinitely smooth wavepacket collapses on a well defined classical limit. With reference to the wavefunction (C.14) and (C.19), we chose the initial position of the wavepacket X as our scaling parameter and set $d/h_x = 0.2$, $\chi = 5/X$, $k = -2$, $\sigma = 2.5/X$, $\ell = 0.05X$, $\bar{x} = 3\ell$. As we commented in Eq. (C.18), the classical equations are invariant under simultaneous rescaling of positions, time and confining strength. In the truncated Wigner, the exact invariance of the classical simulation is broken by the $X-$dependence of the momentum distribution, but it is restored in the $X \to +\infty$ limit.

The lifetime of the metastable state

We now wish to provide further details about the analytical determination of the metastable state formation after a scattering event. For the sake of simplicity, we focus on the static impurity $\tau = 0$, but the same analysis can be ready generalized to the moving impurity as well. We divide the problem in two steps

1. Compute the lifetime of an already trapped meson.

2. Compute the probability of get trapped in the scattering event.

Furthermore, we are interested only in the longest lived metastable states. Within this assumption, one can greatly simplify the analysis. If one considers an already trapped meson, it will remain trapped for long times only if the transmission probability of both fermions is very small. Within this assumption, we can compute the two points above within these approximations

1. Escape after first transmission: a trapped meson leaves the defect as soon as one of the two fermions is transmitted and it cannot be captured back.

2. Capture after a single transmission: since transmission is unlikely, we assume the meson is captured after a single transmission event of the fermion.

We have already discussed this simple calculation in the main text, here we quickly recap it and add some details. It is convenient to parametrized the classical trapped meson in terms of the momenta of the fermions when they hit the barrier. Following the same notation of the main text, we call them (k, q). Before transmission, each fermion evolves independently from the other, feeling a constant force pulling it towards the reflective barrier. Hence, in between two scatterings, the left fermion obeys the equation of motion $\dot{k} = \chi\,, \dot{x} = v(k)$ (we refer to the figure below for notation)

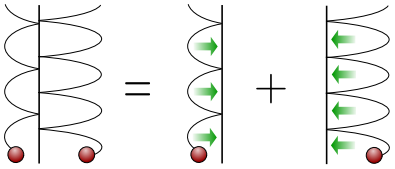

The period of the oscillation is readily computed noticing that, right after the reflection, the momentum of the fermion changes sign $k \to -k$ and the oscillation period $t_{osc}(k)$ is the time needed for the force to bring the momentum back to k, i.e. $k = -k + \chi t_{osc}(k)$. We now consider the probability that the leftmost fermion is not transmitted after n scatterings or, equivalently, the probability of being reflected $R(k)^n = (1-T(k))^n \simeq \exp[-nT(k)] \simeq \exp[-T(k)t/t_{osc}(k)]$. Using the oscillation period and asking that both fermions are not transmitted until time t, one gets Eq. (6.3) for the time evolution of the trapped probability, i.e.

$$P_t(k,q) = \exp\left[-t\frac{\chi}{2}\left(|k|^{-1}T(k) + |q|^{-1}T(q)\right)\right] P_{t=0}(k,q)\,. \tag{C.23}$$

The initial probability $P_{t=0}(k,q)$ depends on the details of the scattering, but surprisingly it can be computed in terms of geometrical considerations without solving the equation of motion.

We now consider the probability of forming a metastable state by shooting a mesonic wavepacket at the defect. For the sake of simplicity, we assume the meson has a well defined energy E and total momentum K. Furthermore, we approximate the capture time to be negligible (i.e. all the mesons of the wavepacket are captured within a time window much smaller than the decay time) and set $t = 0$ as the scattering time. Also within the assumption that the meson is captured only after a single transmission event, there are several possible processes where some reflections take place before the desired transmission shown below.

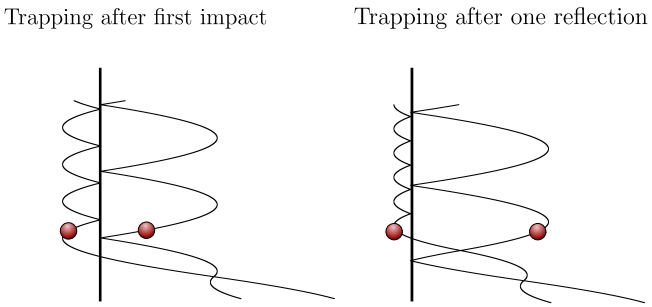

Each of these processes leads a different pair $\{(k_\ell, q_\ell)\}_{\ell=1,2,\ldots}$ of momenta for the trapped meson. The momenta k_ℓ and q_ℓ are not independent, but they must satisfy the constraint $E = \epsilon(k_\ell) + \epsilon(q_\ell)$: we prove it in the case of $\ell = 1$ with the aid of the picture below, the argument is easily extended to the case of generic ℓ. Let us focus on the first transmission event: in our notation, the impact of the first

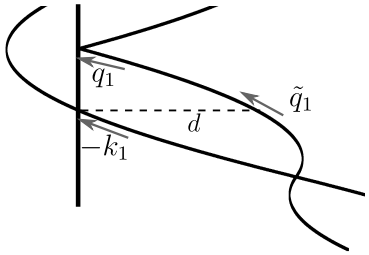

transmitted fermion happens at momentum $-k_1$. Meanwhile, the companion fermion is placed at a distance d and with momentum $\tilde{q}_1$. The total energy of the meson is thus $E = \epsilon(-k_1)+\epsilon(\tilde{q}_1)+\chi d$, for simplicity we can use the energy parity $\epsilon(-k_1) = \epsilon(k_1)$. After the first fermion gets transmitted, the other will move independently with momentum $q(t)$ and distance from the defect $d(t)$ and obeying the equation of motion $\dot{q} = -\chi\, \dot{d} = v(q(t))$. Of course, $E' = \epsilon(q(t)) + \chi d(t)$ is a conserved quantity. By comparison, with the energy of the meson, we have $E' = E - \epsilon(\tilde{q}_1)$. On the other hand, $q^{(1)}$ is the momentum at the moment of impact and can be found by asking $d(t) = 0$, hence $E = \epsilon(q_1) + \epsilon(k_1)$. The same argument can be generalized to arbitrary ℓ by noticing that the scattering with the defect conserves the total energy of the meson.

Energy conservation allows one to find q_ℓ if k_ℓ is known. As a next step, we build a recursive set of equations that fixes k_ℓ from the knowledge of the moment at first impact k_1, together with the total energy and momentum of the fermion. With the help of the figure below, let us consider $-k_1$ the momentum at first impact and, as before, let $\tilde{q}_1$ be the momentum of the companion. Right before the impact, the total momentum $K = -k_1 + q_1$ then the scattering fermion gets reflected and the total momentum becomes $K \to K' = k_1 + \tilde{q}_1$. Our next task is finding the momenta $\bar{k}, \bar{q}$ at the moment of the scattering among the two fermions. This is easily found by imposing that the total energy of the meson is purely kinetic and using the conservation of $K' = \bar{k} + \bar{q}$

$$E = \epsilon(\bar{k}) + \epsilon(k_1 + \tilde{q}_1 - \bar{k}). \tag{C.24}$$

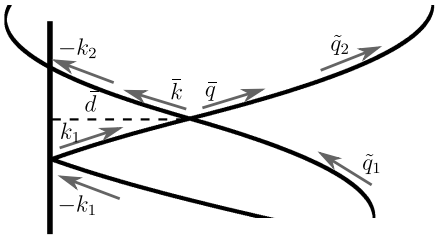

Lastly, from $\bar{k}$ and energy conservation one finds $-k_2$. Let be $\bar{d}$ the distance between the defect and the position of the scattering among the two fermions. With the current convention on the momenta, one has $\epsilon(\bar{q}) = \epsilon(k_1) + \chi d$, but also $\epsilon(\bar{k}) = \epsilon(k_2) + \chi d$, whose comparison gives the simple equation $\epsilon(\bar{k}) + \epsilon(\bar{q}) = \epsilon(k_1) + \epsilon(k_2)$. In summary, and moving to the general case k_ℓ, the recursive relation $k_\ell \to k_{\ell+1}$ is found as the solution of

$$\begin{cases} E = \epsilon(\bar{k}_\ell) + \epsilon(k_\ell + \tilde{q}_\ell - \bar{k}_\ell), \\ \epsilon(\bar{k}_\ell) + \epsilon(k_\ell + \tilde{q}_\ell - \bar{k}) = \epsilon(k_\ell) + \epsilon(k_{\ell+1}), \\ -k_{\ell+1} + \tilde{q}_{\ell+1} = k_\ell + \tilde{q}_\ell. \end{cases} \tag{C.25}$$

Since from momentum conservation one has $\tilde{q}_1 = K - k_1$, the full sequence (k_ℓ, q_ℓ) is entirely determined by k_1.

Let $p(k_1)$ being the probability that the meson hits the impurity with a fermion of momentum $-k_1$. Hence, it will create a trapped meson (k_1, q_1) with probability $p(k_1)T(-k_1)$. The pair (k_2, q_2) is instead created if the first scattering is reflective and then transmissive, hence it will be excited with probability $p(k_1)(1 - T(-k_1))T(-k_2)$ and so on so forth. Eventually, the probability $P_t(E, K)$ that a meson with energy E and momentum K gives a metastable boundstate at time t is

$$P_t(E,K) = \int \mathrm{d}k\, p(k_1) \sum_{\ell=0}^{\infty} T(-k_\ell) \left\{ \prod_{i=1}^{\ell-1} [1 - T(-k_i)] \exp\left[-\frac{\chi t}{2} \left(|k_\ell|^{-1} T(k_\ell) + |q_\ell|^{-1} T(q_\ell) \right) \right] \right\}_{E=\epsilon(k_\ell)+\epsilon(q_\ell)} . \tag{C.26}$$

The last ingredient is determining $p(k_1)$ that in general depends on the fine details of the initial state and the whole time evolution. However, there is at least one case where $p(k_1)$ can be easily obtain, i.e. in the approximation that the size of the wavepacket is much larger than the typical size of the meson. If it is the case, the impact of the fermion will randomly happen at a given position in its trajectory. In the figure below (left), the position of the defect can be arbitrarily moved within a maximum interval of length D. Notice that D is nothing else than the distance traveled by the meson within his breathing period, which we can compute with the help of the right figure.

Let p and $K - p$ the momenta of the two fermions when they scatter. Hence, by conservation of energy p is fixed solving $E = \epsilon(p) + \epsilon(K - p)$. Let us follow the trajectory of the fermion with

initial momentum p: after an oscillation period and right before scattering with the companion, its momentum will be $K - p$. Let us now focus on the displacement: from the equation of motion, we have $D = \left|\int_0^\tau \mathrm{d}t v(p(t))\right|$ with τ the oscillation period and $p(t)$ the time-evolving momentum. By using $\dot{p} = \chi$ and $v(k) = \partial_k \epsilon(k)$, we can easily compute D as $D = \chi^{-1}|\epsilon(K-p) - \epsilon(p)|$. Finally, we can compute k_m from energy conservation $\epsilon(k_m) = \epsilon(0) + \chi D$. Putting the pieces together, k_m is defined by solving

$$\begin{cases} \epsilon(k_m) = \epsilon(0) + |\epsilon(K-p) - \epsilon(p)|, \\ E = \epsilon(p) + \epsilon(K-p). \end{cases} \tag{C.27}$$

Within the allowed window of momenta, we are considering a flat average over the position of the meson at the moment of impact. When changing coordinates to the momentum space, one needs to consider the proper Jacobian: this is easily done from the equation of motion $|\dot{k}| = \chi$ and $|\dot{x}| = |v(k)|$, hence $\mathrm{d}k_1 = \mathrm{d}x|v(-k_1)|\chi^{-1}$. Thus, one finds

$$p(-k_1) \propto |v(-k_1)|\theta(|k_m| - |k|)\theta(k_1 \mathrm{sign}(v(k_1)))\,, \tag{C.28}$$

where θ is the Heaviside theta function and the proportionality constant is fixed by imposing that $p(-k_1)$ is normalized to unity.

C.3 The Tensor Network Simulations

In this section we discuss the tensor network simulations and details for Fig. 6.5. However, first we discuss how the initial mesonic wavepacket can be prepared and controlled.

The wavepacket initialization: the meson creation operator

Here we discuss how to create two fermions in the transverse Ising chain via spin operators. It will be later employed for the creation of a moving meson as the initial state in the tensor network numerical simulation. We start by considering the transverse field Ising model

$$H = -\sum_j \frac{1}{2}\left[\sigma_j^z \sigma_{j+1}^z + h_x \sigma_j^x\right], \tag{C.29}$$

The system can be mapped into the free fermion representation with a Jordan Wigner transformation

$$d_j = \sum_{i=-\infty}^{j-1} \sigma_i^x \sigma_j^- \tag{C.30}$$

with $\sigma_j^{\pm} = (\sigma_j^z \pm i\sigma_j^y)/2$. Then one defines the modes in the Fourier space as

$$\begin{pmatrix} d_j \\ d_j^\dagger \end{pmatrix} = \int_{-\pi}^{\pi} \frac{\mathrm{d}k}{2\pi} e^{ikj} \begin{pmatrix} \cos\theta_k & i\sin\theta_k \\ i\sin\theta_k & \cos\theta_k \end{pmatrix} \begin{pmatrix} \gamma(k) \\ \gamma^\dagger(-k) \end{pmatrix}, \tag{C.31}$$

where $\theta_k = \frac{1}{2i}\log\left[(h_x - e^{ik})/(1 + h_x^2 - 2h_x\cos(k))\right]$. With this choice, the Ising Hamiltonian is diagonal in the mode operators $\gamma(k)$ and the ground state is identified with the vacuum $\gamma(k)|0\rangle = 0$. As a next step, we would like to create a pair of fermions on top of the vacuum. To this end, let us consider an operator defined in the following form

$$O_j = \sum_{\ell\geq 0} \sigma_j^+ \prod_{i=j}^{j+\ell-1} \sigma_i^x \sigma_{j+\ell}^+ F(\ell) = \sum_{\ell\geq 0} d_j^\dagger d_{j+\ell}^\dagger F(\ell), \tag{C.32}$$

with a fast decaying, e.g. exponential, space-dependent function $F(\ell)$. From the O_j operator, we create $O(P, j_0)$ as

$$O(P, j_0) = \sum_j e^{-(j-j_0)^2/\sigma^2} e^{iPj}(O_j + \mathcal{A}). \tag{C.33}$$

The idea is that $O(P, j_0)$ tries to create a wavepacket in motion, centered around j_0 and with momentum P. $\mathcal{A}$ is a constant inserted for imposing the normal ordering with respect to the γ operators and is determined below.

When we express O_j in terms of modes, it will contain operators in the form $\gamma^\dagger\gamma^\dagger$ (which create two fermions), but also $\gamma^\dagger\gamma$, $\gamma\gamma^\dagger$ and $\gamma\gamma$. We are interested in the action of $O(P, j_0)$ on the vacuum and if we fix the constant $\mathcal{A}$ as

$$\mathcal{A} = -\left(\sum_{\ell>0} F(\ell) \int \frac{\mathrm{d}q}{2\pi} e^{-iq\ell} \left(i \sin\theta_q \cos\theta_q\right) \right), \tag{C.34}$$

we obtain a two-fermions state

$$O(P, j_0)|0\rangle = \sum_j e^{-(j-j_0)^2/\sigma^2} e^{iPj} \left(\sum_{\ell\geq 0} F(\ell) \int \frac{\mathrm{d}k}{2\pi} \int \frac{\mathrm{d}q}{2\pi} e^{-ikj} e^{-iq(j+\ell)} \cos\theta_k \cos\theta_q \gamma^\dagger(k)\gamma^\dagger(q) \right)|0\rangle. \tag{C.35}$$

We now first sum over j and define

$$W(P-k-q) = \sum_j e^{-(j-j_0)^2/\sigma^2} e^{i(P-k-q)j}, \tag{C.36}$$

which becomes very peaked in the momentum space $\lim_{\sigma\to\infty} W(P-k-q) = 2\pi\delta(P-k-q)$ for large σ. We further define

$$\tilde{F}(q) = \sum_{\ell\geq 0} F(\ell) e^{-iq\ell}, \tag{C.37}$$

leading to the following compact expression

$$O(P, j_0)|0\rangle = \left(\int \frac{\mathrm{d}k}{2\pi} \int \frac{\mathrm{d}q}{2\pi} W(P-k-q) \tilde{F}(q) \cos\theta_k \cos\theta_q \gamma^\dagger(k)\gamma^\dagger(q) \right)|0\rangle. \tag{C.38}$$

Lastly, we use the asymmetry of the fermions to rewrite the last expression as

$$O(P, j_0)|0\rangle = \left(\int \frac{\mathrm{d}k}{2\pi} \int \frac{\mathrm{d}q}{2\pi} W(P-k-q) \frac{\tilde{F}(q) - \tilde{F}(k)}{2} \cos\theta_k \cos\theta_q \gamma^\dagger(k)\gamma^\dagger(q) \right)|0\rangle. \tag{C.39}$$

Clearly, $\left| W(P-k-q) \frac{\tilde{F}(q)-\tilde{F}(k)}{2} \cos\theta_k \cos\theta_q \right|^2$ is the semiclassical probability of the wavepacket. Tuning σ and the function F we can change the wavepacket. So far we kept F arbitrary but we require F to be fast decaying in ℓ for both computational reasons and to get a more localized wavepacket. F must be tuned if one wants to act on the probability distribution of the difference in the momentum

of the two fermions (while W acts on the total momentum). A convenient choice is choosing F as a Kronecker delta

$$F(\ell) = \delta_{\ell,\ell_0} \tag{C.40}$$

for a certain ℓ_0. Note, the state $|\Psi\rangle = O(P, j_0)|0\rangle$ is not normalized. It must be renormalized before running the simulation. After this, the state $|\Psi\rangle$ will exactly contain two fermions, i.e. one meson.

Numerical details on the Tensor network calculation

The tensor network simulation of the dynamics is implemented via the Python library TeNPy as detailed in Ref. [152]. The strong confinement in our mode significantly suppresses the spreading of correlations throughout the whole system, hence, permitting an efficient tensor network simulation with a low bond dimension for a long time.

We first use the Density Matrix Renormalization Group (DMRG) algorithm to prepare the system of length $L = 240$ with open boundary in its groundstate of the Hamiltonian

$$H_{\text{Ising}} = -\sum_i \sigma_i^z \sigma_{i+1}^z - h_x \sum_i \sigma_i^x - (d - h_x)\sigma_0^x - h_z \sum_i \sigma_i^z, \tag{C.41}$$

where the defect located on site 0. The transverse field is chosen as $h_x = 0.3$, and a non-zero but small longitudinal field $h_z = 0.01$ is used to break the two-fold groundstate degeneracy. As the groundstate is approximately a simple ferromagnetic state without long-range correlation, a low bond dimension $\chi = 20$ is sufficient.

Now we want to create the initial meson wavepacket with a non-zero velocity such that it can move towards the impurity. As introduced in the last section, we construct a string operator $O\left(P, j_0\right)$ according to Eq. (C.33),

$$O\left(P, j_0\right) = \sum_j e^{-(j-j_0)^2/\sigma^2} e^{iPj} \left(O_j + \mathcal{A}\right), \tag{C.42}$$

with

$$O_j = \sum_{\ell \geq 0} \sigma_j^+ \prod_{i=j}^{j+\ell-1} \sigma_i^x \sigma_{j+\ell}^+ F(\ell), \quad \mathcal{A} = -\left(\sum_{\ell>0} F(\ell) \int \frac{\mathrm{d}q}{2\pi} e^{-iq\ell} \left(i \sin\theta_q \cos\theta_q \right) \right), \tag{C.43}$$

and $F(\ell) = \delta_{l,1}$. Numerically we choose $j_0 = 10$, $P = \pi/2$, $\sigma = \sqrt{4L/\pi}$ and the summation over j to be limited within $[j_0 - 10, j_0 + 10]$. Acting the operator $O\,(P, j_0)$ on the groundstate creates a wavepacket with a total momentum P. However, the created meson is a superposition of excitations of different energies, and therefore, each of them has a different velocity.

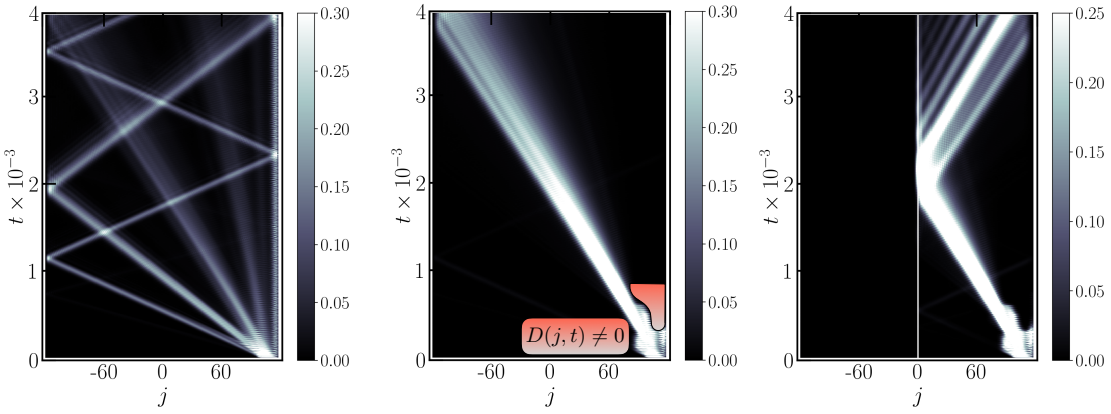

Figure C.3: Dynamics of the connected correlation $\langle \sigma_i^z \sigma_{i+1}^z \rangle$ calculated via TEBD algorithm. Left: no dissipation and no impurity. Middle: No impurity $d = h_x$. Dissipation is included such that only one wavepacket survives. Right: Both dissipation and impurity d=0.1 are present and the metastable state is clearly visible. For all three plots, we use $h_x = 0.3, h_z = 0.12, L = 240$.

The time evolution of the dynamics is achieved by the Time Evolving Block Decimation (TEBD) algorithm with a low bond dimension $\chi = 20$. We use a time step $dt = 1$ and the fourth order Suzuki-Trotter decomposition for the time evolution. The connected part of the correlation $\langle \sigma_i^z \sigma_{i+1}^z \rangle$ is employed to trace the position of the meson. As shown in the left panel of Fig. C.3, the wavepacket quickly spreads with distinct velocities, corresponding to different excitations of the system.

In the absence of the impurity, the wavepackets with the faster velocities bounce at the boundary and reflect back, interfering with the slowly moving wavepackets at later times. Although not shown here, such interference happens more severely when the impurity is present. Consequently, the trapped meson is not clearly visible and its lifetime is difficult to analyze. To address this, we further additionally

introduce the non-Hermitian Hamiltonian to induce week dissipation of the form

$$H_{\text{dis}}(t) = i \sum_j D(j,t) \left(\sigma_j^z \sigma_{j+1}^z + h_x \sigma_j^x \right), \tag{C.44}$$

where $D(j,t)$ is a time-dependent function with a positive amplitude (the maximum value is around 0.01) that smoothly decays in space. For a fixed time $t_0 < 750$, $D(j,t_0)$ is non-zero in regions where undesired meson components move through and get dissipated, permitting us to select the meson wavepacket with an approximately constant velocity. As shown in the middle panel of Fig. C.3, we choose a profile $D(j,t)$ nonzero in the red regions such that only one wavepacket survives and the amplitude of the correlation function also gets amplified due to the normalization of the wavefunction. At later times, we also use a non-zero $D(j,t)$ at the boundary to reduce the finite size effect. In the end, in the right panel, we introduce the impurity $d = 0.1$ same as Fig. 6.5 at the middle of the system and plot the dynamics where a long-lived metastable state can be clearly identified.

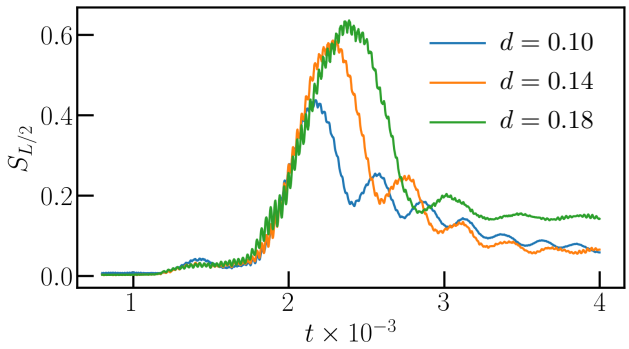

Figure C.4: Dynamics of the half-system entanglement entropy.

We further provide the dynamics of the half-system entanglement entropy defined as

$$S_{L/2}(A) = -\operatorname{tr} \hat{\rho}_{L/2} \log \hat{\rho}_{L/2}, \tag{C.45}$$

where $\hat{\rho}_{L/2}$ denotes the reduced density matrix of half of the system. As the impurity locates at the center of the chain, before the meson-impurity scattering happens, there is almost no entanglement established between two halves of the system. Entanglement entropy suddenly increases around $t \sim 2\times10^3$ where one domain-wall tunnels through the impurity and becomes entangled with the other domain-wall reflected back. It drops down when the transmitted and reflected particles eventually

leave the impurity. Overall, the entanglement of the whole system remains at low values permitting the efficient long-time simulation of the dynamics with a low bond dimension.

Details on Fig. 6.5

Here we give a brief summary of parameters used for Fig. 6.5. For the initial state generation, we use $F(l) = \delta_{l,1}, j_0 = 10, P = \pi/2$ and $\sigma = \sqrt{4L/\pi}$ to determine string operator in Eq. C.43. For the time evolution, we use bond dimension $\chi = 20$, $dt = 1$ and the fourth order Suzuki-Trotter decomposition. The Hamiltonian parameters are $h_x = 0.3, h_z = 0.12$ and $L = 240$. The defect size is $d = 0.1$ in the left panel.

Appendix D

This section is lifted from the supplementary material of Ref. [4].

D.1 Meson Wavepackets

The initial state used in the collision of mesons in Fig. 7.5 is given by

$$|\psi_{t=0}\rangle \propto \sum_{n_1,j_2,n_2} \int dk\, e^{-\frac{(n_1-N_1)^2}{2\sigma_1^2}} e^{ik(j_2+\frac{n_2}{2})} e^{-\frac{(k-q)^2}{2\sigma_k^2}} e^{-\frac{(j_2+n_2/2-c)^2}{2\sigma_c^2}} e^{-\frac{(n_2-N_2)^2}{2\sigma_2^2}} |n_1, j_2, n_2\rangle\,, \tag{D.1}$$

where q is the average momentum of the mobile meson with a standard deviation σ_k, c is the average centre of mass of the mobile meson with standard deviation σ_c and N_i is the average width of the i^{th} meson with standard deviation σ_i. In particular I use the parameters $q = -1$, $\sigma_k = 0.1$, $\sigma_c = 2$, $N_1 = 10$, $N_2 = 4$, $\sigma_i = 1$ for $i \in 1, 2$ and $c = 60$.

The initial states used in the collision of mesons in Fig. 7.6 and Fig. 7.8 are given by

$$|\psi_{t=0}\rangle \propto \sum_{j_1,j_2} e^{-ikj_1-\frac{(j_1+n-2c_1)^2}{4\sigma^2}} e^{ikj_2-\frac{(j_2+n-2c_2)}{4\sigma^2}} |j_1, n, j_2, n\rangle\,, \tag{D.2}$$

where k is the initial momentum of each meson, c_i is the centre of the wavepacket of the i^{th} meson and σ is the standard deviation of the wavepacket in real space. In particular the parameters used in Fig. 7.6 are $k = -1.5$, $c_1 = 15$, $c_2 = 35$ and $\sigma = 0.1$. The parameters used in Fig. 7.8 are $k = -1$, $c_1 = 10$, $c_2 = 30$ and $\sigma = 3$.

Finally, the tetraquark wavepacket used in the simulations presented in Fig. 7.9 is given by

$$|\psi_{t=0}\rangle \propto \sum_j e^{-ikj-\frac{(j_1-c)^2}{2\sigma^2}} |j,d\rangle \,. \tag{D.3}$$

where k is the tetraquark momentum (which I set to zero), c is the average position of the first meson and σ is the standard deviation of the wavepacket. In particular the parameters used are $d = 4$, $k = 0$, $c = 18$ and $\sigma = 5$.

D.2 Truncation of Meson Width

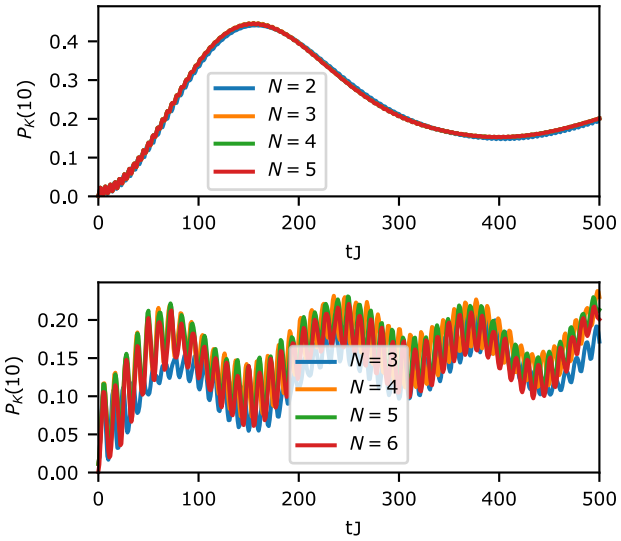

Figure D.1: A comparison of meson dynamics for different truncations in meson width, $n_1, n_2 \leq N$, for the four domain-wall subspace. Here, $L = 20$, $h = 0.1$ and $\alpha = 2.5$. The upper panel considers an initial state of two spatially separate 1-mesons, $|4, 1, 12, 1\rangle$ and the lower panel considers an initial state of two spatially separate 2-mesons, $|4, 2, 12, 2\rangle$. From this we see that as N increases the dynamics are converge to the what is the dynamics of the full four domain-wall subspace.

In order to simulate large system sizes I turned to the four domain-wall subspace described by the Hamiltonian given by Eq. 7.1. The size of this subspace grows as L^4, here L is system size. This still poses a problem when considering the system sizes required to observe collision events. In order to reduce the computational cost of simulations to quadratic growth, I used a truncation in the meson width, $n_1, n_2 \leq N$ for some constant N. When considering small mesons, varying the width of a meson vastly changes the energy of the state. Thus, in order to conserve energy, the meson width will

only experience small fluctuations. As a result, accurate approximations of the full four domain-wall subspace are achieved by only considering n_1 and n_2 values below some constant that is at least larger than the meson widths of the initial state. Fig. D.1 compares time dynamics of mesons for initial states of meson width 1 and 2 simulated in the four domain-wall subspace with varying truncations. We clearly see that both $1-$mesons and $2-$mesons are accurately simulated with a truncation of $N \sim 5$. This approximation will naturally become less accurate as the initial state contains larger mesons.